NORTHWESTERN UNIVERSITY

Ultrafast Photophysical Dynamics of Structural and Electronic Behavior in Hybrid and Nanostructured Semiconductors

A DISSERTATION

SUBMITTED TO THE GRADUATE SCHOOL

IN PARTIAL FULFILLMENT OF THE REQUIREMENTS

for the degree

DOCTOR OF PHILOSOPHY

Field of Chemistry

By

Shobhana Panuganti

EVANSTON, ILLINOIS

September 2023

Abstract

Ultrafast Photophysical Dynamics of Structural and Electronic Behavior in Hybrid and Nanostructured Semiconductors

Shobhana Panuganti

Renewable energy technology, more so than ever before, is critical to the survival of humanity. For decades, concentrated efforts into designing and developing such novel devices resulted in the innovation of solar-driven photovoltaics that were competitive with nonrenewable alternatives. This thesis explores the dynamic behavior of alternative material candidates that exhibit exceptional light-absorbing properties due to their unique hybrid and nanostructured compositions. Many previous studies of the materials discussed herein have focused on gradual improvements to specific aspects of device architectures, though much remains elusive regarding their fundamental electronic responses that would accelerate material design by guiding synthesis for certain properties.

The influence of the distance on rates of energy transfer between donor and acceptor states within an extended nanostructured solid, such as two-dimensional perovskite quantum wells, was investigated *via* transient absorption and time-resolved emission studies. Importantly, specific distances were targeted with high precision throughout the bulk material through synthetic, compositional modifications. Empirically measured, correlated kinetics of electronic behavior and subsequently calculated rates of energy transfer between states aligned well with computational

models of such systems, pointing to the reliability of this test system for explorations of other fundamental photophysical phenomena.

In colloidal studies of the lifetimes of spin-coherence in biexcitons generated by cross-polarized incident laser pulses, several variables were carefully manipulated with respect to the structure and morphology of the nanoparticles. Results indicated that lifetimes of coherence increased slightly with increasing nanoplatelet thickness but were significantly prolonged by the presence of core-shell morphology regardless of heterojunction identities and band alignment, pointing to surface passivation as a principal factor in dictating spin-coherence lifetimes.

Transient X-ray diffraction of bulk hybrid perovskites, including thin films of methylammonium lead iodide, revealed non-equilibrium phase transitions that had not been previously observed or accessed under experimental conditions. These findings demonstrated the dissonance between the steady-state and *in situ* properties of materials, especially under operating conditions for devices, further highlighting the need for ultrafast structural characterization. In particular, the extent of thermal and electronic effects following photoexcitation was clarified, with electronic reorganization playing a dominant role in the observed structural dynamics.

Acknowledgments

When I started graduate school five years ago, I could hardly have imagined the journey I was about to undertake. I might read the *Iliad* or the *Ramayana* one day just to delve into an adventure of equal scale again. I've endured more never-ending nights, half-operational computer systems, disgustingly overused industrial lubricant, and fish/egg/garbage odors than I'd hope to encounter in all my life – and yet, I savor every aforementioned, cranky detail; for they make up the best parts of the many stories and cherished moments I've been lucky enough to share with all of the amazing people who have surrounded me these past few years.

Thank you to my advisors, Profs. Rich Schaller and Mercouri Kanatzidis, for your unwavering confidence in my potential, and your encouragement to perform the types of research and experiments I had previously thought were only realizable in science fiction novels. Each new project involved another aspect of chemistry that seemed impossible, unbelievable, always renewing my faith in the awe-inspiring nature of scientific discovery. I also want to thank those who stepped in to serve on my committee for their suggestions and insights regarding my work, Profs. Danna Freedman, Ken Poeppelmeier, Mark Hersam, and Joe Hupp. And of course, so much of my learning, of the hand-holding that was required to understand even a fraction of my own research, came from Christos Malliakas and Burak Guzelturk.

Somewhere, somehow, I must have known how much I would need my family within arms-reach. Every day, I am grateful for the unconditional warmth and support of my mom, dad, and my little brother, who drove up to my apartment at a moment's notice with food, who definitely couldn't keep me sane but never complained (much) about my insanity either. Amma and Nana: you were the first natural scientists who inspired me – by being curious and exploring the world

in your own beautiful ways – so thank you for showing me exactly what kind of scientist I wanted to be. Siddu, thank you for being so much cooler than I was at your age, and reminding me that life is meant to be fun.

I am so lucky to have collected a ragtag, extended family of the silliest folks living around Lake Michigan. They came together across time, from pre-puberty years to high school to college. Aaron, Giuliana, Chris, Stephanie, Silas: I'm so glad that I'm looking up five years later and you're still all here, smiling at me, loving me.

To all my labmates, for holding me up whenever I couldn't, I'd fall in line behind any of you into battle – Alexandra, Sam, Ariel, Daniel, Becca, Craig, Mike, Shelby, Caitlin, Eric.

To Dr. Nicolas Watkins, whom I will always hear on the wind.

To my Saturday group, for showing me what love really means.

To Ben, for seeing the whole of me and never being afraid.

To Nadia, the wildest baddest witch godmother on Earth.

I am, because of all of you, nothing more or less.

List of Abbreviations

PCE	power conversion efficiency
HOMO	highest unoccupied molecular orbital
LUMO	lowest unoccupied molecular orbital
E_g	optical band gap
XRD	X-ray diffraction
UV-Vis	ultraviolet-visible
PXRD	powder X-ray diffraction
PL	photoluminescence
TA	transient absorption
TR-XRD	time-resolved X-ray diffraction
2D	two-dimensional
3D	three-dimensional
K	Kelvin
A	absorbance
S	scattering
I	intensity
a.u.	arbitrary units
OD	optical density
fs	femtosecond
ps	picosecond

ns	nanosecond
μs	microsecond
EJ	exajoule
μJ	microjoule
FRET	Förster resonance energy transfer
PQW	perovskite quantum well
MA	methylammonium
FA	formamidinium
BA	butylammonium
HA	hexylammonium
OA	octylammonium
ML	monolayer
QD	quantum dot
NPL	nanoplatelet

Dedication

For my amma Sadhana, for my ammamma Suryakantham, for my nanamma Sarojini, and for all the ammas who made me.

नमामि त्वां महादेवीं महाभयविनाशिनीम्।
महादुर्गप्रशमनीं महाकारुण्यरूपिणीम् ॥

I bow to Thee, Goddess, dispeller of gravest fears;
Destroyer of great difficulties, radiant love incarnate.

श्री देव्यथर्वशीर्षम्
Sri Devyatharvasirsha

Table of Contents

Abstract **3**

Acknowledgments **5**

List of Abbreviations **7**

Dedication **9**

Table of Contents **10**

List of Tables **12**

List of Figures **13**

Chapter 1. Introduction **15**

1.1 Energy Needs Demand Solar Technology 15

1.2 Unique Structures Enable Unique Electronic Properties 17

1.3 Photophysical Processes in Semiconductors 21

1.4 Monitoring Photophysical Phenomena using Ultrafast Spectroscopy 23

1.5 Scope of this Thesis 29

Chapter 2. Distance Dependence of Förster Resonance Energy Transfer Rates in 2D Perovskite Quantum Wells via Control of Organic Spacer Length **31**

2.1 Abstract 31

2.2 Introduction 32

2.3 Results and Discussion 35

2.4 Conclusion 46

Chapter 3. Excitonic Spin-Coherence Lifetimes in CdSe Nanoplatelets Increase Significantly with Core/Shell Morphology **47**

3.1 Abstract 47

3.2 Introduction 48

3.3 Results and Discussion 50

3.4 Conclusion 62

Chapter 4. Transient X-ray Diffraction Reveals Non-Equilibrium Phase Transition in Thin Films of CH_3PbI_3 Perovskite **64**

4.1 Abstract 64

4.2 Introduction 65

4.3 Results and Discussion 68

4.4 Conclusion 78
Chapter 5. Dynamic Anisotropy in Photoexcited Lead Bromide Perovskites 80
5.1 Abstract 80
5.2 Introduction 81
5.3 Experimental Methods 83
5.4 Results and Discussion 86
Chapter 6. Conclusions and Outlook 88
Appendix A: Supplementary Information for Chapter 2. 90
A.1 Experimental Methods 90
A.2 Static characterization 92
A.3 Transient spectroscopies 97
A.4 Distance determinations 100
A.5 Theoretical modelling 101
Appendix B: Supplementary Information for Chapter 3. 103
B.1 Experimental Methods 103
B.2 Supplementary Data 105
Appendix C: Supplementary Information for Chapter 4. 108
C.1 Experimental Methods 108
C.2 Data Processing 110
C.3 Temperature Estimations 111
C.4 Additional Data 112
References 114
Curriculum Vitae 129

List of Tables

Table A. 1. Distance data for BA, HA, and OA donor *n = 1* and acceptor *n = 2* neat phases and binary mixtures. Values calculated from crystal structure information obtained through single crystal X-ray diffraction. 100

Table B. 1. Lifetimes of spin depolarization in 2, 3, 4, 5, 6 monolayer CdSe nanoplatelets from single-exponential fitting of spin decay. 105
Table B. 2. Lifetimes of spin depolarization in 5CdSe/*X*CdS core/shell samples with *X*=1, 3, 6 monolayer CdS from biexponential fitting of spin decay. 105
Table B. 3. Lifetimes of spin depolarization in 5CdSe/*X*ZnS core/shell samples with *X*=1, 3 monolayer ZnS from biexponential fitting of spin decay for larger amplitude components. 105

Table C. 1. Minimum and maximum temperature estimations of the photoexcited volume *V* as a function of pump fluence. 111

List of Figures

Figure 1. 1. Density of energy states from single molecules to semiconductor band theory. 17
Figure 1. 2. Representative structures of hybrid perovskites and perovskite quantum wells. 19
Figure 1. 3. Photoexcitation and subsequent electronic processes. 21
Figure 1. 4. Experimental geometry of transient absorption spectroscopy. 24
Figure 1. 5. Steady-state UV-vis versus transient absorption 26
Figure 1. 6. Experimental geometry for time-resolved X-ray diffraction measurements. 28

Figure 2. 1. Static characterization of 2D PQWs. 36
Figure 2. 2. Dynamic optical measurements of BA $n = 1$ and $n = 2$ phase-pure and mixed composition films by transient absorption. 38
Figure 2. 3. Energy transfer in mixed films. 40
Figure 2. 4. Results of computational modeling for FRET in PQW systems. 42

Figure 3. 1. Absorption spectra of CdSe nanoplatelet dispersions in hexanes. 50
Figure 3. 2. Transient absorption spectral maps from copolarized, cross-polarized, and electro-optically modulated pump-probe conditions. 51
Figure 3. 3. Spin-dependent lifetimes and binding energies as a function of NPL thickness. 54
Figure 3. 4. Kinetics and fitted lifetimes in core/shell NPLs. 57
Figure 3. 5. Spin-decay characteristics in CdSe/Zns core/shell NPLs. 59

Figure 4. 1. Steady-state structures of $MAPbI_3$. 67
Figure 4. 2. Transient diffraction patterns for $MAPbI_3$. 69
Figure 4. 3. Rise and recovery transient patterns and kinetics 72
Figure 4. 4. Fluence-dependent behavior and volume expansion. 76

Figure 5. 1. Steady-state (above) and transient, excited-state (below) patterns. 86

Figure A. 1. Donor *n = 1* (blue) and acceptor *n = 2* (red) PXRD patterns for crystalline materials. 94
Figure A. 2. Mixed binary films of butylammonium, hexylammonium, and octylammonium A' site cation materials 94
Figure A. 3. Absorption and photoluminescence spectra of films. 95
Figure A. 4. Mixed binary films. 96
Figure A. 5. Time-resolved absorption spectral maps as a function of probe wavelength. 97

Figure A. 6. Time-resolved photoluminescence data of octylammonium neat and binary materials. Kinetic data are normalized at t = 0 ps which is the moment of incident excitation. .. 99
Figure A. 7. Calculated FRET lifetimes as a function of dipole strength. 101
Figure A. 8. Calculated lifetimes as a function of dipole orientation 102

Figure B. 1. Dynamics of complete spin decay for indicated core-only CdSe samples. 106
Figure B. 2. Spin depolarization for 5CdSe/*X*CdS samples 106
Figure B. 3. Spin depolarization for 5CdSe/*X*ZnS samples. 107

Figure C. 1. Absolute values of maximum change in signal intensity ($|\Delta I|$) over time. 112
Figure C. 2. Normalized integrated absolute values of the peak area ($\int|\Delta I|$) of the (211) reflection. 113

Chapter 1. Introduction

1.1 Energy Needs Demand Solar Technology

Across the world, rapidly industrializing nations are devouring energy. Combined with mounting global population numbers, projected future energy demands are alarming. While total global energy consumption in 2021 neared 595 EJ, global projections for 2040 exceed 733 EJ. Fossil fuels continue to meet more than 80% of that demand, despite incontrovertible evidence that emissions from fossil fuel combustion are a significant contributor to anthropogenic climate change. Recent climate models indicate that continuation of current global practices will lead to irreversible global warming of over 3°C by the end of the 21st century that would result in, and indeed is already a force for, catastrophic conditions for human systems. Even the most generous estimates for sustained human use of non-renewables outline pathways for reserves that would supply a few centuries at best, though having required eons to form within the Earth, and simply cannot keep up with long-term global needs. Immediate, widespread development and democratization of renewable energy technology is urgent and unavoidable for humanity's future goals to be realized.[1-5]

In the search for renewable resources, solar energy in the form of sunlight has long been considered one of the most attractive alternatives. Irradiating the surface of the Earth with over 430 EJ/hour,[3] the sun provides energy on a scale that could completely reshape global human systems if harnessed fully, let alone amply satisfy current global demand in well under two hours.[4] The irresistibility of harnessing sunlight to usefully supply energy instigated the first published report in 1873 of a photovoltaic device using selenium. Several properties for material candidates

were then identified as crucial for photovoltaic operation and still remain primary considerations for material design and optimization in creating efficient and competitive solar cells: 1) direct and broad absorption of light across the solar irradiance spectrum; 2) fabrication using easy, reproducible methods and widely available precursors; and 3) long-term environmental stability in a variety of conditions.[6, 7]

Since their rapid development in the 1970s using similar principles to selenium devices, silicon-based photovoltaics have dominated the commercial market. Other materials have been developed that have significant advantages over silicon, but silicon continues to outcompete for all the aforementioned considerations as a whole. While valuable increases in power conversion efficiency (PCE) approaching theoretical limits have been made since then,[8] silicon solar cells still necessitate defect-free materials with high purity, epitaxial growth conditions, and skilled manufacturing personnel to ensure functional devices.[7] This creates a nearly insurmountable barrier to access for most of the global population, who either do not live proximally to or cannot afford the technology.[1, 2] True democratization of renewable energy to meet rising global demand and climate crises depends on optimizing aforementioned material properties such that these technologies can be manufactured, utilized, and maintained on a household basis with basic experience and education. While these goals can seem idealistic and even unrealistic, one imagines them accomplished in the way that computers quickly transformed from niche room-sized equipment reserved for world experts into handheld smart devices that today's toddlers operate with greater ease than their parents.

New classes of materials, such as colloidal II-VI semiconductors and hybrid organic-inorganic perovskites, have been the focus of much research effort in recent decades. These

materials typically incorporate inexpensive precursors, consisting of earth-rich metals and simple organic compounds, with facile solution-processibility at room temperature, making them incredibly attractive candidates for a variety of applications. Straightforward access to these materials has led to the rapid discovery and development of a vast catalog of analogous materials, each with astonishingly unique properties.[9] In just fifteen years, investigations into solar cells fabricated from hybrid organic-inorganic perovskites have skyrocketed PCEs to over 26%, outperforming commercially available silicon devices.[10, 11]

1.2 Unique Structures Enable Unique Electronic Properties

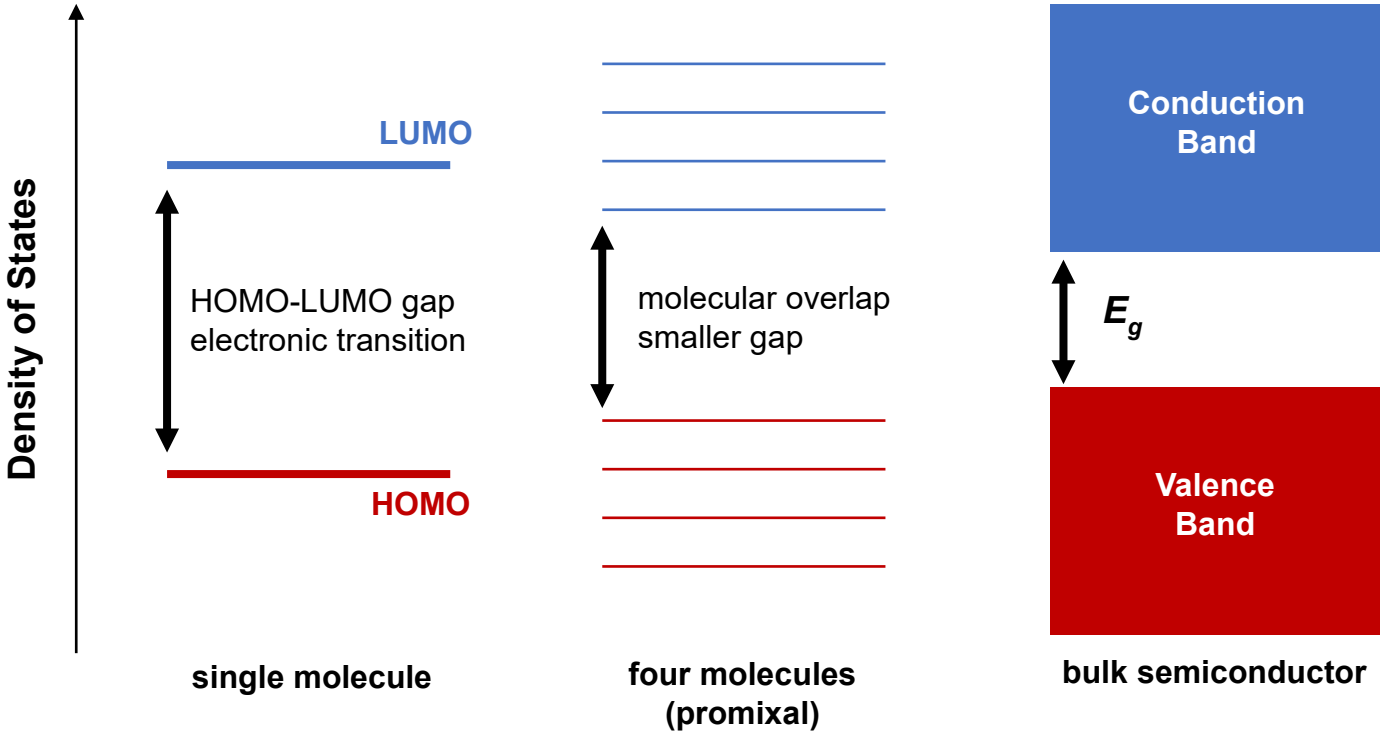

Figure 1. 1. Density of energy states from single molecules to semiconductor band theory. In a single molecules, an electron in the highest occupied molecular orbital (HOMO) is restricted from occupying the lowest unoccupied molecular orbital (LUMO) by the energy gap between the levels. As the electronic wavefunctions of the orbitals in multiple molecules began to overlap, the HOMO-LUMO gap becomes smaller, requiring less energy for an electronic transition. In bulk semiconductors, the HOMO-LUMO levels of individual molecules no longer appear distinguishable, forming instead valence and conduction bands separated by the optical band gap.

Much of the outstanding performance and versatility of nanomaterials and hybrid perovskites is attributed to their unique structures, which can differ greatly with respect to the electronic structure observed in typical bulk semiconductors. According to band theory, discrete energy levels on the molecular level begin experiencing effects of long-range coherence that lead to the formation of a band structure (Figure 1. 1).[12] Electrons in semiconductors reside in the lower-energy valence band and are, crucially, restricted from entering the empty, higher-energy conduction band by the optical band gap, E_g.

Optical photoexcitation, triggered by a photon with at least energy E_g, can generate a bound electron-hole pair in semiconductors by giving an electron in the valence band, also known as the ground state, at least the requisite energy to overcome the band gap and occupy the conduction band, known as an excited state. The energy of this photon is inversely proportional to its wavelength, typically in the UV-vis region of the electromagnetic spectrum (~350 – 800 nm) for materials used in optoelectronic applications. The separation of electron-hole pairs produces charge-carriers, which are needed to generate electrical current. Electrons within the conduction band and holes left behind in the valence band can move freely, though certain material-dependent restrictions are present. In particular, the crystalline and morphological structure of a material has significant influence over the electronic structure and subsequent electronic behavior.

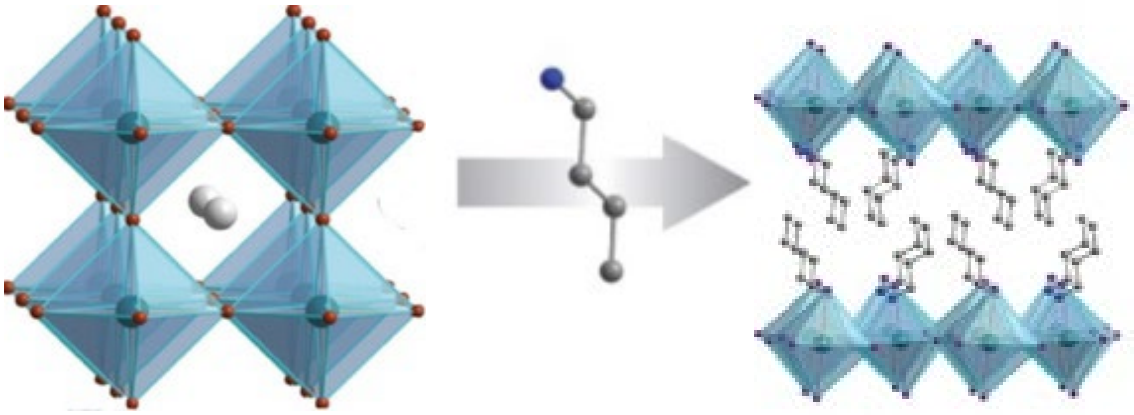

Figure 1. 2. Representative structures of hybrid perovskites and perovskite quantum wells. In 3D hybrid perovskites (left), A sites within the corner-sharing network of $[MX_6]^{2-}$ octahedra are occupied by organic cations instead of atomic cations. Larger organic cations separate layers of the octahedral framework, resulting in layered solids composed of inorganic quantum wells (right). Reprinted (adapted) with permission from reference.[13] Copyright 2019 American Chemical Society.

Hybrid organic-inorganic perovskites are a class of materials that exhibit perovskite connectivity, maintaining AMX_3 stoichiometry, but incorporate organic components into the corner-sharing octahedral framework (Figure 1. 2). Unlike their all-inorganic counterparts, hybrid perovskites contain an organic cation in the A site, the potential occupancy of which is dictated by the Goldschmidt tolerance factor.[14] Recently, researchers further refined this tolerance factor to better predict structures of hybrid perovskites, considering the oxidation states of cations as well.[15] Due to the hybrid nature of these crystals, with significant dielectric contrast between the organic and inorganic components, previous reports have found that overall crystal lattice is highly flexible, enabling unique electronic processes not otherwise found in typical all-inorganic three-dimensional bulk perovskites.[i]

[i] Compounds in solid materials often arrange themselves into frameworks known as a crystal *lattice* in order to lower their overall energy. The arrangements can range from highly-ordered, or crystalline, to a complete lack of structure at all, or amorphous.

Unlike 3D semiconductors, nanomaterials are electronically decoupled structures; by controlling material morphology during synthesis, materials could be synthesized such that their electronic wavefunctions were modified, and they experienced quantum confinement.[16, 17] In the resulting materials, whether colloidal or in extended solids, the dimensions of individual particles or layers are much smaller than the wavelengths of optical photons, thus restricting the typical pathways for interaction between a photon and the electrons within the material. Electronic processes become highly dependent on material morphology and size, most notably the optical band gap.[18]

Investigations into colloidal materials rapidly resulted in the development of nanoparticles with various compositions, sizes, and morphologies. Zero-dimensional nanoparticles, known as quantum dots, were utilized in a variety of fundamental, empirical studies aimed at understanding the effects of quantum confinement. Based on these seminal studies and further synthetic manipulations, new varieties of nanoparticles with lesser degrees of confinement (in only one or two dimensions) and intriguing morphologies were developed, such as nanorods, nanostars, and nanobipyramidal structures, among others. In particular, the incorporation of large cations into the A site of hybrid perovskites results in electronically decoupled layers of inorganic sublattice, resulting in two-dimensional (2D) perovskite quantum wells that are arranged in an extended bulk solid (Figure 1. 2) with increased ambient stability and an array of new properties enabled by quantum confinement. Further details with respect to structures of 2D PQWs and their relationships to 3D hybrid perovskites are discussed in Chapter 2.

With the advent of such astonishing new materials, well established theoretical models of the effects of quantum confinements and subsequent electronic wavefunctions in such materials

need more empirical evidence in order to be predictive. Given the direct influence of charge-carrier dynamics on the conversion efficiency of photons to electricity, fundamental studies of photophysics in these complex materials are crucial.

1.3 Photophysical Processes in Semiconductors

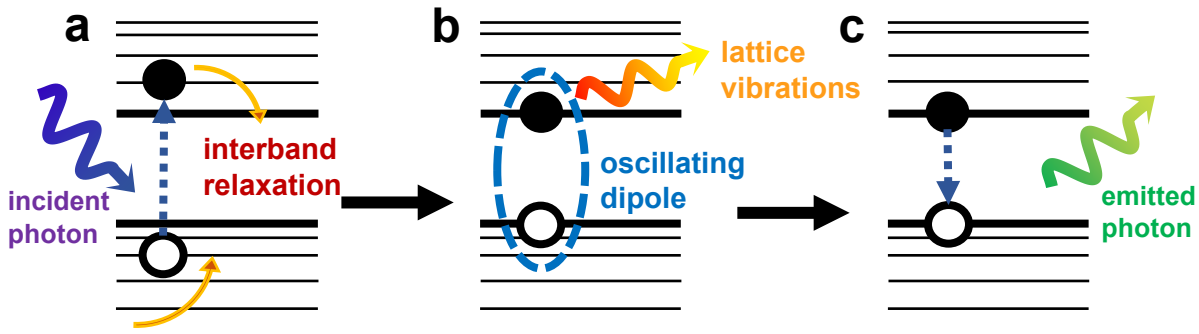

Figure 1. 3. Photoexcitation and subsequent electronic processes.
a) An incident photon with greater energy than E_g strikes a material, exciting an electron within the valence band to a higher energy state within the conduction band. The hot electron couples to vibrational modes, prompting interband relaxation. b) The electron and hole, of opposite charge, experience attractive forces, resulting in a lower energy bound state. Interband relaxation results in the release of heat in the form of coherent lattice vibrations. c) The electron and hole radiatively recombine, resulting in the emission of a photon, though various nonradiative relaxation processes may also be available and co-occur.

The interactions between light – photons, or electromagnetic waves – and matter – substances composed of subatomic particles including electrons – are dynamic processes. Upon photoexcitation of an electron in a material, many relaxation pathways immediately become available for the excited electron as it begins rapidly dispelling its energy. Based on empirical observations of electronic responses in a variety of materials, guiding principles for potential electronic behavior and possible photophysical processes in semiconductors were established. Several dominant, though by no means all, pathways in inorganic semiconductors are further discussed in this section.

In considering the electronic response of a semiconductor to photoexcitation, the energy of the incident photon is a significant factor. Photons without sufficient energy will not trigger an electronic transition in the material.[ii] However, a photon with requisite or greater energy can excite an electron from the valence band to the conduction band; the subsequent energy of the electron once in the conduction band is determined by the energy of the incident photon, as well as the available states *within* the conduction band and valence band, as shown in Figure 1. 3.

Additional energy levels within both the conduction and valence bands correspond to vibrational modes of the structure, as well as momentum along crystallographic directions in the lattice of the bulk solid or nanomaterial.[iii] In order to shed excess energy from an incident photon with greater energy than the band gap, "hot" electrons couple with these vibrational energy states in a process known as interband relaxation (Figure 1. 3a). Other relaxation pathways can exist for hot electrons and their counterpart holes or indeed can be restricted in order to prolong relaxation lifetimes, such as through synthetic manipulation or selective excitation using polarized incident photons, as desired for specialized optoelectronic applications.

When the small amount of energy in excess of the band gap contained by both the electron and hole is resonant with certain vibrational motions of the lattice, the energy is released as heat into the material as shown in Figure 1. 3b. Significant deposits of heat from interband relaxation processes can cause expansion and reorganization of the material, potentially altering the

[ii] Photons of lower energy can still trigger changes in the material by resonating with other aspects of the material that can interact with an external electric field. This is the principle by which microwave ovens operate, the meshed windows being too small for microwaves to pass through.

[iii] Coherent lattice vibrations are considered a quasi-particle in and of themselves, known as phonons. Excited electrons couple with optical phonons, which are able to interact with an external electric field. Optical phonons comprise displacements of charged, or partially charged, species within the lattice and can respond to low energy photons, typically in the infrared.

electronic structure. After relaxing to their respective band edges, the negatively charged electron and positively charged hole experience Coulombic attraction, the strength of which is determined by various material properties. In nanomaterials with high degrees of quantum confinement, attractive forces can result in bound quasi-particles, known as excitons. Exciton binding energies in nanomaterials range from tens to hundreds of meV, dictated greatly by the extent of quantum confinement experienced by the exciton.[19, 20] In materials with low exciton binding energies, such as most 3D semiconductors, electrons and holes instead act as "free" carriers, moving independently. Importantly, electron-hole pairs exhibit characteristics of an oscillating dipole, emitting electric fields that can influence the surrounding electronic structure in the material.

Electron-hole pairs that radiatively recombine at the band edge emit a photon with energy E_g in a process known as fluorescence (Figure 1. 3c). However, many nonradiative pathways often outcompete fluorescence in semiconductors, resulting in lower or completely quenched emission yields. Auger recombination, a multibody process in which a conduction band edge electron absorbs carrier energy to enter higher energy levels, can result in further lattice heating. Electrons can also fall into intermediary levels within the band gap known as "trap" states that lose energy as heat, although additional lower energy fluorescence emission from traps can also occur. These and other processes that generate heat within the material are often undesirable for optoelectronic devices, resulting in the loss of carriers that could otherwise be collected.

1.4 Monitoring Photophysical Phenomena using Ultrafast Spectroscopy

Electronic behaviors occur screamingly fast. The average snap of a finger lasts ~7 ms,[21] far shorter than the blink of an eye, but radiative recombination on such long timescales is exceedingly rare, especially in inorganic semiconductors. Understanding photophysical phenomena and

electronic responses to light are fundamental to the design of all optoelectronic applications, let alone solar cells – yet the ability to study fundamental properties of electronic responses to light remained elusive to scientists for decades, occurring on timescales that could not yet be physically measured. While laser sources implementing electronic gating mechanisms can operate on nanosecond and even picosecond timescales, femtosecond pulses are far too short to generate with electronics themselves. Robust, nonelectronic sources were needed in order to investigate ultrafast phenomena, leading to the Nobel Prize winning development in 1985 of chirped pulse amplification using nonlinear optics.[22] In selected materials, femtosecond pulses are generated entirely by the photophysical properties of the nonlinear optical materials, able to contain high intensity bursts of energy within their structure and steadily release packets of photons, or *pulses*, on femtosecond, and even attosecond, timescales. With decades of focused research efforts in the field of ultrafast spectroscopy, the expanded library of nonlinear optical oscillators that could withstand ultrashort optical pulses across photon energies enabled investigations of photophysical behavior across a variety of materials.

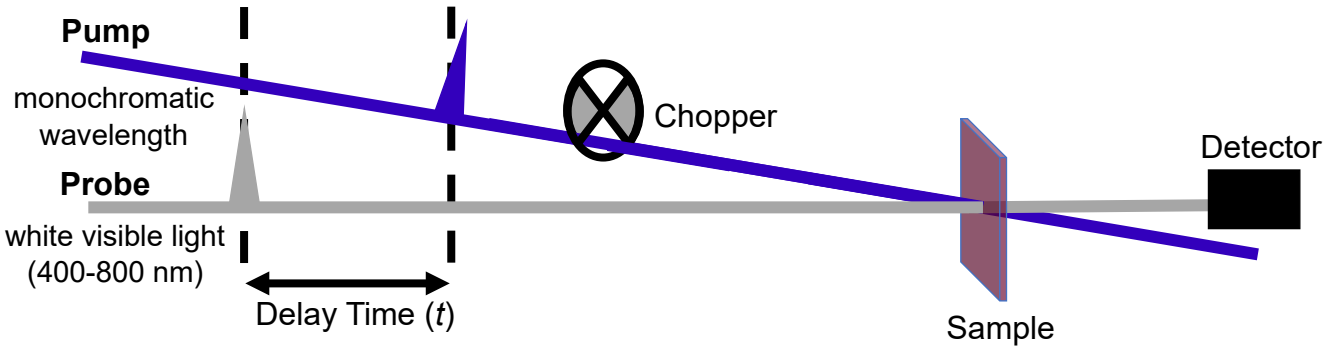

Figure 1. 4. Experimental geometry of transient absorption spectroscopy.
An optical pump of monochromatic wavelength photoexcites an electron in the sample from the ground state in the valence band to the excited state in the conduction band. At a specified time after the pump pulse excitation, the probe pulse hits the sample, and the detector collects the spectrum in this excited state. The chopper acts as a beam stop rotating at half the frequency of the pump pulse train, allowing for acquisition of a probe spectrum *without* pump excitation at each mechanical time delay to generate transient absorption spectra.

Typically, investigations of ultrafast processes utilize two beam paths that are both split from the originating source: an initial "pump" excitation, followed by a "probe" pulse. Each laser pulse is spaced out along the beam path and emitted at the repetition rate of laser, usually several hundreds to thousands of times a second. A sample is placed in the beam paths of both pulse trains, where they are spatially aligned onto the surface. The sample is first excited with the pump – a laser pulse that lasts for a defined length of time while encompassing a narrow range of photon energies. A population of electrons in the sample respond to the pump pulse, creating a temporarily modified electronic structure within the material.

A subsequent probe pulse, also occurring for a defined length of time, then hits the already excited sample at a designated time after the pump. Probe pulses are delayed relative to the pump, utilizing a change in distance to lengthen the path that photons must travel.[iv] By modifying the delay time between the pump and probe, electronic behavior can be observed at a series of time points following photoexcitation. Notably, probe pulses can span a larger range of wavelengths, allowing for measurement of electronic behavior across the chosen spectrum. Detectors are placed to collect the photons from the probe that are either transmitted, reflected, or emitted by the sample. In addition, the number of photons within the pump pulse, or *fluence*, can also influence electronic behavior, most notably by impacting the starting population of electrons that respond to the pump pulse. However, fluence-dependent trends vary by material, and offer further insight into the sample's electronic structure.

[iv] At $3 \cdot 10^8$ $m \cdot s^{-1}$, light travels 0.3mm in 1 ps. Probe pulses are mechanically delayed using a retroflector stage to maintain parallel paths that ensure delay in a single direction.

Figure 1. 4 shows the experimental setup of transient absorption, an ultrafast technique related to steady-state UV-vis absorption spectroscopy. In UV-vis absorption measurements, a white light probe monitors the ground state to excited state transition of electrons as a function of photon energy, spectrally averaged over a period of instrument time, usually a few seconds. In transient absorption experiments, a monochromatic pump,[v] with at least or greater than the E_g of the material, photoexcites electronic transitions in the material. Once the material has absorbed the pump, a probe containing visible energies monitors spectral changes after photoexcitation. Both the pump and probe pulses are ultrashort, irradiating the sample for a fraction of the time over which benchtop UV-vis instruments typically average data collections.

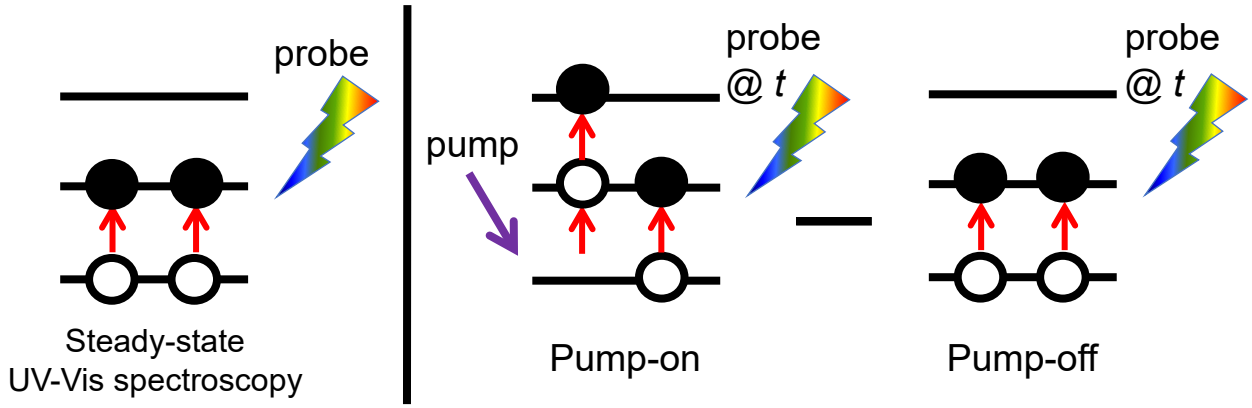

Figure 1. 5. Steady-state UV-vis versus transient absorption
In steady-state UV-vis spectroscopy (left), a broad spectrum of white light irradiates the sample, and the transmitted light is collected over a period of time. The light not detected is absorbed by the sample, an analysis of which photons were absorbed indicates ground state to excited state transitions. In transient absorption (right), two separate signals are collected and differenced. The first signal is collected when the pump pulse irradiates the sample and some, but not all, of the electrons in the ground state are excited. The following probe pulse further excites the electrons, as well as the remaining electrons in the ground state. The second signal, collected without the pump, is akin to steady-state UV-vis spectroscopy excepting that the probe pulse is ultrashort, resulting in time-resolved spectra.

[v] Due to the ultrashort nature of nonlinear pulses, the relationship between the length of the pulse and its spectral range is governed by the Heisenberg uncertainty principle. A fs pulse, as is typical with Ti:sapph oscillators, cannot have an exactly defined monochromatic wavelength, instead encompassing a Gaussian centered on the desired wavelength.

As shown in Figure 1. 5, transient absorption data is collected as the change in absorbance, ΔA, at each time, t, by comparing the absorbance spectra of the *probe* both with and without the pump as follows: $\Delta A = A(t_{\text{pump-on}}) - A(t_{\text{pump-off}})$. As some of the electrons in the ground state transition to the excited state and are "bleached" after the initial pump pulse, the main absorption features observed in steady-state UV-vis spectra appear as negative signals in transient absorption spectra.[vi] This is because the remaining electrons in the ground state, the ones that were unaffected by the pump, are fewer in number than before the pump pulse, resulting in a negative signal when compared to the probe spectrum without the pump pulse. Meanwhile, positive signals can indicate photoinduced absorption features, such as excited carriers transitioning to still higher states or valence band electrons that move to occupy holes in the ground state, among other complex origins. Lifetimes of electronic behavior can be calculated by fitting kinetic data collected along particular wavelengths and features, while spectral changes that are more difficult to isolate can require global fitting analyses.

[vi] "Bleaching" is in reference the loss of color, or photons of visible wavelengths, from ground state to excited state transitions.

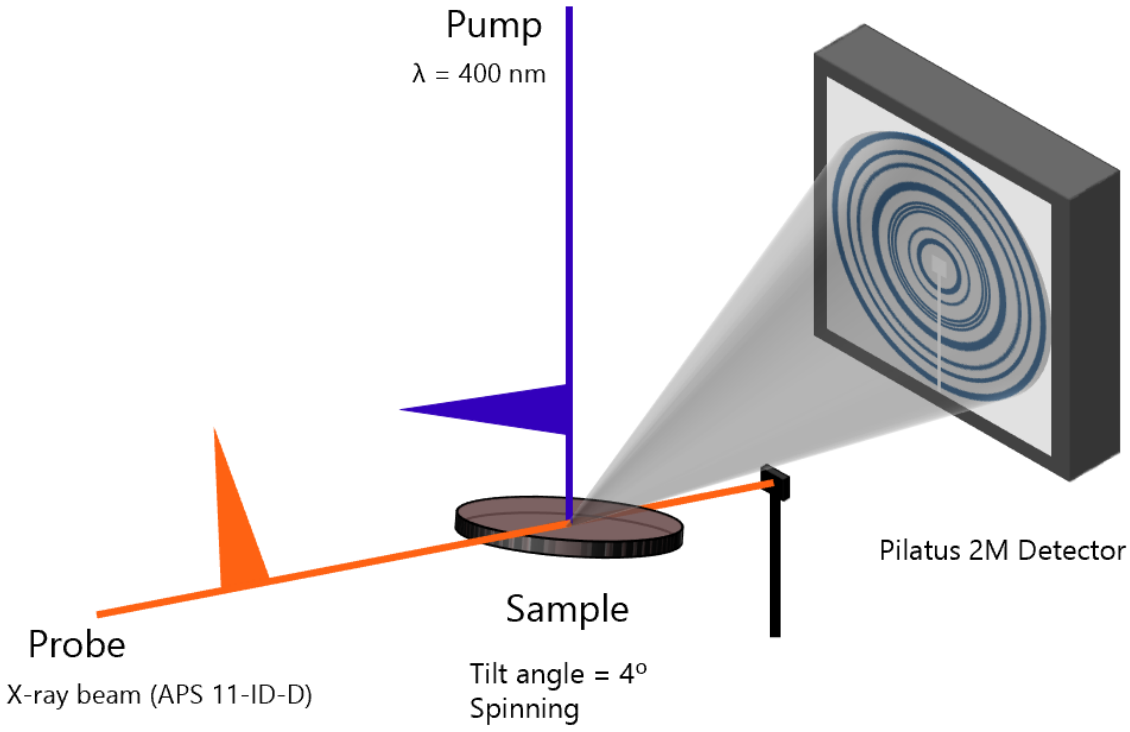

Figure 1. 6. Experimental geometry for time-resolved X-ray diffraction measurements. The laser pump and X-ray probe were orthogonally overlapped onto the surface of the spinning film, which was tilted at an angle of 4° to the incident X-rays. The Pilatus 2M detector was placed ~202 mm from the sample and temporally gated to measure scattering intensity only at the laser-synchronized probe pulses.

Unlike lower energy (UV-vis) probes such as those utilized in transient absorption, X-ray energies correspond to photons with wavelengths on the order of the atomic spacing within a crystal lattice. While visible photons have energies of 1-2 eV with wavelengths of 400-800 nm, incident X-rays used for time-resolved probes in this thesis were over 11 keV with wavelengths of ~0.1 nm. The interaction between incident X-rays and electrons can lead to constructive or destructive interference of their wavefunctions, resulting in diffracted X-ray scattering off the material surface to create a reflected pattern, as shown on the detector in Figure 1. 6. Diffraction patterns generated by measurement of a crystalline material are well-described by Bragg's Law as

follows: $n\lambda = 2d\sin\theta$, where n is the integer diffraction order, λ is the X-ray wavelength, d is the interatomic distance (commonly referred to as d-spacing), and θ is the scattering angle of diffraction. Time-resolved X-ray diffraction experiments employ an optical pump to photoexcite the sample followed by a monochromatic X-ray probe pulse to examine the dynamic changes in d-spacing and other lattice parameters at various time delays. Experiments were conducted at the Advanced Photon Source at Argonne National Laboratory (see Figure 1. 6), as currently available laboratory X-ray sources cannot generate picosecond X-ray pulses of sufficient intensity to detect small, structural changes in photoexcited diffraction patterns. Further discussion regarding time-resolved X-ray diffraction and data analysis can be found in Chapters 4 and 5 and Appendices C and D.

1.5 Scope of this Thesis

Whether colloidal or hybrid lead halide perovskite materials, two-dimensional (2D) semiconductors have been at the heart of recent advances in optoelectronic applications spanning photovoltaics,[23-25] lasers,[26-28] photocatalytic cells,[29-31] and light-emitting diodes (LEDs).[32, 33] The outstanding performance of 2D materials in these applications can be attributed to their unique electronic structures with quantum confinement in only one direction, offering control over optical properties[13] and rates of charge-carrier processes.[34] However, the quantum confinement of these materials also results in high exciton binding energies,[35] anisotropic conductivity,[36] and low carrier mobilities;[37] these properties can impede efficient charge-carrier separation and transport which are crucial to optimal device performance. Most recent research efforts in addressing these issues for 2D materials have focused on optimizing device architecture,[38] though purposeful exploitation

of fundamental photophysical properties has been shown to boost performance in devices by enabling photon upcycling,[39] wavelength downconversion,[40] and energy-funneling.[41-44]

In the work herein, fundamental photophysical properties of 2D materials and related analogs are investigated to better direct material design of these materials for desired optoelectronic purposes. Systematic trends between material structure and electronic behavior are examined across compositional series, tuning for multiple variables to improve theoretical photophysical models. Rates of energy transfer in 2D perovskite quantum wells were investigated as a function of the distance between quantum wells, generating empirical results that aligned well with theoretical calculations. The effects of polarized excitation in enhancing and prolonging the spin-coherent electronic response in 2D nanoplatelets were examined, identifying features with respect to the morphology of the particles that greatly improve lifetimes of spin-coherence. Finally, studies of the dynamic structural response in 3D hybrid perovskites to photoexcitation revealed non-equilibrium phase transitions, highlighting the complex relationship between organic and inorganic components in hybrid perovskites, as well as the correlated responses of the crystal lattice and electronic structure.

Chapter 2. Distance Dependence of Förster Resonance Energy Transfer Rates in 2D Perovskite Quantum Wells via Control of Organic Spacer Length

Reprinted with permission from "Shobhana Panuganti, Lucas V. Besteiro, Eugenia S. Vasileiadou, Justin M. Hoffman, Alexander O. Govorov, Stephen K. Gray, Mercouri G. Kanatzidis, and Richard D. Schaller. *J. Am. Chem. Soc.* **2021** *143* (11), 4244-4252."

2.1 Abstract

Two-dimensional semiconductors are attractive candidates for a variety of optoelectronic applications owing to the unique electronic properties that arise from quantum confinement along a single dimension. Incorporating non-radiative mechanisms that enable directed migration of bound charge-carriers, such as Förster resonance energy transfer (FRET), could boost device efficiencies provided that FRET rates outpace undesired relaxation pathways. However, predictive models for FRET between distinct 2D states are lacking, particularly with respect to the distance *d* between a donor and acceptor. We approach FRET in systems with binary mixtures of donor and acceptor 2D perovskite quantum wells (PQWs), and we synthetically tune distances between donor and acceptor by varying alkylammonium spacer cation lengths. FRET rates are monitored using transient absorption spectroscopy and ultrafast photoluminescence, revealing rapid picosecond lifetimes that scale with spacer cation length. We theoretically model these binary mixtures of PQWs, describing the emitters as classical oscillating dipoles. We find agreement with our empirical lifetimes and then determine the effects of lateral extent and layer thickness, establishing fundamental principles for FRET in 2D materials.

2.2 Introduction

Two-dimensional (2D) semiconductors offer prospective benefits for optoelectronics devices spanning photovoltaics, lasers, and light-emitting diodes[27, 45-50] due to tunable quantum and dielectric confinement effects that facilitate control of electronic band gap and often give rise to strong band-edge absorption in addition to spectrally narrow photoluminescence.[13, 51] However, 2D materials also typically exhibit large exciton binding energies, anisotropic conductivity, and low carrier mobilities, which can impede energy and carrier migration compared to bulk phases. Förster resonance energy transfer (FRET) offers the prospect of rapid exciton migration in 2D materials that can potentially outpace other undesirable excited-state relaxation channels such as carrier trapping, radiative recombination, and even multiexciton annihilation processes.[52, 53] Fast FRET presents an opportunity to bolster the utility of 2D materials, offering routes to defect-tolerant devices and enabling novel energy-funneling architectures.[39, 40, 44, 54]

The probability of FRET occurring between an excited donor and ground-state acceptor depends on the spectral overlap integral and electronic coupling, affected by donor−acceptor distance *d*, between states.[55] However, Förster theory models donor and acceptor states as point dipoles, and while appropriate for molecular and quantum dot (QD) systems, it cannot describe energy transfer between states with 2D spatial extent (see Figure 2. 1a). The generalization of Förster theory to higher dimension structures requires an empirical investigation to guide and test models.[56, 57] Experimental studies of FRET in 2D systems, such as colloidal nanoplatelets, graphene, and transition metal dichalcogenides, have indicated rapid lifetimes on hundreds to few picosecond time scales.[58-67]

To this end, 2D perovskite quantum wells (PQWs) with mixtures of different *n* thicknesses and, therefore, different energy gaps present promising experimental systems for studies of Förster theory in 2D systems. PQWs form upon the incorporation of large, organic cations into the bulk hybrid perovskite framework, which introduces low-dielectric organic barriers between layers of PQWs.[68] The resulting materials are composed of precisely *n* octahedra in each PQW along the stacking axis and exhibit the general formula $A'_2A_{n-1}M_nX_{3n+1}$ where A′ is the larger "spacer" cation constituting the organic barrier, A is the small organic cation occupying the perovskite cage, M is the divalent metal, and X is the halide.

At present, reports focused on 2D PQWs offer disparities regarding FRET rates, though examined sample structures and mixture identities vary among these studies.[69-72] One report, which examined a broad distribution of n thickness PQWs that inclusively spanned $n = 2$ to $n = 6$, reported femtosecond FRET time scales between different *n* layers.[72] Other recent studies of 2D PQWs containing different A′ cations and ranges of n thickness observed remarkably longer hundred-picosecond time scales.[70, 71] The results in each of these reports encounter complications arising from multiple undefined pairings of donor and acceptor species, overlapping spectral signatures that inhibit distinctly correlated dynamics of donor energy outflow with acceptor inflow, and the absence of isolated *n* samples.

To advance the understanding of spatial dimensionality effects on rates of FRET in 2D PQWs and in materials of varying dimensionality generally, studies of energy transfer rates with individually resolved donor and acceptor dynamics in binary donor−acceptor mixtures are crucial.[73, 74] Despite rapid progress in device fabrication and performance, synthetic methods for 2D PQW films containing a single *n* domain and controlled mixtures of *n* phases are

underdeveloped, in particular for materials over a range of A′ cations that would enable one to study energy transfer as a function of distance between layers of 2D PQWs.[70, 75, 76]

In this study, we develop synthetic procedures to achieve both neat and binary mixed films comprising $n = 1$ and $n = 2$ alkylammonium lead halide 2D PQWs and probe energy transfer rates with ultrafast spectroscopy. Femtosecond transient absorption reveals correlated donor and acceptor dynamics that indicate FRET. Time-resolved photoluminescence studies are also performed, suggesting an absence of measurable charge transfer and further supporting energy transfer. We then probe FRET as a function of distance between donor and acceptor PQWs through systematic increases in carbon chain length of A′ site alkylammonium cations. The interlayer spacing between PQWs is directly affected by the steric properties of the organic cation in the A′ site; in our approach, we exploit this inherent structural feature to precisely tune the distance between layers, in particular employing butylammonium (BA), hexylammonium (HA), and octylammonium (OA) with A site methylammonium (MA) cation for n = 2 phases. Next, we construct a theoretical model of these systems and obtain results consistent with our experimental findings, observing rapid picosecond lifetimes that outpace earlier reports of Auger recombination in these materials.38,39 We model other synthetically adjustable parameters of 2D materials, gathering results that suggest FRET lifetimes show little dependence on the isolated tuning of the lateral extent and thickness of the quantum wells. Thus, our work herein begins to build the necessary foundation for predictive models of FRET in 2D PQWs and further guides design principles for employing FRET in devices fabricated from 2D materials.[77, 78]

2.3 Results and Discussion

Crystalline samples of phase-pure $n = 1$ and $n = 2$ for each material $(BA)_2MA_{n-1}Pb_nI_{3n+1}$, $(HA)_2MA_{n-1}Pb_nI_{3n+1}$, and $(OA)_2MA_{n-1}Pb_nI_{3n+1}$ were synthesized according to previously published methods.[79, 80] Briefly, lead oxide was dissolved into hydroiodic acid and heated to boiling while stirring to afford a bright yellow solution. Hypophosphorous acid and the appropriate ratio of alkylamine and methylammonium chloride necessary to produce the desired n phases (n = 1, 2) were then added to the reaction mixture. Large flake-like crystals, precipitated upon cooling, were vacuum filtered, washed with diethyl ether, and stored in an evacuated desiccator. Powder X-ray diffraction (Figure A. 1) of the crystalline materials compared with calculated patterns indicated phase-pure products, showing characteristic peaks in both $n = 1$ and $n = 2$. These phase-pure crystals were then used as precursors for the preparation of both neat and binary films to obtain control over donor and acceptor density in film mixtures as well as to preclude formation of $n = 3$ or thicker PQWs. Binary films were produced by dissolving both $n = 1$ and $n = 2$ crystals into dimethylformamide (DMF) in a nitrogen atmosphere and spin-coating at 4000 rpm for 30s onto clean, preheated (110°C) glass substrates.

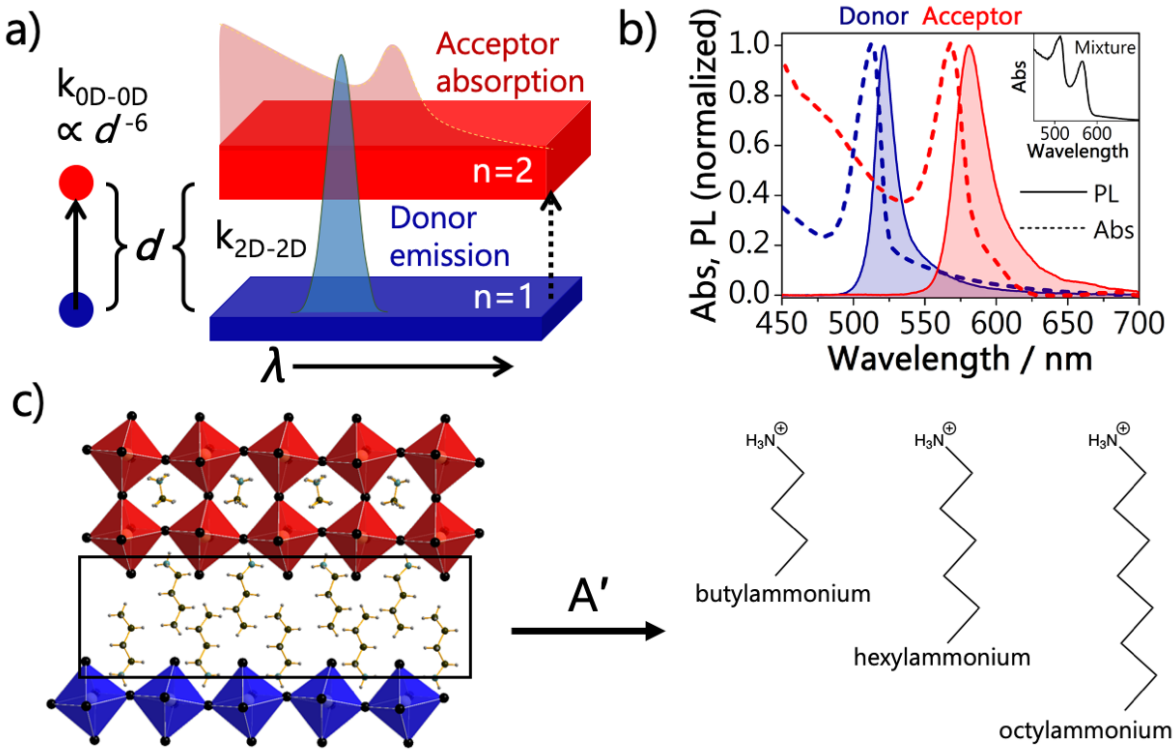

Figure 2. 1. Static characterization of 2D PQWs.
(a) Förster theory describes energy transfer between point dipoles with FRET rates (k_{0D-0D}) scaling with the distance (d) between the donor and acceptor. The 2D spatial extent of 2D PQWs with requisite spectral overlap is hypothesized to increase FRET rates (k_{2D-2D}) owing to the increased effective density of the acceptor, but quantitative theoretical and empirical models have not been developed. (b) Absorption and photoluminescence spectra of donor (n = 1) and acceptor (n = 2) phases of $(BA)_2MA_{n-1}Pb_nI_{3n+1}$. (c) Structural visualization of a donor and acceptor interface in a binary mixture showing layers of $[PbI_6]^{4-}$ octahedra where n = 1 (blue) and n = 2 (red) are separated by the A′ site cation. Molecular structures of the A′ cations used in this study to change the distance of separation between layers are shown at right.

Figure 2. 1b shows absorption and photoluminescence spectra of the neat BA n = 1 donor and n = 2 acceptor films with notable spectral overlap of donor emission and acceptor absorption. Several routes to binary films were examined, and our preferred method of film preparation was adapted from previously reported hot-casting methods in which substrates are preheated before spin-coating to produce well-oriented, homogeneous materials on the substrate

surface.[46] The utilization of higher concentrations of n = 1, in which methylammonium is not present, was expected to inhibit the growth of higher n domains by limiting the amount of methylammonium available for thicker PQW growth. The higher relative ratio of n = 1 to n = 2 yields a donor-saturated system and a lower limit of FRET rates for the system wherein donors tend to experience a single adjacent acceptor. Importantly, mixtures of n = 1 and n = 2 PQWs retained distinct spectral features of the donor and acceptor (Figure 2. 1b, inset). Furthermore, binary film absorption spectra conveyed the absence of secondary phases such as higher n PQWs, which would appear at redder wavelengths. Powder X-ray diffraction patterns of the binary BA films correspondingly indicated only the presence of n = 1 and n = 2 phases (Figure A. 2). Structural and optical characterization of HA and OA films are included in Appendix A.

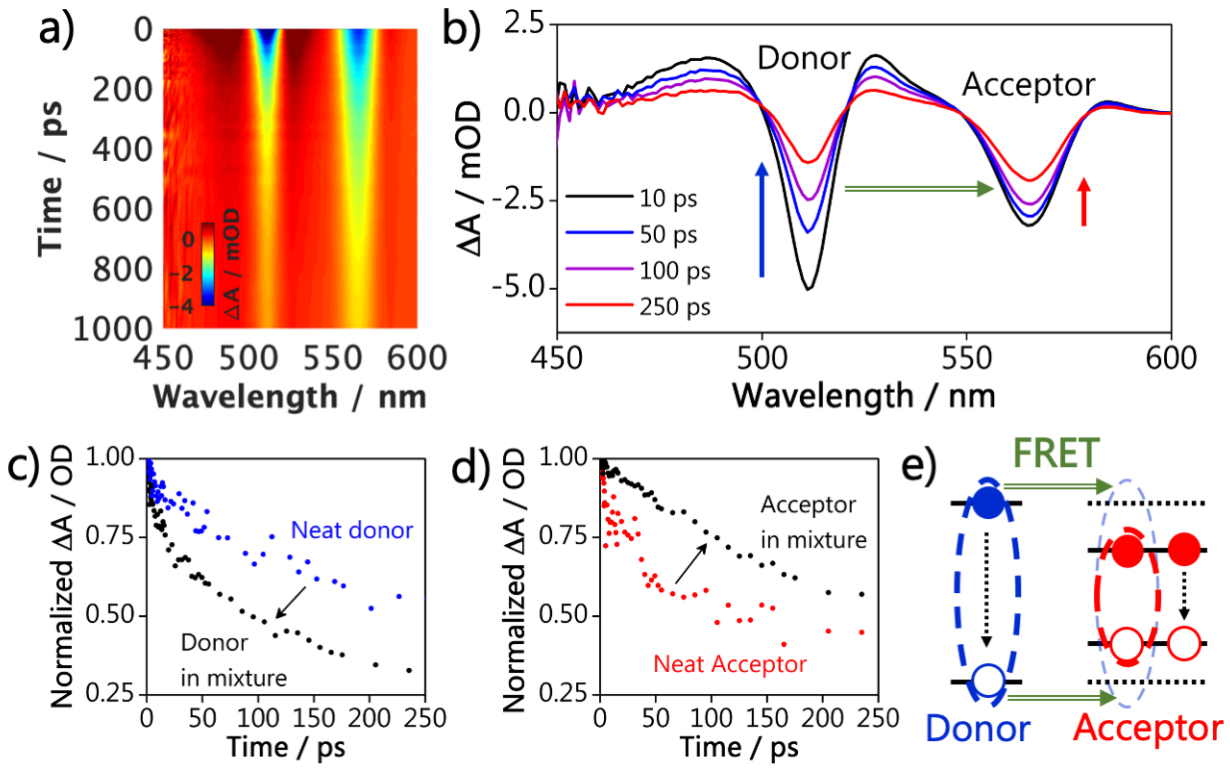

Figure 2. 2. Dynamic optical measurements of BA n = 1 and n = 2 phase-pure and mixed composition films by transient absorption.
(a) Time-resolved absorption spectral map as a function of probe wavelength showing strong negative ΔA signals upon excitation at 512 and 565 nm, which are the main absorption lines of the donor and acceptor components, respectively. Spectra shown are the average of three scans. (b) Transient absorption spectra of the mixed film at 10, 50, 100, and 250 ps with the ground-state bleach signal of the donor decaying much more rapidly compared to the acceptor. (c) Normalized decay dynamics at 496 nm from neat n = 1 and the mixture for the donor. (d) Normalized decay dynamics at 565 nm from neat n = 2 and the mixture for the acceptor. (e) Upon 400 nm excitation, both donor (blue) and acceptor (red) components in the mixture generate excitons, resulting in "bleaching" or a negative ΔA signal, of ground-state transitions. In the mixture, the donor exciton population rapidly decreases as excitons isoenergetically transfer into the acceptor, resulting in a faster decay of the donor in the mixture than the neat donor (c). The energy transfer also increases exciton population in the acceptor after excitation, resulting in a slower decay of the acceptor in the mixture than the neat acceptor (d).

Next, we performed femtosecond transient absorption (TA) spectroscopy using 35 fs laser pulses for both single- component films of donor or acceptor as well as binary films. TA facilitates the observation of any especially rapid processes that relate donor population outflow to acceptor

inflow. In these studies, we implemented low-fluence (2.13 μJ • cm^{-2}) excitation to avoid multiexcitonic processes that can complicate analysis as they potentially could occur on similar time scales as FRET. Figure 2. 2a shows time-resolved changes in absorption (ΔA) signals as a function of probe wavelength for a binary BA film (neat BA films are shown in Figure A. 5). Above-band gap excitation at 400 nm results in "bleaching" of ground-state populations in both n = 1 and n = 2, seen as negative ΔA signals in Figure 2. 2a,b at 513 and 565 nm, respectively. In addition, induced absorption signals appear at a higher energy of each bleach. Owing to the concern that broad n = 2 induced absorption signals overlap with the n = 1 bleach, here, we analyze n = 1 at the induced absorption feature at 496 nm. Kinetics data in Figure 2. 2c,d monitored at 496 and 565 nm are shown normalized at 1 ps following intraband relaxation of carriers and other convoluting processes such as optical Stark shifts.[81]

Donor transient optical signals clearly decay more rapidly in the binary mixture relative to the neat film (Figure 2. 2c). In addition, acceptor kinetics monitored at the 565 nm ground- state bleach feature show notably slower decay signals consistent with FRET for the acceptor PQWs in the mixture relative to the neat n = 2 film (Figure 2. 2d). These observations of shorter donor lifetime and correlated extended acceptor lifetime in the binary mixed film, as compared to the neat materials, convey exciton population transfer from donor to acceptor states via FRET. Importantly, rates of excited-state decay for n = 2 acceptors were also obtained using 545 nm excitation, as opposed to 400 nm, to selectively excite acceptors in the binary films as a means to control for potentially consequential environmental or material-processing influences relative to the neat n = 2 acceptor films. 545 nm is below the energy gap for n = 1 and was verified to not excite n = 1 in the neat donor films, thus allowing us to examine n = 2 dynamics.

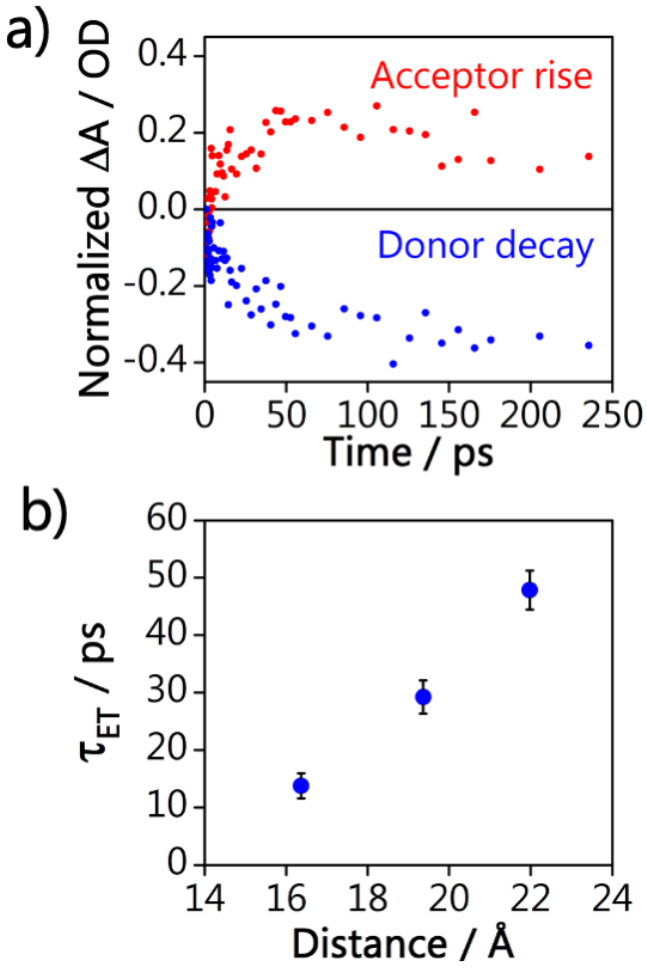

Figure 2. 3. Energy transfer in mixed films.
(a) Isolated decay in $n = 1$ donor and rise in $n = 2$ acceptor lifetimes shown for the BA binary film. (b) Fitted lifetime values for isolated FRET dynamics as a function of approximate distance from the center to center of $n = 1$ and $n = 2$ layers within the mixed film.

Rates of FRET were obtained by differencing the normalized neat donor and acceptor decay dynamics from the corresponding measurements performed for binary mixed films. By differencing the neat film dynamics from mixed film dynamics for each n phase, we account for intrinsic electronic processes of the individual n phase in the absence of other phases and isolate the emergent energy transfer dynamics. Figure 2. 3a shows the isolated rise in the acceptor and

decay in the donor for the BA spacer with a time constant of 14 ± 2 ps. Such correlated dynamics are consistent with the conclusion that rapid FRET occurs in these films and is competitive with other nonradiative pathways that could otherwise quench donor states. However, correlated transient absorption dynamics can also occur for other charge-carrier migration pathways, such as electron transfer. To determine whether a contribution from charge transfer is operative, we performed time-resolved photoluminescence measurements. Unlike charge transfer, FRET results in the migration of the entire exciton from the donor into the acceptor state (see Figure 2. 2e) and can induce sensitized acceptor emission to which time-resolved photoluminescence is sensitive, whereas charge transfer at low excitation fluence quenches emission. Figure A. 6 shows representative time-resolved photoluminescence and a dynamic response from both mixed and neat OA films. This data again exhibits correlated donor decay and acceptor rise dynamics, supporting FRET and not charge transfer, on similar time scales as noted in transient absorption.

Transient absorption measurements were repeated for the full range of A′ spacer cations, including neat donor, neat acceptor, and binary mixed films, in order to gain experimental understanding of FRET scaling in 2D PQW materials. The donor−acceptor distance, here defined as the center of a donor layer to the center of an acceptor layer, was determined from single-crystal diffraction as functions of each A′ site cation, and additional details regarding the determination of these distances can be found in Appendix A. For progressively longer spacer lengths of 16.4, 19.4, and 21.9 Å, respectively, FRET lifetimes of 14 ± 2, 29 ± 3, and 48 ± 3 ps were obtained from fitting donor-derived decays and are shown in Figure 3b. As such, FRET rates decrease with increasing distance for 2D PQWs in a nonlinear fashion as the electromagnetic coupling between the donor and acceptor decreases.

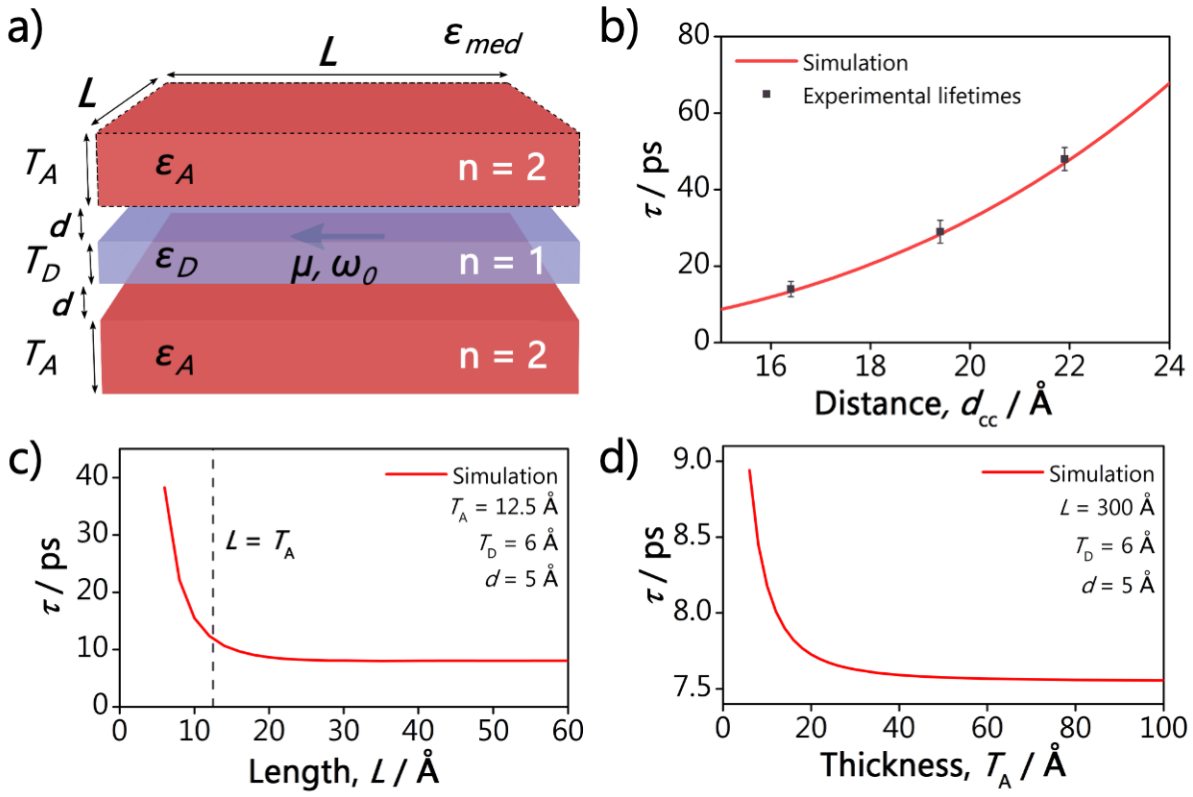

Figure 2. 4. Results of computational modeling for FRET in PQW systems.
(a) Schematic diagram of the computational model for the system, also noting its geometrical parameters. The system is composed of three stacked slabs with the $n = 1$ donor slab in the middle. The dashed lines surrounding the top $n = 2$ acceptor slab indicate the volume used for the integral in eq 1. (b) Comparison of the experimentally measured lifetimes with the values obtained from the simulated model. (c) Theoretical average lifetimes with respect to changes in the PQW length. The dashed line marks the value at which the length of the PQWs is the same as the acceptors' thickness; i.e., it becomes a cube. Above this value, the system rapidly reaches a stable value. (d) Theoretical average lifetimes with respect to changes in the acceptor PQW thickness.

The observed trend in FRET lifetimes as a function of distance was compared to a computational model we developed to describe FRET in 2D materials. The model considers the PQWs as discrete three-dimensional slabs, where the radiative emission of the donor PQW is described by a classical oscillating dipole operating at its emission wavelength, $\lambda_{PL} = 525$ nm (see Figure 2. 1b). The resulting electric fields in the materials are determined numerically using COMSOL Multiphysics software. The geometrical configuration of this model, shown in Figure

2. 4a, stacks three PQWs along the z direction with a $n = 1$ donor between two $n = 2$ acceptors. Importantly, they are separated by the distance d that accounts for the molecular spacers used in the experimental samples. The strength of the donor dipole is taken as $\mu = 2.5$ eÅ, a value guided by a previous report.[82] We calculated the FRET rate by considering the electromagnetic absorption at the acceptor slabs in a system excited by a dipole situated at the center of the donor slab (see Figure 2. 4a) using the expression:[60, 72]

$$k_{\mathrm{FRET}} = \frac{2}{\hbar}\varepsilon_0 \mathrm{Im}[\varepsilon_{\mathrm{A}}] \int_{\mathrm{A}} |E|^2 \, \mathrm{d}V \tag{1}$$

where ε_0 and ε_{A} are the permittivity of free space and the relative permittivity of the acceptor PQW, respectively. The volume integral of the electric field generated by the dipole inside the donor PQW is evaluated over the volume of the acceptor PQW, denoted as A, and surrounded by a dashed black line in Figure 2. 4a. From this magnitude, we obtain theoretical lifetimes of the excited state in the donor PQW as $\tau = 1/k_{\mathrm{FRET}}$. Lastly, we use a single-oscillator Lorentz model to define the permittivity of the slabs with parameters chosen to maintain consistency with previously reported dielectric constant values for similar materials.[19, 83] In defining the dielectric constant this way, i.e., with shifted absorption lines between the $n = 1$ and n = 2 layers denoting their respective values, we introduce information about the different strengths of quantum confinement in each subsystem. The permittivity of the simulated slabs is then given by

$$\varepsilon_r = \varepsilon_\infty + \frac{\omega_{\mathrm{p}}^2}{\omega_0^2 - \omega^2 - 2i\omega\gamma} \tag{2}$$

The resulting FRET lifetimes we obtained through both the empirical and theoretical approaches are rapid, outpacing previously reported Auger recombination lifetimes of ~80 ps in similar materials.[77, 78] However, these FRET rates appear slower than in other binary and multiple

mixed layer systems, such as those reported by Proppe *et al.*,[72] perhaps owing to the smaller donor−acceptor spectral overlap of the binary system studied herein. Given the same materials, lateral sizes, and spacing, we would expect the FRET rates between $n = 2$ donors and $n = 3$ acceptors as well as consecutive sequences of larger layer n thicknesses to be higher as the result of the reduced difference between their electronic state shifts due to deviation from the expected trend for distance dependence in 2D systems.

In Figure 2. 4b, we present theoretical results for the FRET lifetimes as we change the spacing d between the PQWs. The x-axis is presented in terms of center-to-center distance, d_{cc}, between the PQWs in order to offer a consistent description with the experimental data in Figure 2. 3b, which is also included in this plot. We note that the experimental and theoretical data are in good agreement, indicating that the alkylammonium cations used in the experiment effectively behave as spacers and thus affect FRET rates. Furthermore, the experimental data and model show FRET rates that rapidly decrease with increasing distance between the donor and acceptor. Fitting of these rates indicates that they scale with the center-to-center distance between the PQWs as approximately d_{cc}^{-4}, a trend observed in some reports involving 2D donor or acceptor states[56, 58, 59, 66, 67] but not observed for others.[62, 64] Other factors, such as dielectric screening at the donor[62] and extended acceptor morphology,[60, 64] can impact FRET rates and result in quantum confinement.

Our model goes beyond describing FRET between point- like dipoles in infinite 2D slabs. It also allows us to explore FRET for particular finite slab geometries that are subject to synthetic manipulation, such as lateral area control.[84] We calculated the impact of finite lateral area on the transfer time for a single FRET event. The numerical results of FRET lifetime versus PQW side

length, L, are presented in Figure 2. 4c for a donor−acceptor separation of d = 0.5 nm. We observe prompt convergence spanning from $\tau \approx 40$ ps at L = 0.5 nm to values approximately an order of magnitude lower, such as those observed in Figure 2. 4b, when we consider values of L > 2 nm. At values of $L \leq d = 1.25$ nm, the system effectively approaches QD-like behavior rather than 2D quantum well characteristics. In this calculation, we neglect effects that the small lateral extent would imply with respect to the quantum confinement experienced by the particles. From this data, we conclude that, from the perspective of the geometrical coverage of donor PQWs by the acceptor ones, we should not expect changes in the typical time scale of a FRET event with further increases in PQW area.

Given the rapid decay of the electric field of the classical oscillating dipole, the extension of the thickness of a PQW beyond the immediate proximity of the original excitation has a negligible effect on FRET rates given otherwise fixed acceptor properties, as seen in Figure 2. 4d. However, although these data capture the dependency of the FRET rates on the spatial distribution of matter, they again do not specifically account for the effect of quantum confinement as a function of changing morphology. Nonetheless, from the combined evidence of Figure 2. 4c,d, one could argue that the slab thicknesses depicted in Figure 2. 4a and used to compute Figure 2. 4b virtually maximize the FRET rate for a given spectral overlap as modeled by eq 1. In other words, from the perspective of this theoretical model, the PQW geometry observed in the experimental samples provides almost maximal FRET transfer rates for a given material pairing and interlayer distance, and neither extending the layer length nor stacking additional $n = 2$ acceptor layers should substantially alter FRET rates. Additional results of the theoretical model with respect to other parameters, such as dipole strengths and relative orientations, are included in Appendix A.

2.4 Conclusion

The controlled variation of the A′ site cations in $n = 1$ and $n = 2$ phases of 2D PQWs was successfully implemented as a nanoscopic tool for modifying electronic energy migration with respect to distance between donor and acceptor states with two-dimensional spatial extent. Having prepared binary, controlled mixtures for the examination of the scaling of FRET with distance, we obtained donor-derived lifetimes of 14, 29, and 48 ps for distances of 16.4, 19.4, and 21.9 Å, respectively. Computationally derived lifetimes for FRET are in agreement with empirical data for 2D PQWs, indicating FRET lifetimes that scale with distance as d^{-4} for PQWs presenting a large lateral extent and moderate spectral overlap between donor and acceptor states. Importantly, overcoming the synthetic challenges posed in the pursuit of the controlled donor and acceptor mixtures of higher n layers for FRET studies will prove beneficial for ongoing and future studies of applications in which films are implemented. In that way, the extension of the empirical model for scaling FRET with distance could include consecutively longer alkylammonium cations that would increase the distance between layers. Overall, the synthetic and spectroscopic methods employed in this work for obtaining phase-pure and mixed-phase 2D PQW film and resultant ultrafast dynamics of FRET afford extensive control for factors that affect electronic processes, thus showing improved understanding of charge-carrier behavior. Such understanding and vetted modeling opens possibilities for fast, even multiexcitonic, FRET manipulations on ultrafast time scales through the implementation of 2D materials.

Chapter 3. Excitonic Spin-Coherence Lifetimes in CdSe Nanoplatelets Increase Significantly with Core/Shell Morphology

Reprinted with permission from "Phillip I. Martin, Shobhana Panuganti, Joshua C. Portner, Nicolas E. Watkins, Mercouri G. Kanatzidis, Dmitri V. Talapin, and Richard D. Schaller. *Nano Letters* **2023** *23* (4), 1467-1473."

3.1 Abstract

We report spin-polarized transient absorption for colloidal CdSe nanoplatelets as functions of thickness (2–6 monolayer thickness) and core/shell motif. Using electro-optical modulation of co- and cross-polarization pump–probe combinations, we sensitively observe spin-polarized transitions. Core-only nanoplatelets exhibit few-picosecond spin lifetimes that weakly increase with layer thickness. The spectral content of differenced spin-polarized signals indicate biexciton binding energies that decrease with increasing thickness and smaller values than previously reported. Shell growth of CdS with controlled thicknesses, which partially delocalize the electron from the hole, significantly increases the spin lifetime to ∼49 ps at room temperature. Implementation of ZnS shells, which do not alter delocalization but do alter surface termination, increased spin lifetimes up to ∼100 ps, bolstering the interpretation that surface termination heavily influences spin coherence, likely due to passivation of dangling bonds. Spin precession in magnetic fields both confirms long coherence lifetime at room temperature and yields the excitonic *g* factor.

3.2 Introduction

Colloidal II−VI semiconductor nanoplatelets (NPLs) constitute attractive candidates for a wide variety of optoelectronics owing to their unique band structure that derives from quantum confinement along a single direction in addition to narrow absorption and emission line widths that arise from perfect ensemble thickness control with well-defined surface facets.[84-88] This material class, and other morphologically similar semiconductors such as two-dimensional (2D) halide perovskites, have garnered interest for their unique spin polarization properties owing to highly controlled material features including tailored thickness of the inorganic semiconductor and, for the II−VI materials, established routes to replace synthetic organic ligands with dielectric inorganic shells.[89-93] In addition to tuning quantum well thickness, altering particle surface characteristics and controlling electron−hole overlap offer routes to influence spin-depolarization pathways, such as through interaction with surface dangling bonds, which may yield increased spin coherence lifetimes of benefit to spintronics.[94-96]

A recent study of colloidal 2D CdSe nanoplatelet quantum wells upon excitation with a circularly polarized pump and cross-polarized probe revealed a short-lived induced absorption at lower-energy wavelengths than the ensemble absorption feature.[87] The red-shifted absorption arises from Coulombic stabilization of biexcitons that show selectivity for the cross polarized pump−probe combination over the period of time for which pump-induced spin polarization is preserved. Relatedly, copolarization of circular pump and probe leads to delayed growth of lower-energy differential induced absorption during the period in which scattering randomizes spin. Such spectral features enable characterization of lifetimes and mechanisms for spin-depolarization of

photogenerated excitons that can help to develop understanding regarding fundamentals of exciton dynamics in these materials.[85, 92, 93, 97]

In this report, we perform circularly polarized transient absorption spectroscopy on CdSe NPLs as well as CdSe/CdS and CdSe/ZnS core/shell NPLs in order to discern trends regarding the lifetime of spin-polarization upon increasing particle thickness or shell layer thickness. We observe that as NPL thickness increases from three to six monolayers (MLs) in core-only structures, the spin coherence lifetimes increase proportionally, but fitted lifetimes remain < 2 ps; the 2 ML CdSe NPL sample behaves anomalously, which may relate to appreciably altered lattice properties of this thinnest sample. Circularly polarized TA spectra for these structures convey biexciton binding energies when compared to static absorption and here are found to be smaller than previously suggested. Spin-polarization lifetimes increase appreciably upon addition of CdS shell layers to tens of picoseconds. CdS shell growth simultaneously yields surface modification in addition to reduced electron−hole overlap, both of which may increase spin lifetimes. Remarkably, we find that a single ZnS monolayer shell that does not appreciably alter electron−hole overlap also increases spin polarization lifetime significantly, suggesting the key importance of competing surface bonding effects that perhaps dominate electron−hole pair delocalization. Transient Faraday rotation measurements in static magnetic fields further confirm that observed signals arise from spin polarization, and precession frequencies afford the exciton *g* factor. These findings show that NPL morphology plays an appreciable role in stabilizing exciton spin orientation and can serve to decrease the availability of spin-decay pathways in ways that warrant further examination to achieve technological benefit.

3.3 Results and Discussion

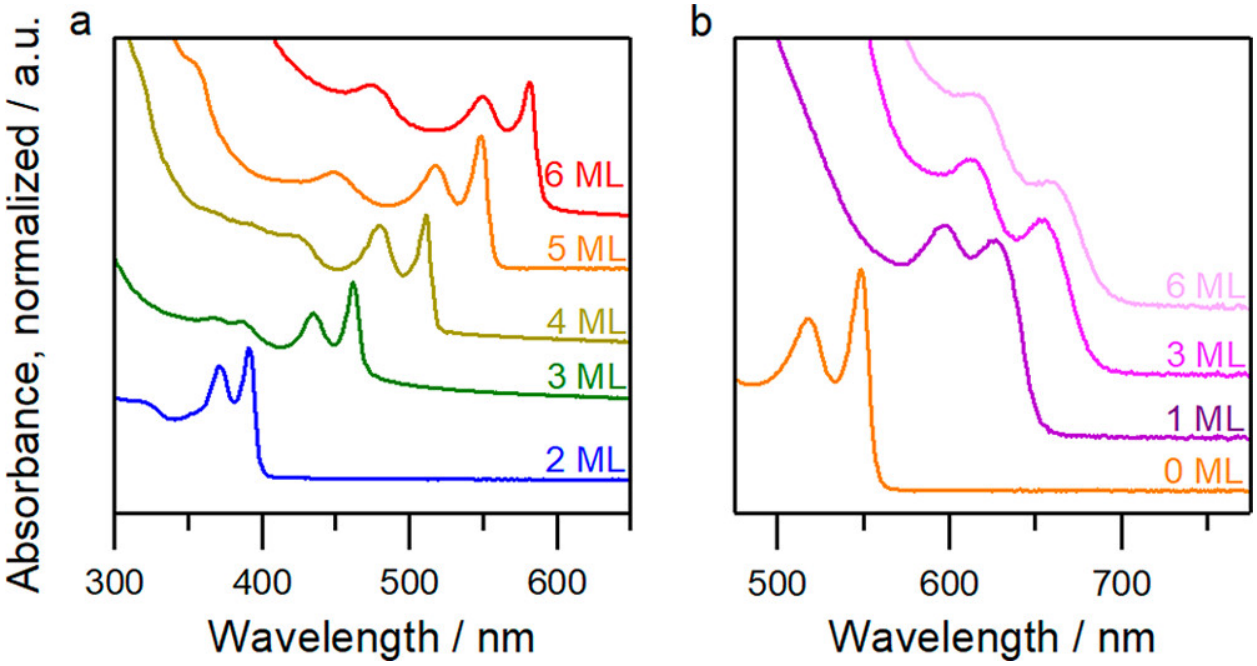

Figure 3. 1. Absorption spectra of CdSe nanoplatelet dispersions in hexanes.
(a) Indicated core-only monolayer thicknesses and (b) 5CdSe NPL cores with CdS shells of indicated layer thicknesses.

Colloidal NPLs, synthesized according to previously published methods,[84-88, 98] were dispersed in hexane for presented optical measurements. Steady-state absorption spectra of the 2.5, 3.5, 4.5, 5.5, and 6.5 ML CdSe NPLs (herein termed 2CdSe, 3CdSe, 4CdSe, 5CdSe, and 6CdSe, respectively) and CdSe/CdS core/shell NPLs with a 5CdSe core and 1, 3, or 6 ML CdS shell thickness (termed 5CdSe/ 1CdS, 5CdSe/3CdS, and 5CdSe/6CdS, respectively) are shown in Figure Figure 3. 1. As the core-only NPL thickness increases, the lowest energy absorption transition red-shifts (Figure 3. 1a), while the CdSe/CdS core/shell particles further red-shift from the core-only spectrum (for the same 5CdSe NPL core) with increasing shell-layer thickness as quantum confinement and dielectric confinement decrease (Figure 3. 1b).

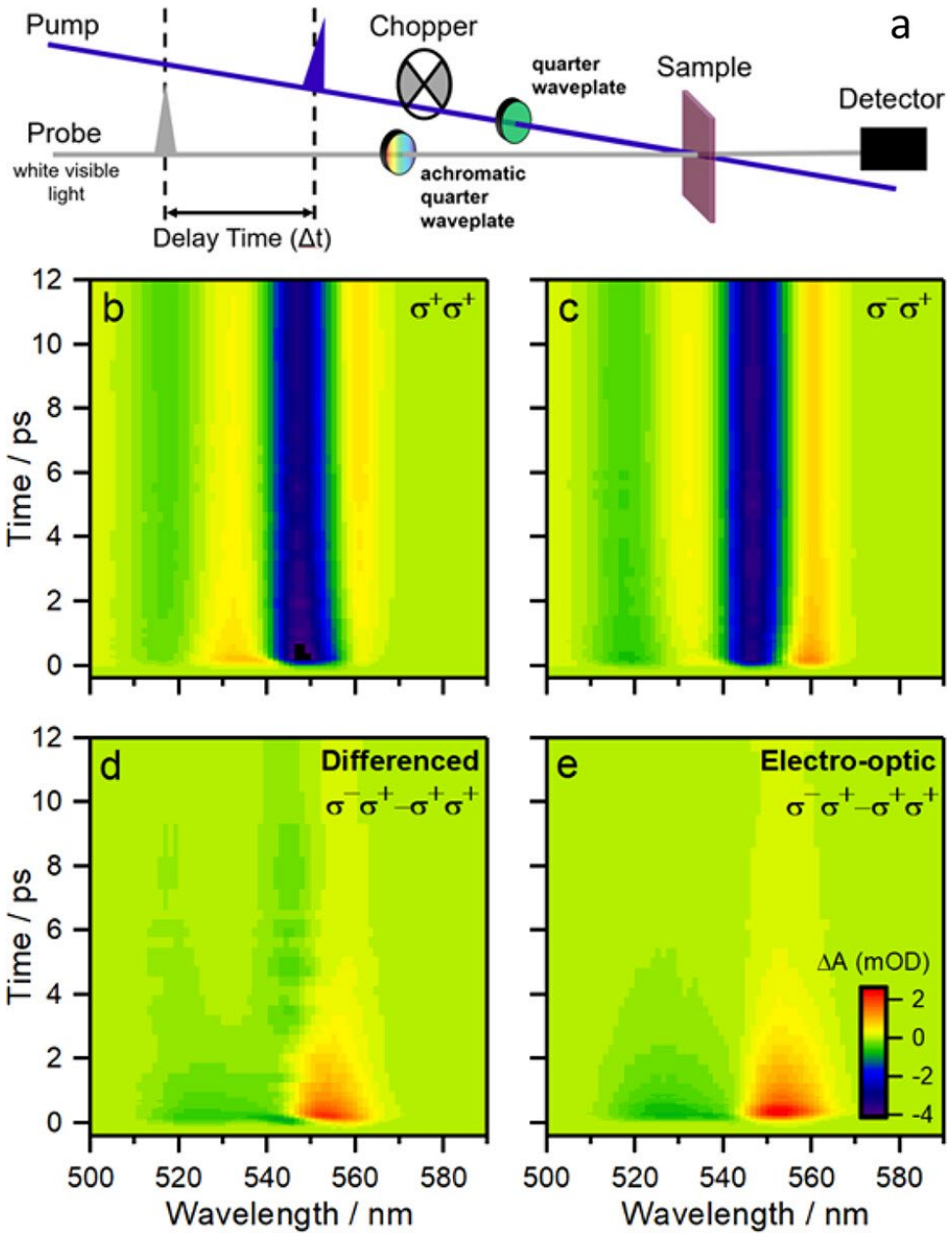

Figure 3. 2. Transient absorption spectral maps from copolarized, cross-polarized, and electro-optically modulated pump-probe conditions.
(a) Schematic of circularly polarized transient absorption experiments. (b, c) Transient absorption spectral maps for indicated pump and probe circular polarization conditions. (d) Differencing panel b from panel c highlights time-dependent response of the polarization-dependent spectral information. (e) Replacement of the mechanical chopper with an electro-optical modulator directly yielded differential responses of the sample to copolarized vs cross-polarized pump–probe conditions with increased signal-to-noise ratio.

We performed transient absorption experiments using a 35 fs, amplified titanium:sapphire laser with a 2 kHz repetition rate. Pump pulses produced with an optical parametric amplifier were circularly polarized using an achromatic zero-order waveplate, maintained at fluences corresponding to ~0.1 excitons per NPL on average, and made coincident on the sample together with mechanically time-delayed, circularly polarized white light probe pulses. In order to minimize exciton spin decay via hot carrier relaxation, samples were excited with pump wavelengths near respective absorption onset energies, typically about 10 nm blue of the band-edge transition and with less excess energy than the exciton binding energy (which spans 400 meV for thin cores down to 50 meV for thicker core/shells).[20, 99-101] Appreciably higher energy photon excitation reduced observed spin-polarized signal amplitudes. Figure 3. 2a shows the experimental configuration and representative transient absorption spectral maps versus pump−probe time-delay measured for the 5CdSe NPL sample. For cross-polarized data (Figure 3. 2b), we observe a photoinduced absorption (PIA) feature near 553 nm that is initially intense and decays within several picoseconds. In the copolarized TA spectral map (Figure 3. 2c), the PIA is notably weaker initially but becomes stronger within the first few picoseconds. This low-energy PIA feature is consistent with previous reporting and confers spin-selective excitation of the singly excited, spin-polarized exciton to a biexciton state and spin depolarization arising from flipping of either spin in the exciton.[20, 90, 93-102]

To isolate spin-polarized features in the TA maps, transient data were collected using a mechanically chopped pump pulse that was copolarized with the probe and then subtracted from separately measured cross-polarized data (Figure 3. 2d). Manual subtraction of the independently collected data sets does successfully highlight spectral and temporal features related to spin polarized transitions but is also subject to appreciable noise in quantitative analyses of the exciton

dynamics. To improve the signal-to-noise ratio, reduce data acquisition time, and implement a single multichannel detector for the probe pulses, we performed transient absorption measurements by replacing the typical mechanical chopper with an electro-optic inserted into the pump pulse train (see Figure 3. 2a) set to produce half-wave rotation at 1 kHz. Co- and cross-polarized pump−probe data were thus collected for immediately sequential pump pulses, not only eliminating the need to routinely collect probe-only spectra but also decreasing background noise introduced from fluctuations in the pump or probe intensity over experimental lab time. Using this approach, we were able to directly generate polarization differential transient spectral maps of the spin-dependent photophysical behaviors, as shown in Figure 3. 2e.

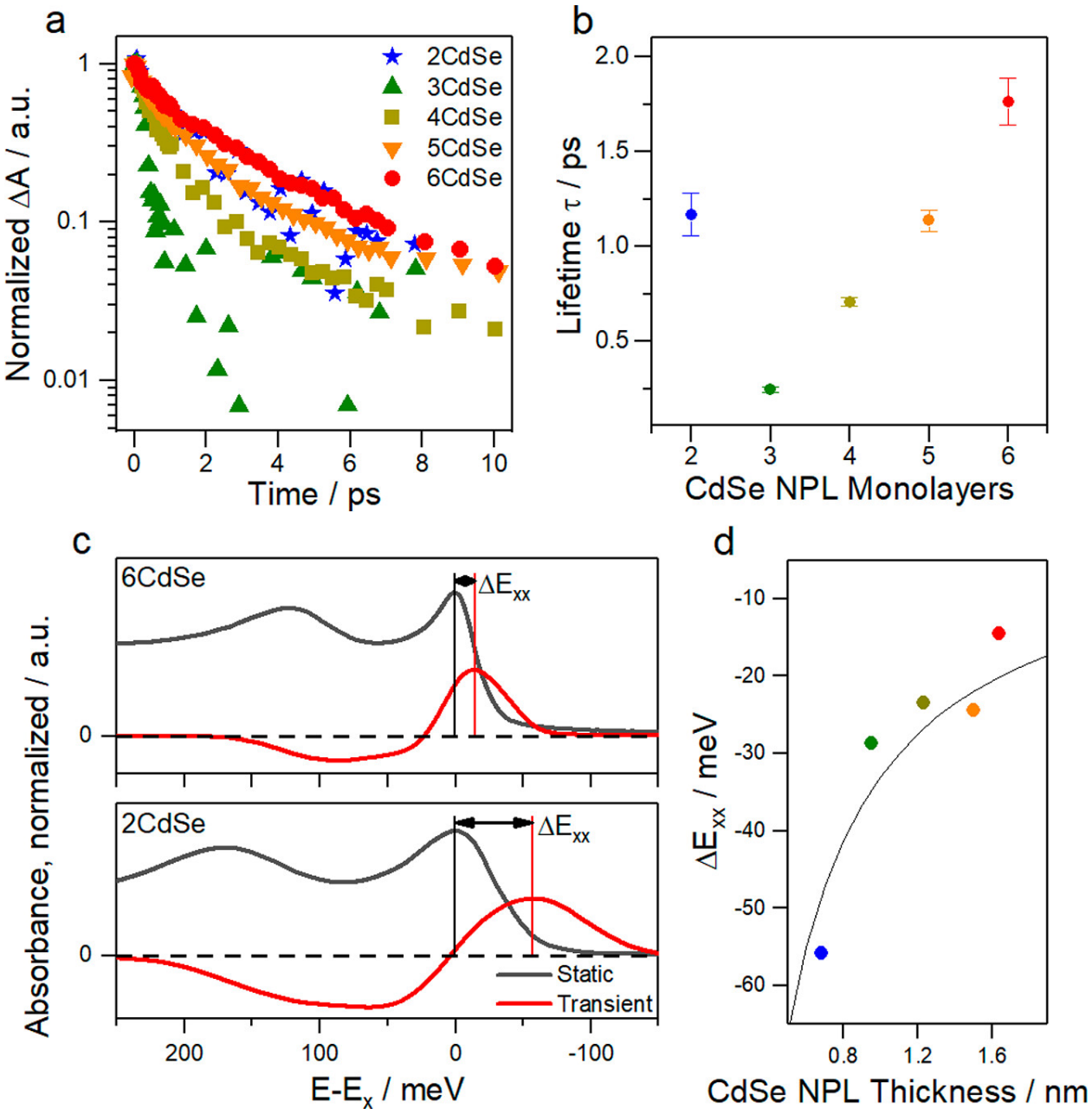

Figure 3. 3. Spin-dependent lifetimes and binding energies as a function of NPL thickness. (a) Spin polarization lifetime for indicated core-only NPL samples and (b) fitted decay time constants. (c) Biexciton binding energy, ΔE_{xx}, evaluated from the spectral shift of the static absorption maximum to that of the transient spin-polarized signal. (d) Biexciton binding energy evaluated for indicated core-only NPL thicknesses spanning 2CdSe to 6CdSe.

Figure 3. 3a shows the dynamic behavior of the spin-selective biexcitonic PIA across CdSe core-only samples as a function of increasing NPL thickness. These kinetic traces were then fit to single-exponential decays to evaluate spin coherence lifetimes (Table B. 1). Over the range of increasing NPL thickness from 3CdSe to 6CdSe, spin-polarized decay lifetime increases from just 0.24 ± 0.01 ps for 3CdSe up to 1.76 ± 0.12 ps for 6CdSe, as shown in Figure 3. 3b (data plotted to longer time delays appear as Figure B. 1). A conceivable origin of this trend may be the reduced prominence of surface atoms as NPL thickness increases which present surface spins that cause depolarization.

Notably, the 2CdSe does not fit the otherwise systematic trend, instead exhibiting similar dynamic behavior as 5CdSe, suggesting that other contributing factors in the generation of long-lived spin-polarized species impact the particularly thin 2CdSe NPLs. Thinner NPLs and especially 2CdSe experience appreciable strain in comparison to thicker NPLs that feature more internal bonding, which conceivably could disrupt the otherwise systematic trend.[103-105] At the same time, the >3 eV energy gap of 2CdSe may play a role if exciton wave functions begin to permeate the high potential barrier of the organic surface.[104] This thickness dependence for core-only samples conveys lifetimes that are short and comparable to those recently reported for 2D perovskite spin-polarized lifetimes versus inorganic layer thickness.[89] Xiang *et al.* reported fast, subpicosecond decay components as evidence of hole spin-flips in CdSe with longer-lived spin polarization arising from particles that lack rapid hole trapping[93] but relied on examining differences in dynamics for other exciton transitions that we did not observe. Notably, hole trapping has been implicated to occur on similar time scales as our observations[106] and could deleteriously affect excitonic spin polarization.

In addition to spin coherence decay lifetime, differential spin-polarized transient spectral maps show clear changes between the lower-energy PIA in comparison to the heavy hole static absorption feature as a function of thickness, with a shift from the static peak that relates biexciton binding energy and an increased line width possibly arising from relative spatial position of the second electron hole pair created by the probe[102] (see Figure 3. 3c). We find that attractive biexciton binding energy reaches ∼50 meV in the 2CdSe core-only NPLs and decreases to ∼15 meV in the 6CdSe core-only NPLs (Figure 3. 3d). Reduction of biexciton binding energy is expected as particle thickness increases and trends in the direction of bulk-like behavior.[107] Such biexciton binding energies for 4CdSe have been estimated at up to 45 meV in the literature,[90] based in part on observation of biexciton-derived gain and lasing red-shifts. However, we note that amplified spontaneous emission appears at energies prescribed by optical gain but is also influenced by optical loss from reabsorption. Measurements of binding energy reported in this report suffer less from the latter-described influence and relate a smaller value that is consistent with other experimental data for both 4CdSe[108, 109] and theory,[107] further highlighting the role of reabsorption from small Stokes shifts in gain and lasing efforts.

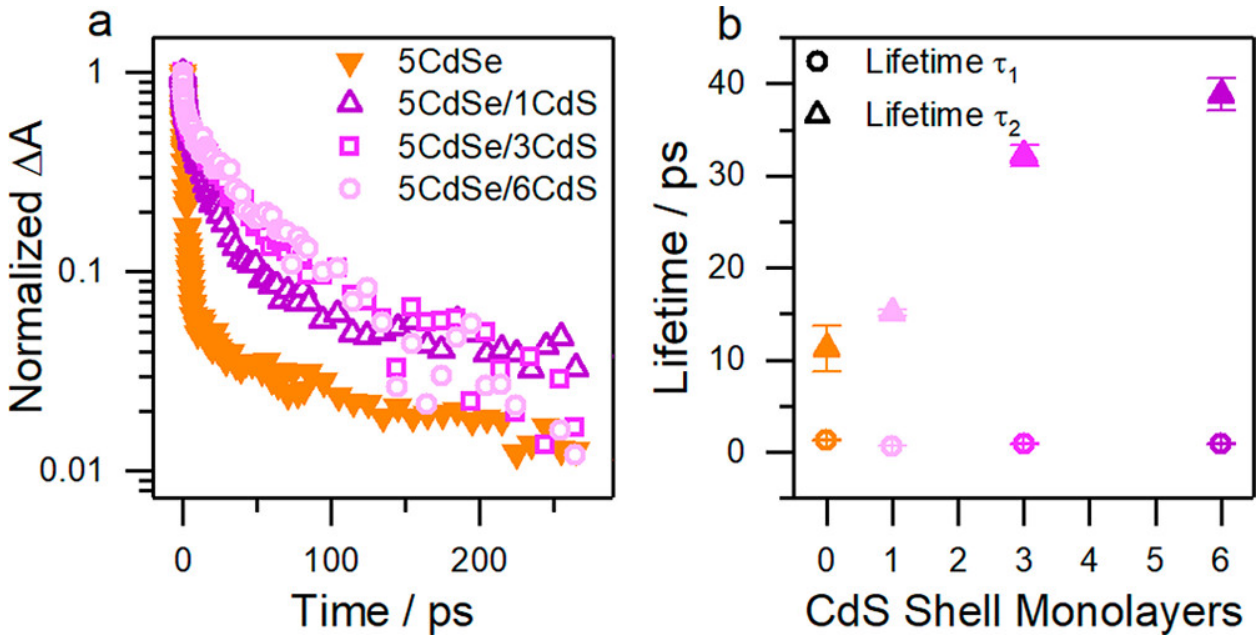

Figure 3. 4. Kinetics and fitted lifetimes in core/shell NPLs.
(a) Dynamics of CdSe/CdS core/shell NPL samples that were synthesized using the same 5CdSe core. Spin polarization lifetimes increase significantly for these core/shell structures. (b) Spin-polarized decay kinetics are well-described by biexponential fitting with lifetimes τ_1 and τ_2.

Figure 3. 4 shows the spin-polarized dynamic behavior of CdSe/CdS core/shell NPL samples that were synthesized using the same 5CdSe core. Spin polarization lifetimes increase significantly for these core/shell structures. Decay kinetics are well-described by biexponential fitting with lifetimes τ_1 and τ_2 (see Figure B. 2) for each sample exhibiting a rapid, ~1 ps process and a longer-lived, up to ~49 ps lifetime (see also Table B. 2). This longer decay component indicates a significant extension of spin-polarized exciton lifetime relative to the core-only samples. The τ_2 lifetime increases sublinearly with CdS shell thickness, which suggests diminishing influence on the preservation of spin polarization with both increased total volume of the nanostructure and increased average distance to the organic interface. Quantum confinement, it should be noted, also changes sublinearly with shell layer thickness. Increases of the exciton

spin coherence lifetime clearly arise from features of the core/shell morphology, but a challenge to mechanistic interpretation is that the core/shell system differs in multiple ways from the core-only particles. The core/shell samples experience reduced electron−hole wave function overlap for this combination of materials and reduced quantum and dielectric confinement in addition to altered CdSe interface chemistry. The quasi-type-II energy level alignment of the CdSe/CdS conduction bands permits electron delocalization into the CdS shell layer whereas holes nominally remain within the CdSe core.[96] Such delocalization could serve to reduce exchange interaction of the electron with the hole that can facilitate spin relaxation.[110] At the same time, isolated spins of dangling bonds and charges at the inorganic−organic interface may offer fast, efficient spin relaxation,[92, 111, 112] but the nearly matched lattices at the inorganic−inorganic interface can largely reduce the importance of such relaxation processes.

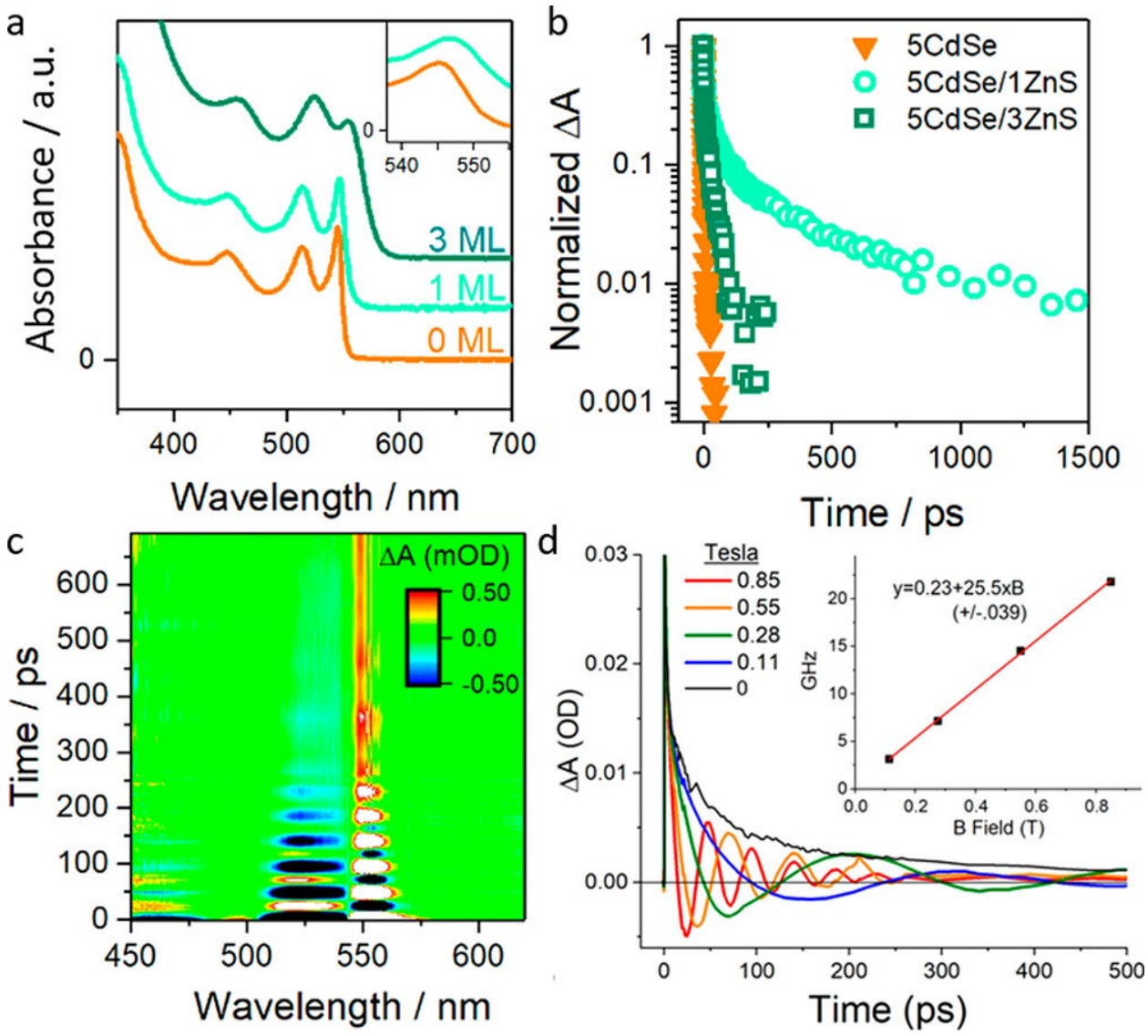

Figure 3. 5. Spin-decay characteristics in CdSe/Zns core/shell NPLs.
(a) Absorption spectra of core/shell NPLs with a 5CdSe core and either 1 or 3 ZnS shell layers. (b) Pump-polarization-modulated transient response of the three samples in panel a show an appreciable increase in spin-polarized lifetime with even 1 layer of ZnS shell growth. (c) Transient Faraday rotation of a 5CdSe/1ZnS nanoplatelet sample at room temperature shows oscillatory behavior with one discernible frequency. (d) For the 5CdSe/1ZnS sample, measurement at several different indicated magnetic field strengths (here plotted at 554 nm probe wavelength) shows a linear dependence of oscillation frequency (inset), a *g* factor of 1.83, and small y-axis intercept (230 MHz).

To evaluate influences on CdSe/CdS core/shell spin lifetimes, we also prepared 5CdSe/ZnS core/shell NPLs with 1 or 3 ZnS monolayers. These structures, for which shells were carefully grown via colloidal atomic layer deposition using a fixed 5CdSe core,[85, 98] lack appreciable delocalization of either charge-carrier into this wider gap shell as noted by the absorption spectra shown in Figure 3. 5a. ZnS shell growth does appreciably alter the surface bonding in comparison to organic ligand surface termination. Interestingly, the 5CdSe/1ZnS core/shell sample presented markedly slower spin depolarization relative to the core-only sample as shown in Figure 3. 5b, with a significant amplitude ~100 ps lifetime as well as additional still longer-lived low-amplitude components (see Figure B. 3 for biexponential fits and Table B. 3 for fit parameters). Upon continuing growth to a 3ZnS monolayer shell, lifetime decreases to ~21 ps perhaps influenced as strain builds up with the thicker, small-lattice-spacing shell.

Overall, the significant lifetime increase suggests that removal of the proximal organic surface termination or passivation of dangling surface bonds for the core/shell structure serves to increase spin lifetimes in both the CdSe/CdS and CdSe/ZnS systems, consistent with theoretical investigations of Rodina *et al.*[111, 112] Additionally, this finding suggests that the hole spin relaxation mechanism is not centrally important, as this charge remains contained within the CdSe core for the latter core/shell.

Finally, we performed transient Faraday rotation measurements in different magnetic fields[113] for the 5CdSe/1ZnS sample. Magnetic field causes the spin polarization to oscillate with the Larmor precession frequency associated with $E = g\mu_B B$. In these experiments field-induced oscillations occur, and we find the oscillation frequency scales linearly with magnetic field strength with y-intercept near zero (~230 MHz). By fitting the period of oscillation versus field,

we obtain an excitonic *g* factor of $g = 1.83$ that relates contributions of the electron and hole. This value is similar to other reports of exciton g factor as studied using pump−orientation−probe measurements, such as in work by Feng *et al*.,[114] and further confirms that the long lifetime observed indeed conveys spin coherence.

The spin depolarization of these states can occur through various mechanisms, including hot carrier relaxation and inelastic collisions with the nanoplatelet surface, that result in rapid spin-polarization decay. There are several common spin-depolarization mechanisms in semiconductors.[91, 92, 96] In the Elliot−Yafet (EY) mechanism, spin depolarization occurs through momentum scattering while the Bir−Aronov−Pikus (BAP) mechanism becomes operative in materials where hole concentration is high and exchange scattering with electrons is possible. The relevance of these mechanisms in bulk materials is often dictated by the availability of phonon coupling (in the case of EY) and exchange scattering (in the case of BAP) pathways as affected by temperature, carrier mobilities, and morphology. However, quantum confinement of nanoparticles can result in local structure-induced magnetic fields, such as at the surface,[92, 111, 112] which boosts the dominance of Dyakonov−Perel (DP) pathways that are enabled in structures without inversion symmetry and supported by extended electronic states. Synthetic manipulation of the particle morphology, such as increasing the nanoplatelet thickness or replacing an organic ligand with a more perfectly matched shell layer, alters characteristics of the particle surface, in some cases reducing electron−hole overlap for CdSe/CdS, but in the case of CdSe/ZnS chiefly moves spins of organic ligand termination further from the spin-polarized exciton and reduces the rate of dominant spin-depolarization pathways. Increasing ZnS shell thickness likely increases strain and may

introduce cracks in the shell, altering the energy landscape, though this requires more investigation.

With regard to observation of biexponential decays of spin-polarized lifetime, we expect that such observations point to different electronic scenarios for subpopulations within the ensemble with an origin that remains to be investigated. Notably, spin-polarization data for the 5CdSe core-only sample shown in Figure 3. 4a does not match that of a different 5CdSe sample shown in Figure 3. 5b. The former shows a few percent amplitude of a longer-lived spin polarization that is absent in the latter sample. The observation for the former offers a prospect of long-lived spin polarization in core-only samples if the features of this subpopulation might be understood and controlled.

3.4 Conclusion

Spin polarization of excitons created with circularly polarized laser pulses in core-only CdSe NPLs decay rapidly, occurring on picosecond time scales. Variation in sample morphology, such as particle thickness and surface passivation, are shown to impact and increase spin-depolarization lifetimes, with an increase from $\tau = 0.24$ ps in 3CdSe NPLs to $\tau = 1.76$ ps in 6CdSe NPLs. Growth of CdS shells yielded significant increases in spin-depolarization times, with an order of magnitude effect for thin-shelled samples of 5CdSe/1CdS NPLs ($\tau_2 = 24$ ps) up to $\tau_2 = 48.6$ ps for 5CdSe/6CdS NPLs. Additional measurements conducted on 5CdSe/ZnS samples, which do not alter electron−hole overlap, would suggest a key role that surface passivation plays in maintaining excitonic spin coherence. In particular, 5CdSe/1ZnS core/shell samples exhibited a 100 ps lifetime, which is nearly two orders of magnitude longer than those observed in core-only samples. Studying these effects provides an important step toward understanding how to generate

and maintain long-lived spin-polarized excitonic states in 2D semiconductors. Understanding specific spin-depolarization lifetimes and mechanisms will be valuable for the implementation of these states and materials in future technologies.

Chapter 4. Transient X-ray Diffraction Reveals Non-Equilibrium Phase Transition in Thin Films of CH_3PbI_3 Perovskite

Reprinted with permission from "Shobhana Panuganti, Shelby A. Cuthriell, Ariel A. Leonard, Michael A. Quintero, Craig C. Laing, Burak Guzelturk, Xiaoyi Zhang, Lin X. Chen, Mercouri G. Kanatzidis, and Richard D. Schaller. *ACS Energy Lett.* **2023** *8* (1)*,* 691-698."

4.1 Abstract

Advantageous optoelectronic properties of methylammonium lead triiodide ($MAPbI_3$) likely arise from coupling between photogenerated charge-carriers and the soft, deformable lattice. We investigate structural dynamics of $MAPbI_3$ films using time-resolved X-ray diffraction versus pump–probe time delay and pump intensity. During the first nanosecond, the lattice anisotropically distorts from tetragonal to cubic at excitation intensities that are insufficient to thermally induce the first-order thermodynamic phase transition at 330 K. The high-symmetry structure then relaxes back to the starting phase with 11 and 236 ns time constants via a different transition pathway than observed either in the first nanosecond or in previous reports for $MAPbI_3$. Early time dynamics are consistent with polaron formation and lattice strain stabilization while the slower recovery dynamics outlive radiative recombination and relate metastability. Fluence-independence of these lattice deformations in the low-power regime conveys relevance to optoelectronics including photovoltaics and highlights sustained involvement of nonequilibrium, photoinduced lattice reorganization in $MAPbI_3$ under functional conditions.

4.2 Introduction

Significant research efforts focus on methylammonium lead iodide and related hybrid organic–inorganic perovskites because they are inexpensive, solution-processable semiconductors with desirable properties for optoelectronic applications.[115-117] Recent studies have suggested that many of these unexpected and attractive properties likely arise from dynamic structural behavior not observed in more rigid crystalline substances[118, 119] allowing for complex lattice-carrier coupling, such as the rapid formation of polarons.[120-123] While there are reports that the operative conditions of optoelectronic applications do affect the structure and optical properties of this material, transient spectroscopic studies are unable to directly probe underlying lattice behavior, which is typically assumed not to change appreciably.[119, 124, 125] When lattice behavior deviates significantly from equilibrium, such as we show here with $MAPbI_3$, electronic phenomena respond to the altered crystal symmetry, thus spectroscopic findings can misinterpret observables that actually derive from lattice evolution. In the same way that crystal phase transitions can alter bandgap and carrier effective mass, local changes in crystal symmetry near photon absorption events can yield not only carrier trapping, but also screening and protection of charges from rapid recombination.[122, 126] Direct investigations of lattice dynamics with high Q resolution are required to discern conditions that lead to lattice changes and relevant time scales of distortion formation and relaxation. Photoinduced heating can also occur due to intraband relaxation of hot carriers and Auger processes, such as from above-gap excitation,[127-129] introducing both thermal and electronic effects to consider in the overall lattice response.[125, 130, 131]

Prior structural studies of $MAPbI_3$ have determined that this material undergoes a first-order thermodynamic phase transition from the room-temperature tetragonal *I*4*/mcm* space group

into the high-temperature cubic $Pm\bar{3}m$ phase.[125, 132] Single crystal diffraction has shown that the two structures are closely related with additional distortions present in the tetragonal structure that lower its symmetry.[124, 133] In particular, the Pb–I–Pb bond angles are 180.0(0)° and 179.1(4)° whereas the tetragonal lattice distorts away from this "ideal" bonding geometry (see Figure 4. 1a).[134] One recent study utilizing ultrafast electron diffraction observed large increases in disordered motion of organic cation and halide site occupancy, providing further evidence of nonequilibrium structural changes.[135] Still, currently available transient electron diffraction techniques lack sufficient resolution to discern individual Bragg reflections, which could offer aspects of its structural lability.[136]

In this work, we perform time-resolved X-ray diffraction measurements of $MAPbI_3$ thin films that reveal significant, nonequilibrium distortions following photoexcitation with fluence-independence that suggests relevance to solar energy conversion. Unlike other techniques, powder X-ray diffraction of thin films using pulsed (79 ps), synchrotron X-rays affords high-resolution diffraction for time-resolved structural insights and individually resolved Bragg reflections that can be monitored with respect to pump–probe delay time. By using pulsed excitation, we are able to examine the fundamental carrier and lattice dynamics that underlie material performance with aims to comprehend and eventually guide optoelectronic materials design. We observe fluence-independent, structural transformations of $MAPbI_3$ that indicate gradual, anisotropic distortions of the lattice from tetragonal to a distinct cubic phase followed by a slow recovery back into the tetragonal phase. Notably, while our observations are consistent with reported photoinduced phase transitions in metal halide perovskites,[137] our results also suggest that the material recovery from the high-symmetry structure back to the unexcited, tetragonal phase proceeds through structural

distortions unlike those observed during the rise process in the first nanosecond. These findings establish a more precise understanding of the dynamic excited-state response in $MAPbI_3$, offer insight into the atypical, nonequilibrium behaviors that enable its remarkable performance, and provide clear evidence that the remarkable *in situ* material properties arise from the unique structure of the operative material, which is not the same as the equilibrium structure.

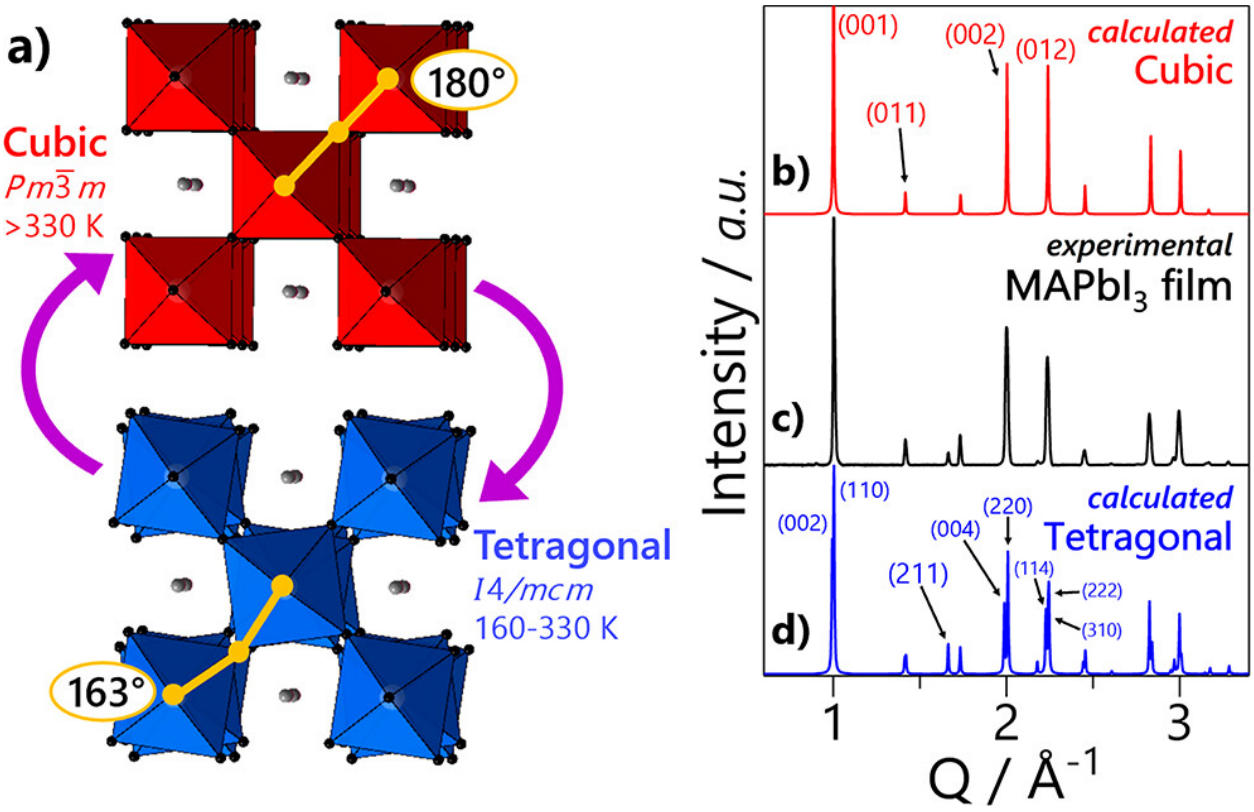

Figure 4. 1. Steady-state structures of $MAPbI_3$.
a) Visualization of the tetragonal (blue) and cubic (red) phases of $MAPbI_3$. At room temperature and pressure, the material exhibits a tetragonal structure with Pb–I–Pb bond angles that deviate from the ideal octahedron geometry. The gradual extension of these strained bond angles to 180° transforms the material into the cubic perovskite phase. (b) Calculated diffraction pattern of the cubic phase (red) of $MAPbI_3$, (c) experimental diffraction pattern of the sample film (black), and (d) calculated diffraction pattern of the tetragonal phase (blue) of $MAPbI_3$. Miller indices are indicated for peaks of interest.

4.3 Results and Discussion

Measurements were conducted at Beamline 11-ID-D of the Advanced Photon Source at Argonne National Laboratory according to the setup shown in Figure C. 1. Thin films of $MAPbI_3$ were fabricated using modified, published methods.[46] Briefly, $MAPbI_3$ crystals were synthesized and dissolved in dimethylformamide to produce a precursor solution for spin-coating onto sapphire substrates. Substrates were then annealed to produce polycrystalline thin films and coated with poly(methyl methacrylate). Films were photoexcited using 400 nm (3.1 eV), 1.2 ps duration pulses at 10 kHz with controlled fluences for a pump spot area of 1200 × 6900 μm of above-gap excitation. Notably, the above-gap excitation homogeneously excites within the plane of the film and is not selective for particular film regions. Films were rapidly spun in order to reduce degradation, present spatially averaged responses, and excite regions of the sample that are under ambient conditions. X-ray diffraction probing was performed using 11.7 keV X-ray pulses that were 79 ps in duration, and powder diffraction patterns for given pump–probe time delays were integrated on a Pilatus 2M detector. To lessen photodegradation over the course of the experiments, we prepared sample films with thicknesses >0.5 μm, therefore larger than the penetration depth of the pump but within the X-ray probing depth. By subtracting the steady-state diffraction pattern of the sample from each transient photoexcited pattern, we isolated the behavior of the photoexcited population from the unexcited depth of the film. Throughout this work, we refer to these postprocessed, differenced patterns as transient patterns for ease of analysis. Additional details are available in Appendix C.

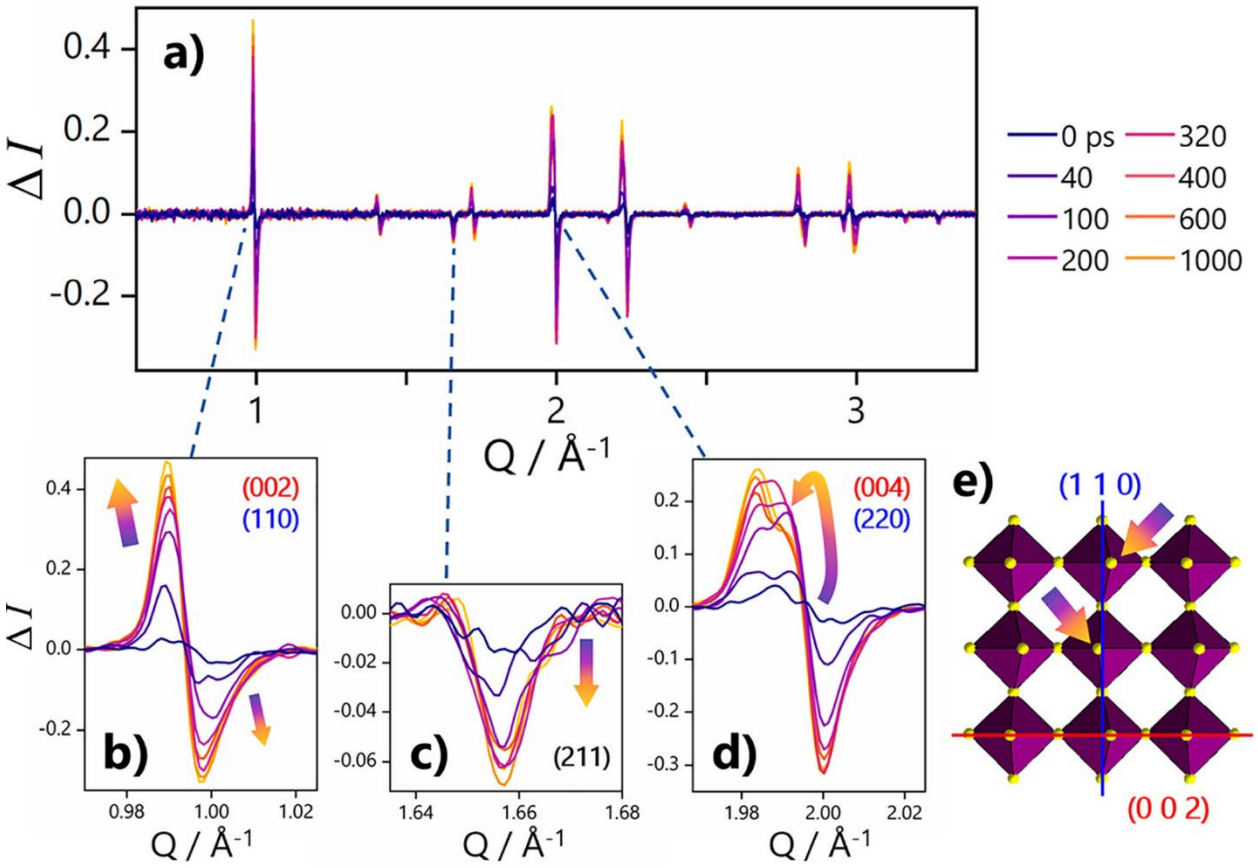

Figure 4. 2. Transient diffraction patterns for $MAPbI_3$.
(a) Transient diffraction patterns showing the change in diffraction intensity (ΔI) from 0 to 1000 ps (legend at right) at a representative fluence of 77 μJ • cm^{-2}. Peaks of interest are indicated at Q = 0.99 $Å^{-1}$, Q = 1.66 $Å^{-1}$, and Q = 1.99 $Å^{-1}$. (b) ΔI centered around Q = 0.99 $Å^{-1}$ exhibits negative and positive signal at all time delays, indicating lattice expansion. However, the signal shape is asymmetric with the positive signal intensity increasing more quickly than the negative signal over pump–probe delay time. (c) ΔI at Q = 1.66 $Å^{-1}$, corresponding to the (211) reflection of the tetragonal phase, decays during the first nanosecond without any evidence of expansion. This reflection is present in the tetragonal phase and absent in the cubic phase. (d) ΔI centered around Q = 1.99 $Å^{-1}$ exhibits lattice expansion. In the positive signal, two distinct peaks can be seen increasing in intensity at different rates over time with the area under the positive signal appearing larger than that of the negative signal. (e) The (110) and related (*nn*0) family of reflections correspond to the axis along which Pb–I–Pb bond angles are distorted in the tetragonal structure while the (004) and related (00*2n*) reflections instead show ideal bonding geometry where the Pb–I–Pb bonds are at or close to 180°.

Figure 4. 1 shows steady-state diffraction of the sample (Figure 4. 1c, black), as well as diffraction patterns calculated from single-crystal X-ray diffraction studies of the high-temperature (>330 K) cubic phase (Figure 4. 1b, red) and room temperature tetragonal phase (Figure 4. 1d, blue) of $MAPbI_3$.[134] The calculated patterns of the tetragonal and cubic phases of $MAPbI_3$ share many peaks at nearly identical *d*-spacings in the experimental film pattern, making it difficult to discern some of the closely spaced peaks that are present in the tetragonal phase as compared to the cubic phase. However, the lower symmetry of the tetragonal phase results in several additional peaks that are absent in the cubic phase and allow us to distinguish the two phases; the (211) reflection of the tetragonal phase at $Q = 1.66$ Å^{-1} can be clearly seen in the experimental diffraction pattern (Figure 4. 1c) and confirms that the unexcited film is in the tetragonal phase.

Transient diffraction patterns collected over the first nanosecond following photoexcitation at a fluence of 77 μJ • cm^{-2} are shown in Figure 4. 2. In particular, we observe a reduction of diffraction intensity from the (211) tetragonal reflection at $Q = 1.66$ Å^{-1} over time (Figure 4. 2c). The decrease in diffraction intensity of this reflection suggests a photoexcited transition of the structure to a higher symmetry space group where the reflection has become systematically absent. Though reflections present only in the tetragonal phase are still observed in the undifferenced transient patterns after photoexcitation, the differenced patterns serve to isolate photoexcited behavior and do not contain information about the unexcited portion of the films. Thus, the absence of positive features at any new positions over time coincident with the isolated reduction in diffraction intensity along tetragonal-only reflections is consistent with the observation of a transition to higher symmetry. Other peaks exhibit both negative and positive features and reach their maximum signal intensity by one nanosecond, suggesting a gradual expansion of the structure

along all axes of the lattice (Figure 4. 2a). Upon lattice expansion, spacing between planes increases and Bragg reflections shift to lower Q values in the diffraction patterns. In transient patterns, these shifts in peak position appear as derivative line shapes with approximately symmetric positive and negative signals at respectively lower and higher Q values. We also note that in contrast to dynamics reported for studies of inorganic colloidal nanoparticle systems, in which structural recovery begins within the instrument response time, the slow rise dynamics of this material that also persist long after the instantaneous formation of charge-carriers are particularly remarkable.[137-140]

Many peaks in transient patterns also exhibit asymmetric positive and negative signal line shapes. As seen at $Q = 0.99$ Å^{-1} (Figure 4. 2b), the positive and negative signal intensities are nearly equivalent from 0 to 60 ps; the positive signal subsequently outgrows the negative signal (Figure C. 1). This asymmetry likely arises from higher relative scattering intensities of reflections in the cubic phase as well as tetragonal reflections disappearing in concert with the appearance of a cubic reflection. Notably, certain regions of transient diffraction patterns exhibit multiple negative and positive features. In Figure 4. 2d, two distinct features are apparent in the positive signal near $Q = 1.99$ Å^{-1}, indexed to the (004) and (220) Bragg reflections of the tetragonal structure. Initially, the signal intensity corresponding to the (220) reflection on the right increases more quickly than the (004) reflection. However, the (220) begins decaying after 400 ps even as the (004) signal continues to increase until 1 ns. Since these individual reflections are nearly indiscernible in the steady-state pattern (Figure 4. 1c), the visible peak separation in the transient patterns suggests different magnitudes of expansion along each direction. The (220) reflection corresponds to the lattice plane along which Pb–I–Pb bond angles are distorted away from 180° in

the tetragonal structure while the (004) reflection instead results from the lattice plane that exhibits cubic bonding geometry (Figure 4. 2e), indicating that anisotropic expansion precedes the extension of the distorted bond angles within the first nanosecond following excitation.

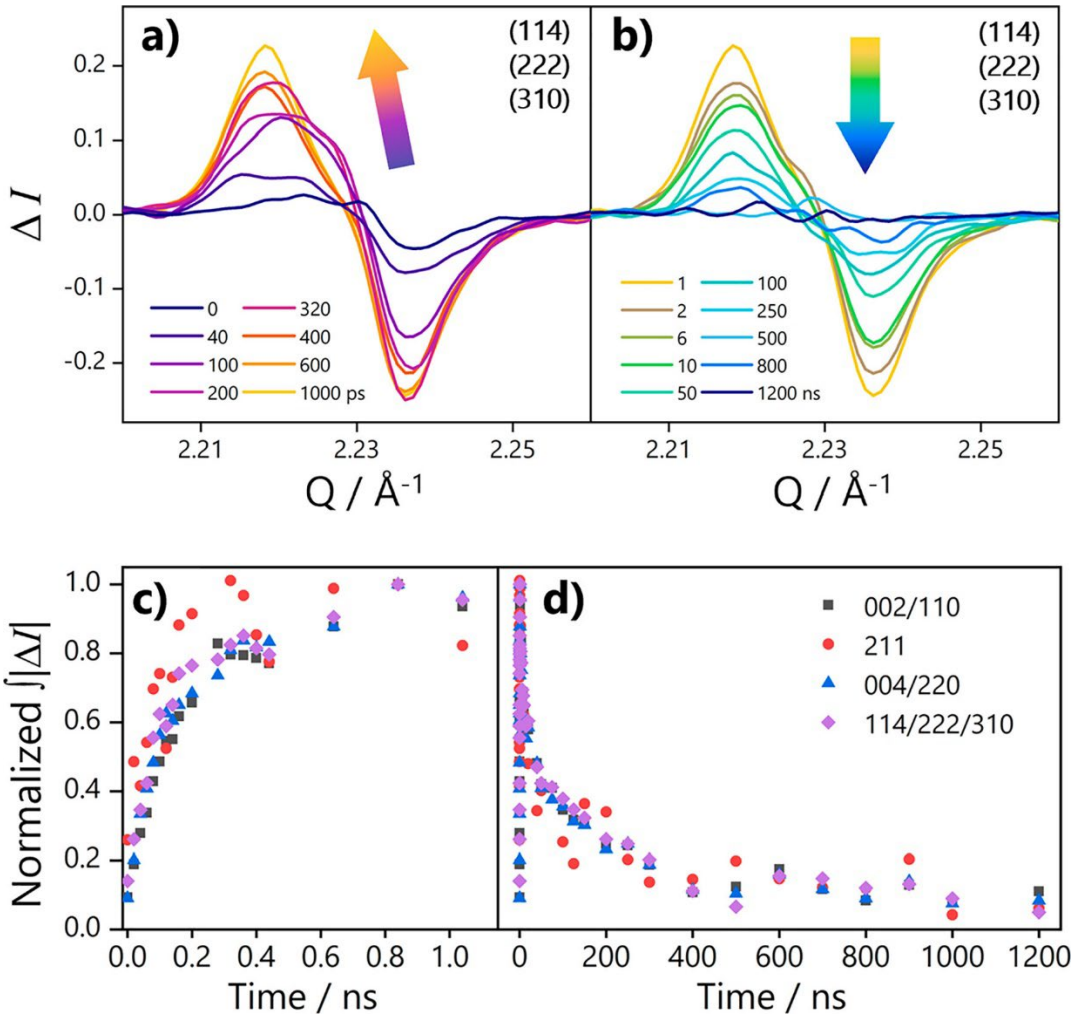

Figure 4. 3. Rise and recovery transient patterns and kinetics.
At top, transient patterns at 77 μJ • cm^{-2} showing the change in diffraction intensity (ΔI) centered around Q = 2.23 Å^{-1} from (a) 0 to 1 ns and (b) 0 to 1200 ns following photoexcitation. At bottom, normalized integrated absolute values of peak areas ($\int|\Delta I|$) as a function of pump–probe delay time for selected reflections from (c) 0 to 1 ns and (d) 0 to 1200 ns following photoexcitation. Exponential fitting of normalized $\int|\Delta I|$ with respect to time revealed fluence-averaged "rise" lifetimes of τ_{211} = 144 ± 20 ps for the initial decrease of (211) reflection (red, circle) as well as τ_1 = 58 ± 10 ps and τ_2 = 296 ± 26 ps for the remaining peaks. Following 1 ns, the structure begins its "recovery" with fluence-averaged fitted lifetimes of τ_3 = 11.1 ± 4.1 ns and τ_4 = 236 ± 49 ns.

Similar changes in diffraction intensity are observed in other reflections that overlap in the steady-state pattern including those at $Q = 2.23$ Å^{-1} which are discussed in further detail below (Figure 4. 3a,b). This complex evolution has not been reported in the mechanism of the first-order thermodynamic transition. Though the properties of the first-order phase transition at 330 K in $MAPbI_3$ have been well-characterized, previous empirical studies have not examined transient diffraction patterns of $MAPbI_3$, such as those reported here, due to the ultrafast experimental conditions required. As a nonequilibrium phenomenon, these observations are consistent with reports of preferential coupling and polaron formation along the *c*-axis in both computational and experimental studies of metal halide perovskites.[120, 121, 141]

Additionally, the positive signal retains a shoulder feature around $Q = 1.99$ Å^{-1} where the (220) reflection appears. We considered that the lingering (220) feature may be due to many distinct lattice domains throughout the film that exhibit different degrees of structural distortion over time.[142] In addition to the tetragonal and cubic structures, local distortions with sufficient coherence would result in distinct diffraction features as pump–probe delay time increases since carriers and heat likely diffuse into domains below the photoexcited population subsequent to the initial photoexcitation pulse.[143] As the local structure expands and distorts to accommodate the inflow of carriers and thermal energy, these populations would begin to appear as an additional feature, such as the shoulder noted above, in the transient pattern.

After 1 ns, pump-induced changes in X-ray diffraction intensity begin to decrease across all reflections, indicating structural relaxation and contraction as well as recovery toward the unperturbed lattice phase. Interestingly, in Figure 4. 3a we observe multiple features ─ indexed to the (114), (222), and (310) Bragg reflections of the tetragonal phase ─ evolving at different rates,

especially noting the dominant shoulder at high Q values in the positive lobe at early times. In contrast, the line shape at all times after the material begins to relax exhibits wholly new features (Figure 4. 3b). The three indexed reflections appear less distinguishable, and the dominant shoulder at Q = 2.225 Å^{-1} does not reappear with the same diffraction intensity. The transition mechanism of the material from tetragonal to cubic appears to differ from the recovery mechanism back to the initial tetragonal phase. In order to elucidate the origins of this mechanistic hysteresis and other observed structural evolutions, we examine the dynamics of these phenomena and identify correlated behaviors as potential sources.

Dynamics were further investigated by calculating the absolute value of the integrated area of the transient pattern at each pump–probe delay. The rise and recovery dynamics for selected peaks at a representative fluence of 77 μJ • cm^{-2} are shown in Figure 4. 3c. The (211) tetragonal reflection at Q = 1.66 Å^{-1} displayed single exponential behavior with an average lifetime of τ_{211} = 144 ± 20 ps across all measured fluences with sufficient intensity for fitting (Figure C. 2). However, biexponential fitting of the rise in the diffraction signal across the other selected peaks and fluences (Figure 4. 3c) indicated two processes: an initial, rapid response over tens of picoseconds (τ_1 = 58 ± 10 ps) followed by a longer rise lifetime over hundreds of picoseconds (τ_2 = 296 ± 26 ps). The fitted values for τ_1 fall within the pulsewidth of the X-ray probe and may correlate to reports of acoustic phonon lifetimes[133] and thermal bottlenecking[144] while the longer lifetimes τ_2 correlate with both polaron stabilization lifetimes[118] (~300 ps) and thermalization lifetimes[145, 146] (~250 ps) found between the organic and inorganic lattice in transient, optical studies. Biexponential fitting of the recovery dynamics averaged across all measured fluences (Figure 4. 3d) showed a decay of τ_3 = 11.1 ± 4.1 ns followed by a slower relaxation of τ_4 = 236 ±

49 ns for all analyzed peaks, the latter of which outlives several reports of radiative recombination lifetimes in similar $MAPbI_3$ films and points to the metastability and hindered recovery of the excited state structure.[147, 148] The faster recovery time scale τ_3 correlates with carrier relaxation and recombination time scales,[116, 127] while the slower recovery τ_4 process shows the transient signals becoming weaker, suggesting lattice contraction and cooling.

The anisotropic rates of change along each direction of the lattice are consistent with reports that the formation and stabilization of polarons occurs preferentially along the *c*-axis—elongating the lattice in the (00*l*) direction (see Figure 4. 2e)—followed by straightening of the distorted Pb–I–Pb bonds into the cubic phase.[121] Prior reports have found that photoexcited electrons couple preferentially with phonons corresponding to the stretching and bending of Pb–I–Pb bonds; this electron–phonon coupling enables polaron formation to occur along the *c*-axis where the electrons couple with Pb–I bond vibrations. Guzelturk *et al*. conducted transient single crystal X-ray diffraction studies in the related hybrid perovskite methylammonium lead bromide and observed similar anisotropic strain associated with electronic changes, estimating the strain energies and finding them in agreement with polaron binding energies and estimated polaron radius.[123, 149] However, the dissipation of polarons with lifetimes of hundreds of picoseconds in related metal halide materials,[120] significantly shorter than τ_4 in this work, may restrict relaxation pathways and thus contribute to the prolonged metastability of the excited structure as well as observed hysteresis in the transition mechanism. It is also likely that the rapid absorption of photons and subsequent nonequilibrium behavior induces strain in the material that impacts the onset of the phase transition.[150] As such, there would be lattice distortions that accommodate the interface between the photoexcited population against the unexcited population of the sample.[151]

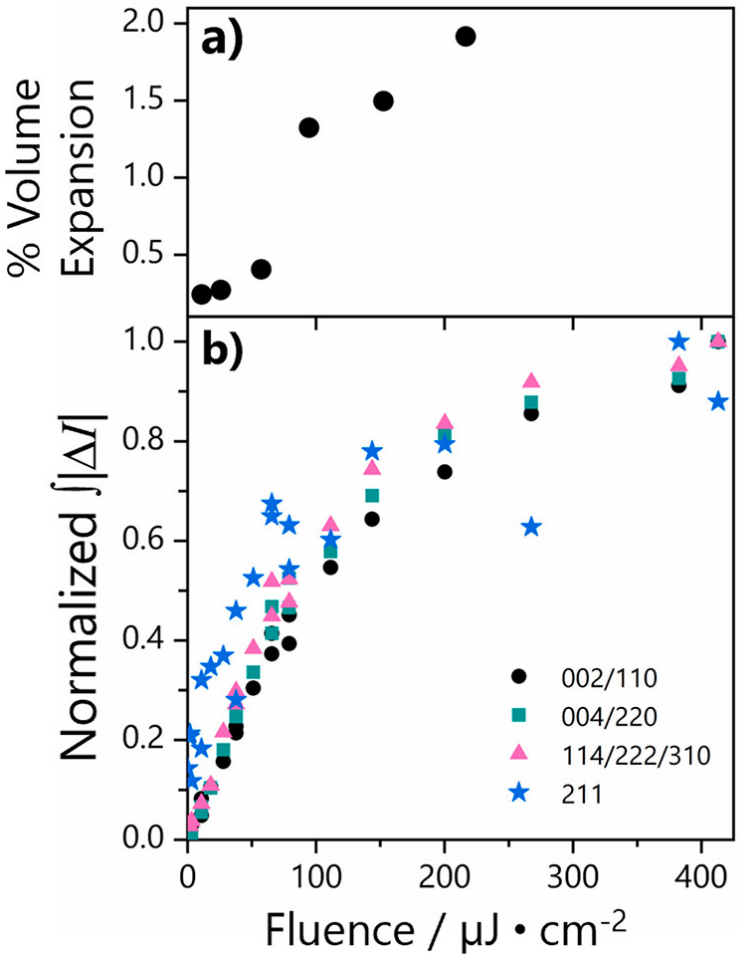

Figure 4. 4. Fluence-dependent behavior and volume expansion.
(a) Percent volume expansion of the photoexcited structure at 1 ns compared to the equilibrium cubic structure at 330 K. (b) Normalized integrated absolute values of peak areas $\int|\Delta I|$ as a function of pump fluence for selected reflections.

Ranges of temperature elevation of the photoexcited material were calculated as a function of pump fluence (Table C. 1).[122, 151] Maximum temperature calculations assumed all pump energy became available thermal energy, while minimum temperatures were calculated assuming only photon energy in excess of the band gap is dissipated thermally. Additional details are available in Appendix C. We note that these calculations do not consider thermal diffusion into the rest of the film over time and thus represent the effective temperature of only the photoexcited material at

early time.[117, 143, 152, 153] Calculated effective temperatures fall short of the reported temperature at which a phase transition occurs (330 K) for all but the highest fluence studied in this work (413 μJ • cm^{-2}). This suggests that the phase transition toward the cubic phase is primarily driven by the presence of charge-carriers. In this respect, previous reports examining the calculated band structure of $MAPbI_3$ have observed that the highest occupied states of the valence band are primarily composed of nonbonding and antibonding molecular orbitals that are stabilized by the hydrogen bonding between the methylammonium cation and octahedral iodide, contributing to the octahedral distortions observed in the tetragonal phase.[154, 155] Thus, promoting an electron from the valence band maximum to the conduction band minimum may relax these distortions both by inducing organic cation motion that breaks the stabilizing hydrogen bonding, as recent ultrafast structural studies of metal halides materials have observed on picosecond time scales, while also strengthening the bonding orbitals in the Pb–I–Pb bonds that results in the relaxation of the octahedral distortions.[135, 156]

Importantly, many of the dynamic responses observed herein show pump fluence-independent behaviors in the limit of low fluence (at or below ∼100 μJ • cm^{-2}). Because the data shows that lifetimes are quantitatively independent of the number of photons with which we have excited the sample at low power, it is reasonable to suggest that such response occurs for wide-ranging optoelectronic applications, including solar cells. While the time scales of structural changes are fluence-independent at or below this fluence, all analyzed peaks exhibit fluence-dependent signal intensity, rising linearly up to 100 μJ • cm^{-2} and then exhibiting saturation at higher fluences (Figure 4. 4b). Given that Auger recombination becomes important for carriers at reported fluences close to ∼3–10 μJ • cm^{-2} and results in an appreciable increase in available

thermal energy,[116, 127, 148] this unexpected trend at low fluences also suggests that lattice heating from nonradiative relaxation pathways is not chiefly responsible for the phase transition mechanism. Features from the transient patterns at 1 ns after excitation for selected fluences were indexed to $Pm\bar{3}m$, the same reported space group as the known cubic structure of $MAPbI_3$. The observed diffraction intensities for this higher symmetry structure are consistent with the known, thermodynamically accessible cubic structure of $MAPbI_3$, thus we assign the cubic space group to the photoexcited structures at maximum signal intensity and acknowledge that this assignment may simplify the true excited structure owing to evaluation of a time-averaged response. Unexpectedly, the unit cell volumes were larger than reported values for the known, thermodynamic cubic phase at the phase transition temperature of 330 K (Figure 4. 4a). Though these transient expanded cubic parameters may also occur at higher temperatures, the structures observed here are nonequilibrium structures near room temperature. The presence of charge-carriers, then, likely accounts for the additional lattice expansion observed.

4.4 Conclusion

This is the first report that directly measures the *in situ* operative structure of $MAPbI_3$, as well as its dynamic behavior, under optical stimulation. We also notably identify several nonequilibrium structures and phenomena that have not been shown in studies where the structure is measured in equilibrium. Using ultrafast X-ray diffraction techniques, we identified and characterized the dynamic, photoexcited structures of $MAPbI_3$. We observed anisotropic distortions and rates of change along specific directions of the lattice as the material transitions from the starting phase to a higher-symmetry, metastable excited structure over 1 ns following photoexcitation. We also observed hysteresis between the rise and recovery behaviors of the

nonequilibrium phase transition, and we consider that the dynamic formation, stabilization, and dissipation of polarons along the *c*-axis of the lattice may be responsible. These structural changes have not been observed in the tetragonal-to-cubic phase transition in $MAPbI_3$, let alone at the low effective temperatures calculated in this study, indicating that these behaviors cannot be explained only by an increase in thermal energy due to photoexcitation. In this regard, a key aspect of future work will be to understand the quantitative contributions from each of the various energetic components that comprise the material's structural response to photoexcitation. This includes, but is not limited to, the thermal dissipation of incoming photon energy. Manipulating the excitation pump energies and ambient experimental temperatures can affect the kinetics of hot-carrier relaxation and Auger processes, advancing our understanding of photoexcited structural reorganization in hybrid perovskite materials. The dynamics of these nonequilibrium structures demonstrate the flexible lattice response of metal halide perovskites that facilitates favorable properties and provide further insight to enable new device architectures for both photovoltaics and novel applications that exploit ultrafast, nonequilibrium symmetry switches, such as quantum computing and information sciences.

Chapter 5. Dynamic Anisotropy in Photoexcited Lead Bromide Perovskites

5.1 Abstract

The influence of organic cations on the electronic properties of three-dimensional hybrid perovskites is intensely debated. In particular, formamidinium and methylammonium lead bromide are isostructural cubic $Pm\bar{3}m$ structures at room temperature with similar optical properties stemming from their inorganic sublattices; yet, investigations examining the local electronic structures in these materials have indicated that the cations significantly affect and alter carrier dynamics following photoexcitation due to differences in their individual chemical properties and orientations within the inorganic framework. In this work, we employ an ultrafast optical pump and time-resolved X-ray diffraction probe to excite an electronic transition in thin films of these perovskites and observe subsequent structural behavior. We demonstrate that while methylammonium lead bromide remains relatively unperturbed by photoexcitation, formamidinium lead bromide undergoes anisotropic expansion followed by a non-equilibrium phase transition to a lower symmetry structure. These findings further illuminate the unique role that organic cations play in templating the electronic structure of hybrid perovskites and their subsequent carrier dynamics, opening the potential for new functionalities based on cation selection in material design.

5.2 Introduction

Hybrid organic-inorganic perovskites of the composition AMX_3 (A = monovalent organic cation, M = divalent metal, X = halide) have been shown to exhibit many highly desirable functional properties for optoelectronic devices, and they have subsequently been fabricated using compositional analogs to achieve impressive power conversion efficiencies in photovoltaics. One particularly attractive aspect of hybrid perovskites is the ability to easily tune the electronic properties, such as the optical band gap and photoluminescent quantum yield, thus allowing for the broad development of materials with targeted properties in a variety of applications.[13] Indeed, the organic cations play a significant role in dictating the structures of hybrid perovskites with many bulkier organic molecules leading to electronically decoupled, two-dimensional inorganic quantum wells and other lower-dimensional analogs.

$MAPbBr_3$ and $FAPbBr_3$ share many similar electronic properties given the isostructural connectivity of the inorganic sublattice within the two materials. Several studies have shown that the inorganic sublattice is largely responsible for the observed optical properties with only slight variation exhibited in the local energy landscape and carrier dynamics across analogs with both organic and inorganic *A*-site cations.[157-159] It is difficult to isolate various aspects of the full contribution of each cation to the electronic and crystal structure in hybrid perovskites: each cation exhibits various degrees of freedom, molecular symmetry, and dielectric properties, among other crucial variations.[160, 161] Differences in the properties of these cations have been shown to significantly impact both the electronic and crystal structure by allowing or forbidding certain types of interactions between carriers and the greater lattice to occur, ultimately leading to some observed differences in carrier dynamics.[162] Specifically, studies examining the bromide analogs

following optical excitation observed changes in the electronic configurations of the cations while they were within the perovskite framework, suggesting the seemingly innocent cations are affected by changes in the electronic landscape of the inorganic sublattice and may contribute much more to carrier dynamics than is immediately apparent.[163] These investigations and others that closely examine the cations have continued to raise questions over the degree of influence exerted by specific properties of each unique cation with respect to the deviations from cubic within inorganic lattice connectivity and subsequent carrier dyamics.[164] These include considerations such as the steric/spatial overlap of cations within the inorganic lattice versus electronic interactions and intermolecular forces, such as hydrogen bonding, between the partially-negative halides and partially-positive amine moieties. Even though the disorder is local, the effects are seen over long-range order.

In this study, we employ time-resolved X-ray diffraction to investigate and compare the ultrafast structural dynamics of these two materials after pulsed laser photoexcitation. We use an above-bandgap optical pump and an X-ray probe with variable pump power and pump-probe time delay to quantify the behavior of photoexcited populations and their effects on the material structure. As photoexcitation perturbs the materials, we observe changes in powder diffraction patterns that indicate distortions of the crystal structure to accommodate new electronic configurations arising dynamically as the materials react and recover. We find that the two structures behave completely unlike each other, exhibiting different structural distortions as well as different timescales of those changes. We follow the structural evolution based on observations in the differenced powder patterns and find that the fundamental properties of the organic cation significantly dictate the types of structural deviations, both in crystalline and electronic

connectivity, that are observed to accommodate the influx of photons. These findings present direct implications for affecting carrier dynamics and material performance of hybrid perovskites in optoelectronic devices and other applications that necessitate irradiation of the material through designing cations with strategic electronic properties for desired outcomes.

5.3 Experimental Methods

Chemicals. Hydrobromic acid (48 wt %) 99.95%, hypophosphorous acid (50 wt %), dimethyl formamide (anhydrous), chlorobenzene, polymethyl methacrylate, lead (II) acetate powder ≥ 99% trace metals basis, methylamine hydrochloride ≥ 98%, and formamidine acetate were all purchased from Sigma Aldrich. Ethyl ether (anhydrous) was purchased from Fisher Scientific. Methylamine hydrochloride was dried in an oven at 70°C overnight before use. All other chemicals were used as received without further purification.

Synthesis of $MAPbBr_3$ crystals. A 50 mL Erlenmeyer flask was dried overnight at 110°C was charged with lead acetate powder (3253 mg, 10 mmol) and methylamine hydrochloride (676 mg, 10 mmol). Subsequently, 20 mL of hydrobromic acid and 1.8 mL of hypophosphorous acid were added to the flask while heating and stirring to afford a clear solution. The flask was removed from heat and allowed to cool to room temperature. Small, bright orange crystals precipitated out of solution upon cooling and were isolated from the reaction mixture through vacuum filtration over a medium-porosity fritted glass filter. The crystals were triple washed with diethyl ether and stored in an evacuated desiccator for at least 24 hours before further use.

Synthesis of $FAPbBr_3$ crystals. A 50 mL Erlenmeyer flask was dried overnight at 110°C was charged with lead acetate powder (3253 mg, 10 mmol) and formamidine acetate (1041 mg, 10 mmol). Subsequently, 20 mL of hydrobromic acid and 1.8 mL of hypophosphorous acid were

added to the flask while heating and stirring to afford a clear solution. The flask was removed from heat and allowed to cool to room temperature. Small, bright orange crystals precipitated out of solution upon cooling and were isolated from the reaction mixture through vacuum filtration over a medium-porosity fritted glass filter. The crystals were triple washed with diethyl ether and stored in an evacuated desiccator for at least 24 hours before further use.

Thin film fabrication. Single-crystal sapphire and fused quartz glass substrates (Ø25.4 mm × 1.6 mm) were cleaned in a sonicated bath using first soapy water, then deionized water, and finally acetone for ten minutes each. These washes were followed by 30 minutes of ultraviolet-ozone (UVO) treatment. The substrates and previously synthesized perovskite crystals were then transferred into a nitrogen atmosphere for the remainder of processing. A precursor solution was prepared by first dissolving the perovskite crystals (200 mg, 0.323 mmol) in 1 mL of dimethyl formamide and then syringe filtering through 0.2 µm-pore polytetrafluoroethylene (PTFE) membrane. Substrates were preheated to 110°C Films were synthesized by spin-coating 80 µL of the precursor solution onto the substrates at 1000 rpm for 30 seconds and then annealing at 110°C for 5 minutes. The films were then coated in a concentrated solution of polymethyl methacrylate in chlorobenzene and annealed at 110°C for 5 minutes. The resulting films were stored in the dark under nitrogen until use.

Time-Resolved X-ray Diffraction. TR-XRD experiments were conducted using synchrotron radiation at beamline 11-ID-D of the Advanced Photon Source (APS), Argonne National Laboratory. Laser pulses were generated using the frequency-doubled output from a Ti:sapphire regeneratively amplified laser with 10 kHz repetition rate, producing 3.1 eV (400 nm) incident pump energy with 1.2 ps pulse width and elliptical spot size of 1200 × 6900 µm (area =

0.06557 cm^{-2}). Laser fluence at the sample was adjusted using neutral density filters, and time delays were mechanically created using a translation stage and retroflector. The X-ray probe beam was diverted using two inline undulators from the APS storage ring in 24-bunch mode to provide 11.57 keV (λ = 1.05969 Å) probe pulses at 6.5 MHz repetition rate with 79 ps pulse width. The laser pump and X-ray probe were orthogonally overlapped onto the surface of the spinning film, which was tilted at an angle of 4° to the incident X-rays. The Pilatus 2M detector was placed ~202 mm from the sample and temporally gated to measure scattering intensity only at the laser-synchronized probe pulses. Detector image plates were collected and integrated over twenty seconds of exposure time. The subsequent scattering intensity was azimuthally integrated to produce diffraction patterns and then averaged over six cycles for each time delay. Image plate pixel values were calibrated to Q /$Å^{-1}$ using the azimuthally integrated diffraction pattern of a CeO_2 standard.

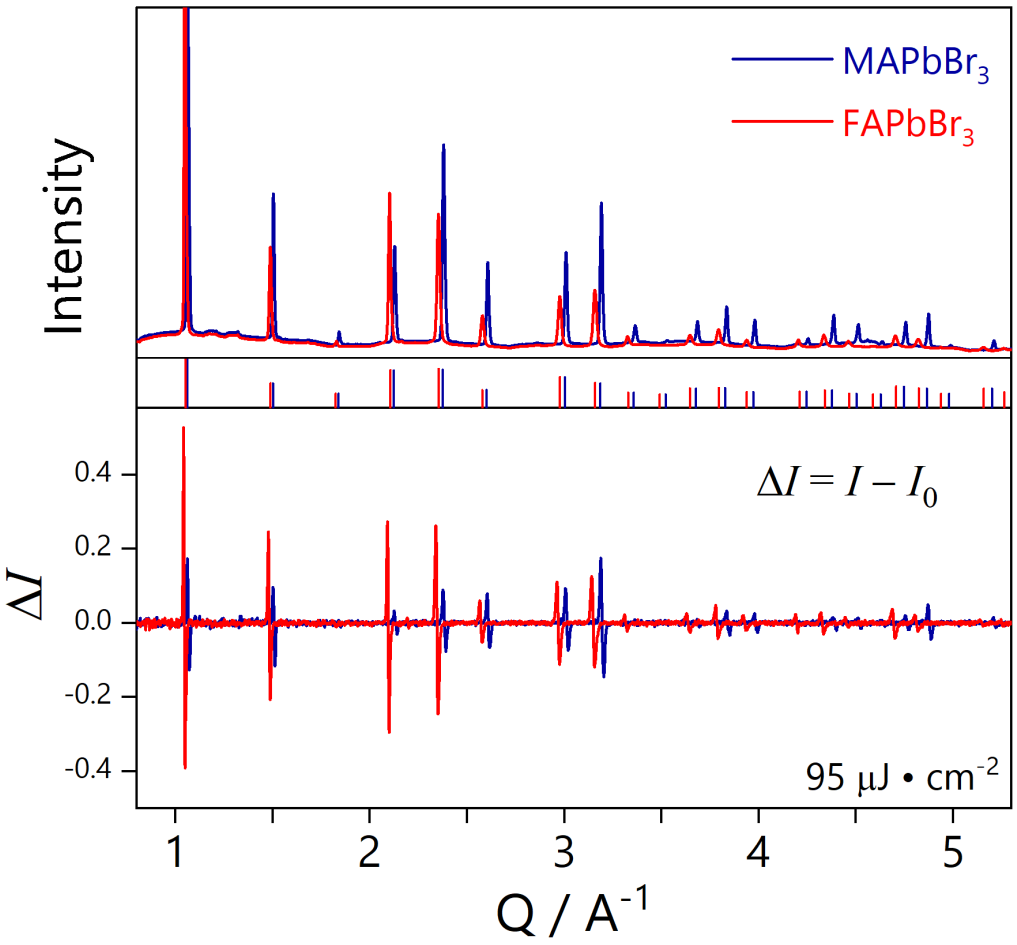

Figure 5. 1. Steady-state (above) and transient, excited-state (below) patterns. $MAPbBr_3$ (blue) and $FAPbBr_3$ (red) sample films with expected Bragg reflection positions indicated from single crystal X-ray diffraction data. Transient patterns are shown for 1 ns time delay at a representative fluence of 95 μJ • cm^{-2}. While both starting materials are shown to exhibit cubic symmetry at room temperature, the positions of Bragg reflections for these isostructural starting materials differ slightly relative to each other. These variations likely arise from differences in cation orientation and disorder. Thermal energy present at room temperature causes the cations to rotate rapidly within the framework, leading to changes in the local bonding and lattice connectivity that result in different lattice parameters between the two analogs.

5.4 Results and Discussion

In Figure 5. 1, steady-state and transient, excited-state patterns of both $MAPbBr_3$ and $FAPbBr_3$ sample films are shown. We observe asymmetry in the peak at 1.05 A^{-1} in the steady-

state pattern of $FAPbBr_3$, corresponding to the (100) Bragg reflection in cubic symmetry. Close examination of other peaks within this family of planes, such as the (200) and (300) reflections at 2.05 A^{-1} and 3.05 A^{-1} respectively, do not reveal systematic evidence of either secondary phases or lower symmetry domains, which would have resulted in additional symmetry-forbidden peaks or peak asymmetry with splitting that became more pronounced with increasing Q. While both starting materials are shown to exhibit cubic symmetry at room temperature, the positions of Bragg reflections for these isostructural starting materials differ slightly in relation to one another. These variations arise from differences in cation orientation and disorder at room temperature. Sufficient thermal energy is present for each cation to rotate rapidly within the framework, causing changes in the local bonding and lattice connectivity based on the rate and magnitude of motion and resulting in different lattice parameters between to the two analogs.

Peaks within the same family for the cubic space group expand at different rates to different magnitudes. This indicates anisotropic expansion along certain axes of the structure, even though all axes are equivalent at room temperature. This may be empirical evidence that the electronic structure, at least locally, is not isotropic, even though the long range crystallographic ordered structure is. Crystal structures are determined by X-ray diffraction which measures electronic density in reciprocal space. According to valence-shell electron-pair repulsion (VSEPR) theory, electronic geometry and molecular geometry are not equivalent in the presence of lone pairs. The lone pair on the central Pb atom is active, imparting structural influence on the local bonding and connectivity.[165] As photoexcitation disrupts the energy landscape, local rotations and fluctuations, which appear isotropic when averaged over the steady-state structure, suddenly become operative in dictating connectivity.

Chapter 6. Conclusions and Outlook

Fundamental investigations of photophysical dynamics are indispensable to the development of solar-driven energy technology, guiding synthetic design and uncovering the basis of electronic behavior that dictates most chemical research. In this work herein, several studies are presented that examine specific, structural aspects of hybrid and nanostructured materials in order to deconvolute the complex relationship between electronic behavior and material structure.

Chapters 2 and 3 examine trends across systems of nanomaterials, isolating individual variables with respect to sample morphology and composition in order to establish quantitative trends and provide evidence to support predictive theoretical modelling in similar systems. Quantitatively investigating distance dependence of FRET between 2D donor and acceptor states within extended solids relied on careful selection of perovskite quantum wells and compositional components such that the dielectric environments and effects from other convoluting electronic factors were negligible. Meanwhile, modified transient absorption setups were necessary to ensure reliable measurements of spin-coherence in colloidal nanoplatelet systems that could minimize noise and target phenomena of interest.

Chapter 4 and 5 focus on well-known compounds, where many of the contributing aspects to the electronic structure have been studied and isolated by previous studies. Time-resolved X-ray diffraction experiments instead required consideration of the many overlapping physical processes in order to generate a holistic narrative that accounted for all the observed dynamic structural behavior. Individual electronic pathways were probed across various timescales and incident photoexcitation powers, utilizing the versatility of the experimental setup to examine

variables within the different systems. In this way, the presence of thermal and electronic effects could be slowly disentangled.

Gaining useful insights from ultrafast spectroscopy is non-trivial, demanding directed hypotheses from researchers and extremely intentional, attentive data analysis. Indeed, gaining the information offered through ultrafast spectroscopic experiments necessitates establishing sample systems with clear variables of interest and rigorous monitoring for competing influences. With such a variety of approaches, the breadth of potential photophysical studies alone that could significantly accelerate the pace of synthetic design and theoretical understanding is staggering. Yet, interdisciplinary efforts are often key in deriving quantitative relationships, with combined theoretical and photophysical studies resulting in key explanations for observed behaviors. Ultrafast experiments of further complexity and greater prospective discoveries, especially with the impetus of impending climate crises, need to be conducted in collaboration with synthetic, structural, and theoretical expertise to form robust design principles for energy technology.

Appendix A: Supplementary Information for Chapter 2.

Reprinted with permission from "Shobhana Panuganti, Lucas V. Besteiro, Eugenia S. Vasileiadou, Justin M. Hoffman, Alexander O. Govorov, Stephen K. Gray, Mercouri G. Kanatzidis, and Richard D. Schaller. *J. Am. Chem. Soc.* **2021** *143* (11), 4244-4252."

A.1 Experimental Methods

Chemicals. Butylamine (99.5%), hexylamine (99%), octylamine (99%), hydroiodic acid (57 wt %, 99.95%), hypophosphorous acid (50 wt %), dimethylformamide (anhydrous), lead(II) oxide powder (≥99% trace metals basis), and methylamine hydrochloride (≥98%) were all purchased from Sigma-Aldrich. Ethyl ether (anhydrous) was purchased from Fisher Scientific. Methylamine hydrochloride was dried in an oven at 70 °C overnight before use. All other chemicals were used as received without further purification.

Crystal Syntheses.[79, 80]

General Procedure for n = *1.* PbO powder (2232 mg, 10 mmol) was added to hydroiodic acid in a 50 mL Erlenmeyer flask and heated to boiling while stirring to afford a bright yellow solution. In a separate vial, the alkylamine was neutralized with 2 mL of hypophosophorous acid in an ice bath. The alkylammonium solution was then added to the reaction mixture. Orange precipitate initially crashed out but redissolved after additional heating. The reaction mixture was removed from heat and allowed to cool to room temperature to facilitate the precipitation of the crystalline product from the solution. The precipitate was separated from the reaction by vacuum filtration and washed with diethyl ether over a medium porosity fritted glass filter to afford orange, flake-like crystals. Crystals were stored in an evacuated desiccator until further use.

General Procedure for n = *2*. PbO powder (2232 mg, 10 mmol) and methylamine hydrochloride were added to hydroiodic acid in a 50 mL Erlenmeyer flask and heated to boiling while stirring to afford a bright yellow solution. In a separate vial, the alkylamine was neutralized with 2 mL of hypophosophorous acid in an ice bath. The alkylammonium solution was then added to the reaction mixture and dissolved completely. The reaction mixture was removed from heat and allowed to slowly cool to room temperature to facilitate the precipitation of the crystalline product from the solution. The precipitate was separated from the reaction by vacuum filtration and washed with diethyl ether over a medium porosity fritted glass filter to afford red, flake-like crystals. Crystals were stored in an evacuated desiccator until further use.

For $(C_4H_9NH_3)_2PbI_4$, the general procedure for $n = 1$ was followed using butylamine (925 µL, 9.34 mmol) in 15 mL of hydroiodic acid; for $(C_6H_{13}NH_3)_2PbI_4$, the general procedure for $n = 1$ was followed using hexylamine (800 µL, 6.08 mmol) in 18 mL of hydroiodic acid; for $(C_8H_{17}NH_3)_2PbI_4$, the general procedure for $n = 1$ was followed using octylamine (700 µL, 4.24 mmol) in 20 mL of hydroiodic acid.

For $(C_4H_9NH_3)_2(CH_3NH_3)Pb_2I_7$, the general procedure for $n = 2$ was followed using butylamine (694 µL, 7 mmol), methylamine hydrochloride (338 mg, 5 mmol), and 15 mL of hydroiodic acid; for $(C_6H_{13}NH_3)_2(CH_3NH_3)Pb_2I_7$, the general procedure for $n = 2$ was followed

using hexylamine (580 μL, 4.39 mmol), methylamine hydrochloride (338 mg, 5 mmol), and 18 mL of hydroiodic acid; for $(C_8H_{17}NH_3)_2(CH_3NH_3)Pb_2I_7$, the general procedure for $n = 2$ was followed using octylamine (165 μL, 1.02 mmol), methylamine hydrochloride (338 mg, 5 mmol), and 20 mL of hydroiodic acid.

Thin-Film Syntheses.[46]

General Procedure. Amorphous glass substrates (2.5 cm × 2.5 cm × 1 mm) were cleaned 3× using deionized water followed by acetone and finally ethanol in a sonicated bath for 10 min. The substrates were then preteated for 10 min using an ultraviolet ozone (UVO) treatment method. Phase-pure $n = 1$ and $n = 2$ crystals were dissolved into 300 μL of dimethylformamide (DMF) in a nitrogen atmosphere. The glass substrate that was preheated to 110 °C was quickly transferred (1.5 s) to the spincoating stage. Thirty μL of the solution was then immediately spincoated onto the substrate and spun at 4000 rpm for 30 s. The resulting films were stored in a nitrogen atmosphere until further use. In the following, the films are denoted by the alkylammonium carbon chain length and the layer thickness; e.g., C4n1 refers to a film synthesized with butylammonium (four carbons) and of $n = 1$ phase and so forth.

C4n1. The general procedure for film synthesis was followed using 40 mg of $(C_4H_9NH_3)_2PbI_4$ dissolved into DMF.

C4n1 and C4n2 Mixture. The general procedure for film synthesis was followed using 20 mg of $(C_4H_9NH_3)_2PbI_4$ and 20 mg of $(C_4H_9NH_3)_2(CH_3NH_3)Pb_2I_7$ dissolved into DMF.

C4n2. The general procedure for film synthesis was followed using 40 mg of $(C_4H_9NH_3)_2(CH_3NH_3)Pb_2I_7$dissolved into DMF.

C6n1. The general procedure for film synthesis was followed using 40 mg of $(C_6H_{13}NH_3)_2PbI_4$ dissolved into DMF.

C6n1 and C6n2 Mixture. The general procedure for film synthesis was followed using 20 mg of $(C_6H_{13}NH_3)_2PbI_4$and 20 mg of $(C_6H_{13}NH_3)_2(CH_3NH_3)Pb_2I_7$dissolved into DMF.

C6n2. The general procedure for film synthesis was followed using 40 mg of $(C_6H_{13}NH_3)_2(CH_3NH_3)Pb_2I_7$dissolved into DMF.

C8n1. The general procedure for film synthesis was followed using 40 mg of $(C_8H_{17}NH_3)_2PbI_4$ dissolved in DMF.

C8n1 and C8n2 Mixture. The general procedure for film synthesis was followed using 20 mg of $(C_8H_{17}NH_3)_2PbI_4$and 20 mg of $(C_8H_{17}NH_3)_2(CH_3NH_3)Pb_2I_7$, dissolved in DMF.

C8n2. The general procedure for film synthesis was followed using 40 mg of $(C_8H_{17}NH_3)_2(CH_3NH_3)Pb_2I_7$, dissolved into DMF.

X-ray Diffraction Measurements. PXRD patterns were collected on a Rigaku Miniflex600 powder X-ray diffractometer (Cu Kα, λ = 1.5406 Å) operating at 40 kV/15 mA with a graphite monochromator and Kβ foil filter. Single-crystal X-ray diffraction was performed using a STOE IPDS II diffractometer (Mo Kα, λ = 0.71073 Å) operating at 50 kV/40 mA with a graphite monochromatizer.

Static Optical Measurements. Absorption spectra were measured using a Shimadzu 3600 UV−vis−NIR spectrophotometer. PL spectra were collected under 405 nm front-facing photoexcitation with a 35 fs pulse width laser diode.

Scanning Electron Microscopy. Scanning electron microscope images were acquired using a Hitachi SU4800-II cFEG SEM at an accelerating voltage of 2.0 kV. Materials were precoated with osmium using an SPI Osmium coater.

Transient Spectroscopy.
Ultrafast experiments were performed using a Ti:sapphire amplifier with 2 kHz repetition rate and 35 fs pulse width. 400 nm pump pulses were generated using the frequency doubled output of the laser with a BBO crystal. Time-resolved photoluminescence measurements were collected using a streak camera with front-facing excitation. Photon counts were accumulated for 15 ms over 30,000 integrations. In transient absorption experiments, a small portion of the 800 nm Ti:sapphire output was focused into a sapphire crystal to produce white light probe pulses. 545 nm pump pulses were generated from the 800 nm laser output using an optical parametric amplifier (OPA). Probe pulses were mechanically time delayed using a translation stage and retroflector. Transient absorption spectra for each time point were averaged for 2 s, and then, three reproducible, separate scans were averaged together. Background subtraction and probe chirp correction were conducted for all raw spectra before data analysis. All spectroscopic studies were performed at room temperature and in ambient conditions.

A.2 Static characterization

a) Powder X-ray diffraction (PXRD)

PXRD patterns of the as-prepared crystalline precursors (Fig S1) and mixed films (Fig. S2) were compared to calculated patterns from single crystal diffraction data.[166-169] Both crystalline and film materials showed preferred orientation along the stacking axis (perpendicular to the 2D PQWs), as calculated based on the March-Dollase approach. Peak matching confirmed the desired phases ($n = 1$ or $n = 2$) without the presence of secondary phases from higher layer n phases or degradation of material.

The presence of low-angle Bragg reflections in the mixed film patterns provides evidence of the parallel orientation of the inorganic layers to the substrate. Additionally, the d-spacing for the low angle peaks (below characteristic bulk reflections at $2\theta \sim 15°$) represent the distance from the center of each n-layer, enabling estimation of specific n phases by the positions of these reflections.

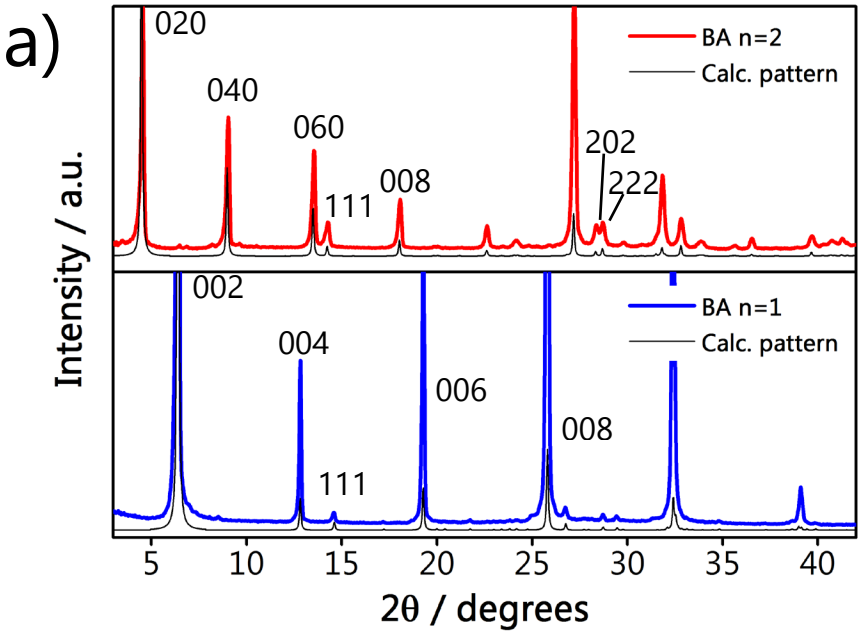
a)
020
040
060
111
008
202
222
BA n=2
Calc. pattern
002
004
111
006
008
BA n=1
Calc. pattern
Intensity / a.u.
5
10
15
20
25
30
35
40
2θ / degrees

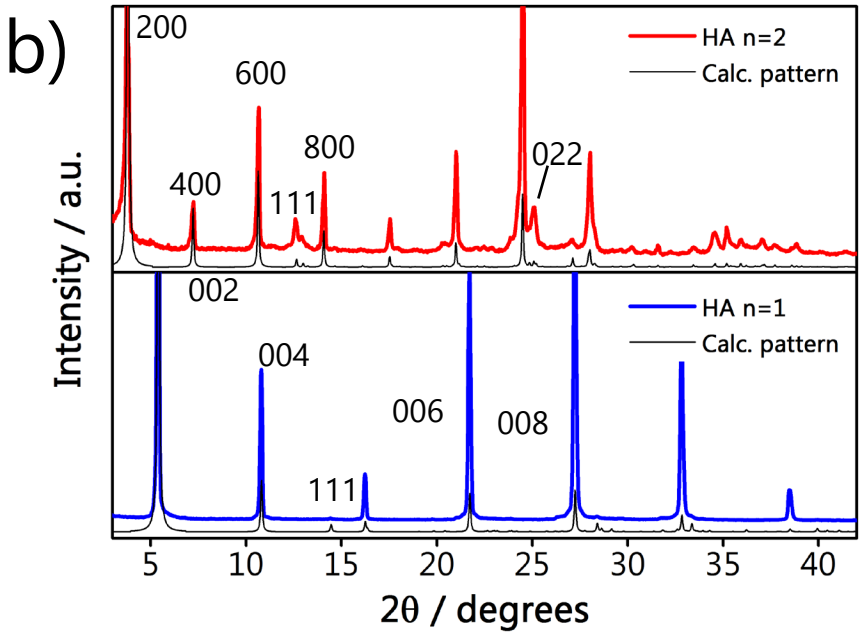
b)
200
600
400
111
800
022
HA n=2
Calc. pattern
002
004
111
006
008
HA n=1
Calc. pattern
Intensity / a.u.
5
10
15
20
25
30
35
40
2θ / degrees

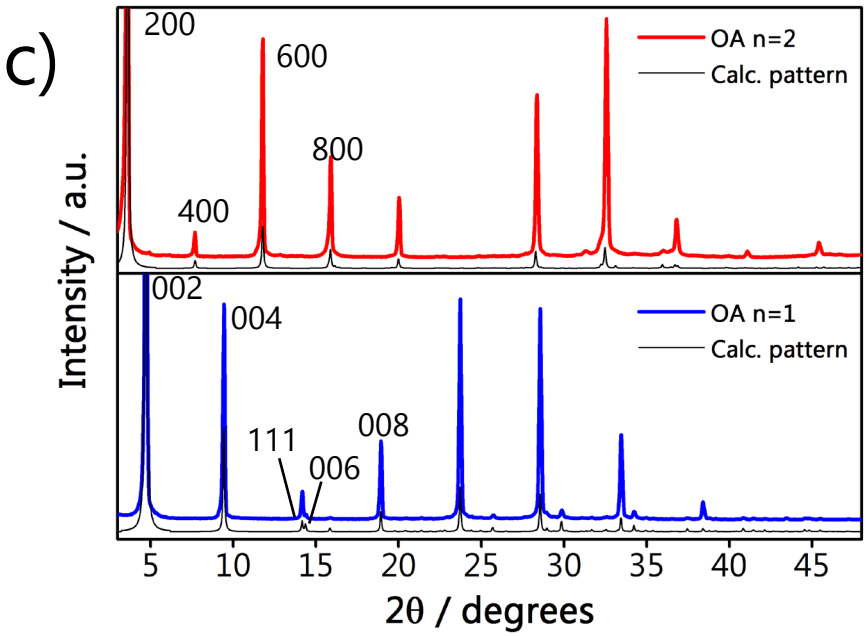

Figure A. 1. Donor *n = 1* (blue) and acceptor *n = 2* (red) PXRD patterns for crystalline materials. a) butylammonium b) hexylammonium and c) octylammonium as the A' site cation. Miller indices of corresponding Bragg reflections are indicated.

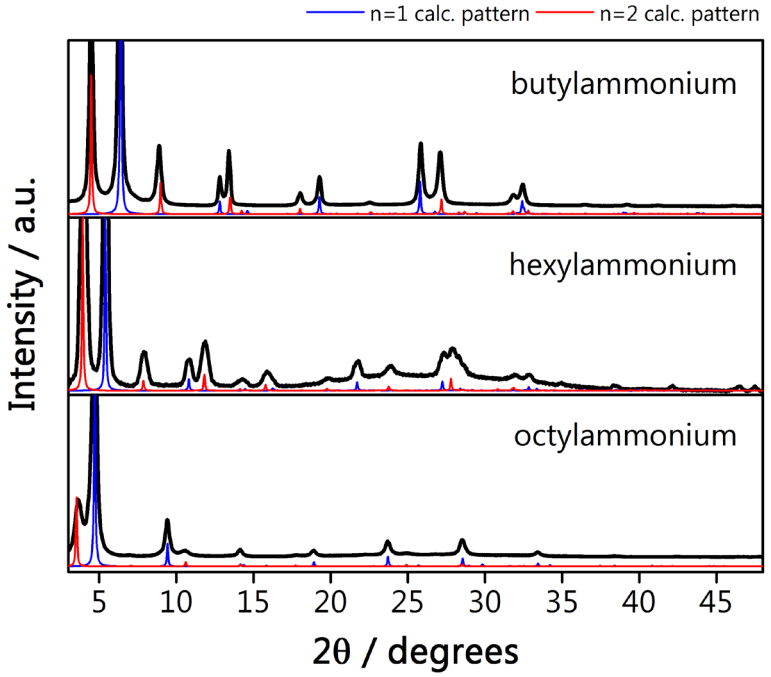

Figure A. 2. Mixed binary films of butylammonium, hexylammonium, and octylammonium A' site cation materials.

b) Optical properties (absorption, photoluminescence)

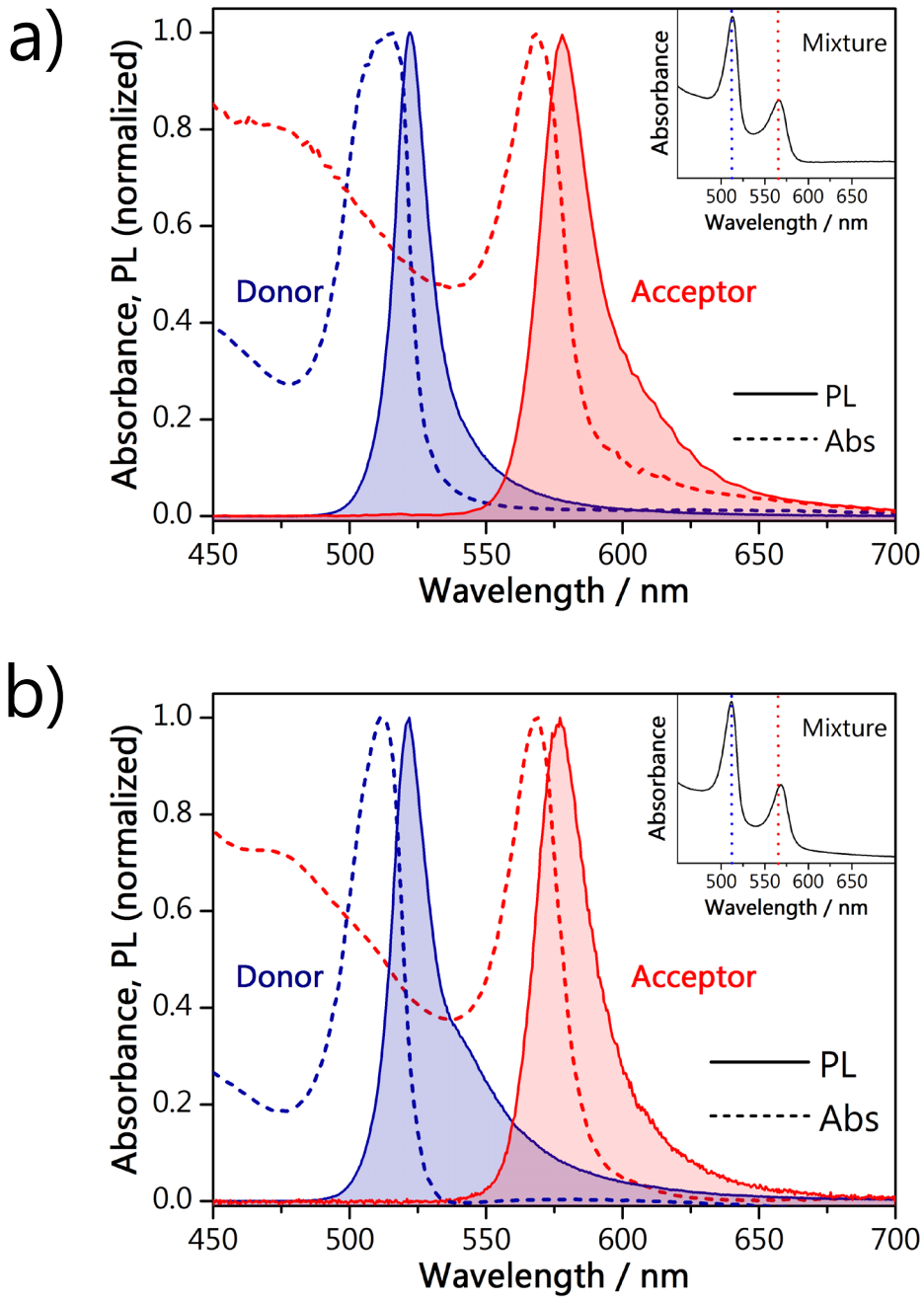

Figure A. 3. Absorption and photoluminescence spectra of films.
Donor ($n = 1$) and acceptor ($n = 2$) phases, as well as binary mixture films (insets) of a) hexylammonium and b) octylammonium. See Fig. 1 (main text) for butylammonium.

c) Scanning electron microscopy (SEM)

We collected SEM images of each mixed binary donor *n = 1* and acceptor *n = 2* film. Images show homogenous surface coverage and significant overlap of domains throughout depth and breadth of the films. Moreover, we expect that both donor and acceptor are present within an individual grain, ensuring surface overlap of the *n* layers separated only by the alkylammonium cations.

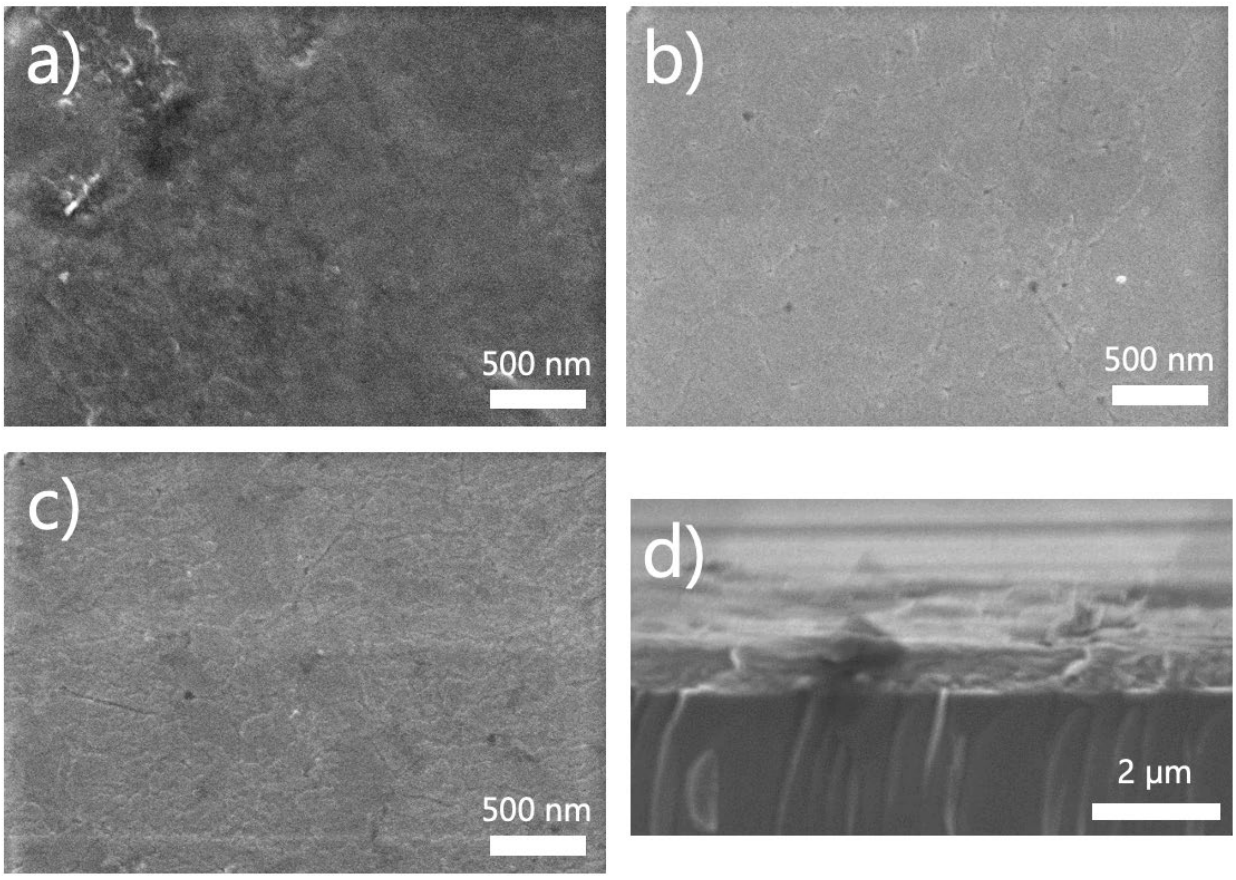

Figure A. 4. Mixed binary films.
a) butylammonium, b) hexylammonium, and c) octylammonium A' site cation materials with d) cross-sectional image of hexylammonium binary film.

A.3 Transient spectroscopies

a) Transient absorption (TA) spectroscopy

TA spectra were collected on neat donor (*n = 1*) films and binary films of BA, HA, and OA materials using both 400 and 545 nm excitation. Spectral and kinetic data are the average of three scans. Initial power dependent measurements of BA *n = 1* films were conducted in order to determine fluence limits of single-exciton regimes in these materials. In all studies, a fluence of 2.13 μJ•cm^{-2} was used (4.28•10^{15} photons•cm^{-2} for 400 nm pump, 5.83•10^{15} photons•cm^{-2} for 545 nm pump). Data was collected in triplicate using three separately fabricated thin film samples for each material.

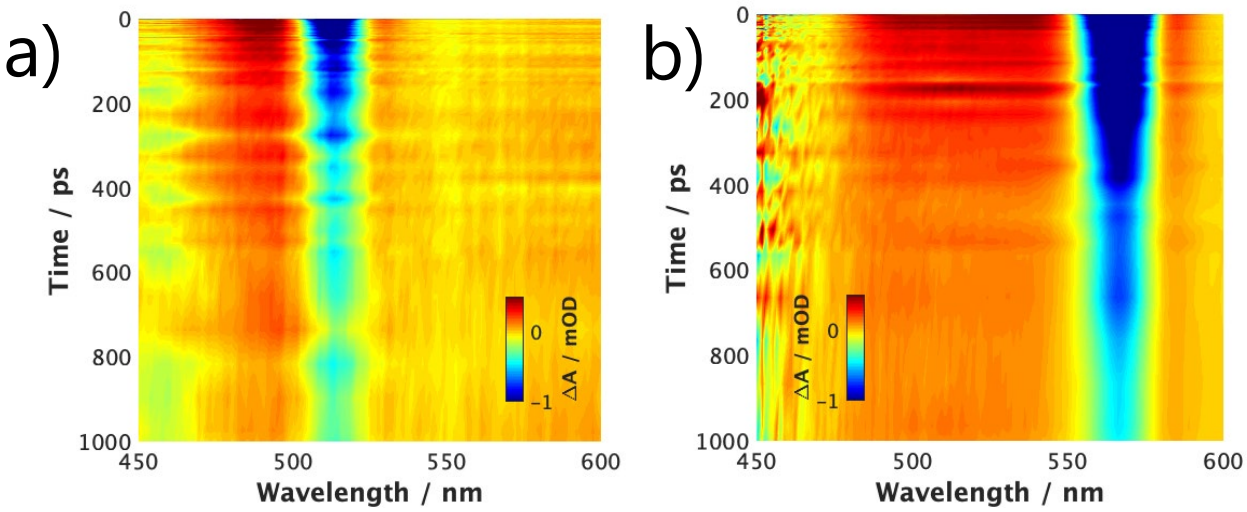

Figure A. 5. Time-resolved absorption spectral maps as a function of probe wavelength. a) Neat butylammonium donor (*n = 1*) film at 400 nm excitation, and b) mixed binary film at 545 nm excitation to obtain butylammonium acceptor (*n = 2*).

b) Time-resolved photoluminescence (trPL)

trPL measurements were collected on neat donor (*n = 1*), neat acceptor (*n = 2*), and binary films of BA, HA, and OA materials. Spectral and kinetic data were collected using 30,000 integrations of charge-coupled device (CCD) detector plate collections. A fluence of 2.13 μJ • cm^{-2} (4.28 • 10^{15} photons • cm^{-2}) at 400 nm excitation was used.

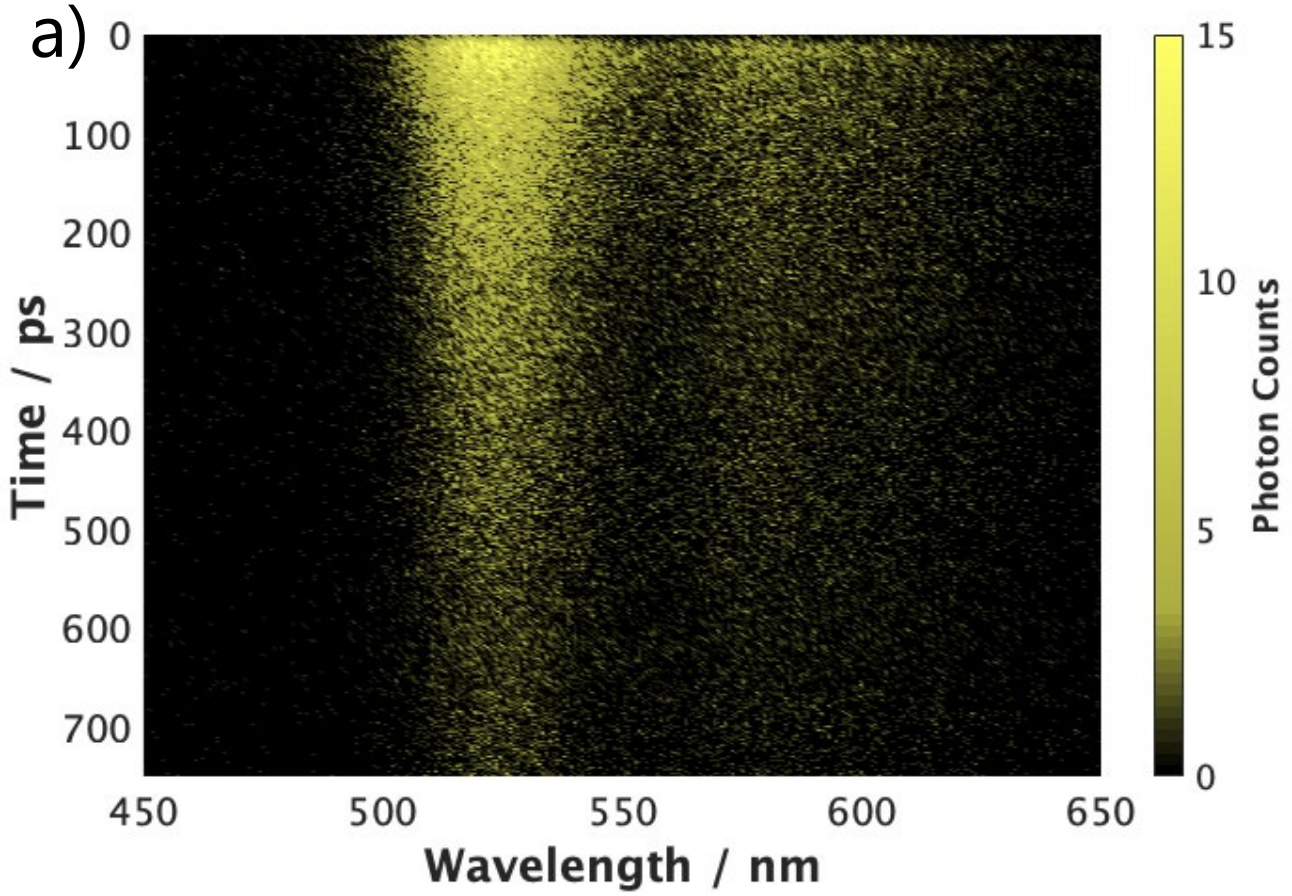
a)
0
100
200
300
400
500
600
700
Time / ps
450
500
550
600
650
Wavelength / nm
15
10
5
0
Photon Counts

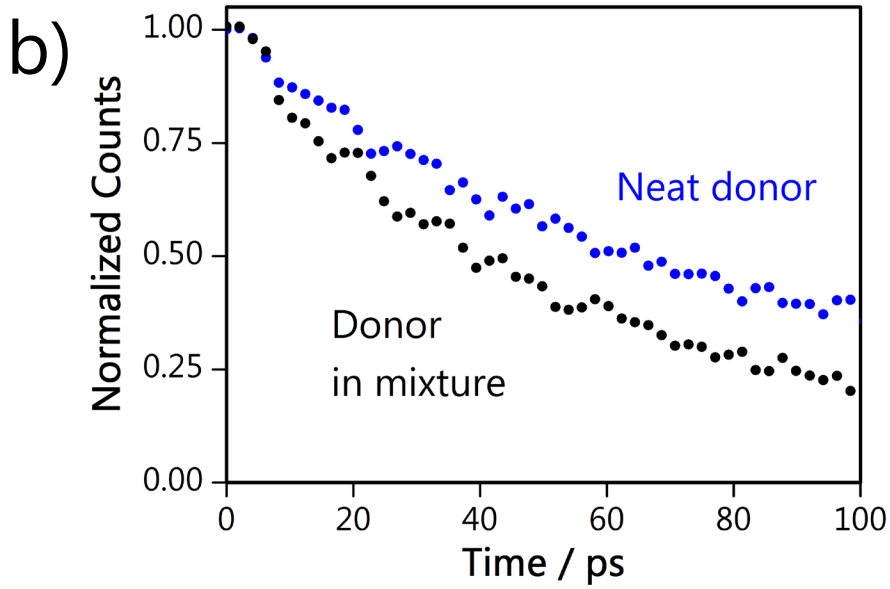
b)
1.00
0.75
0.50
0.25
0.00
Normalized Counts
Neat donor
Donor
in mixture
0
20
40
60
80
100
Time / ps

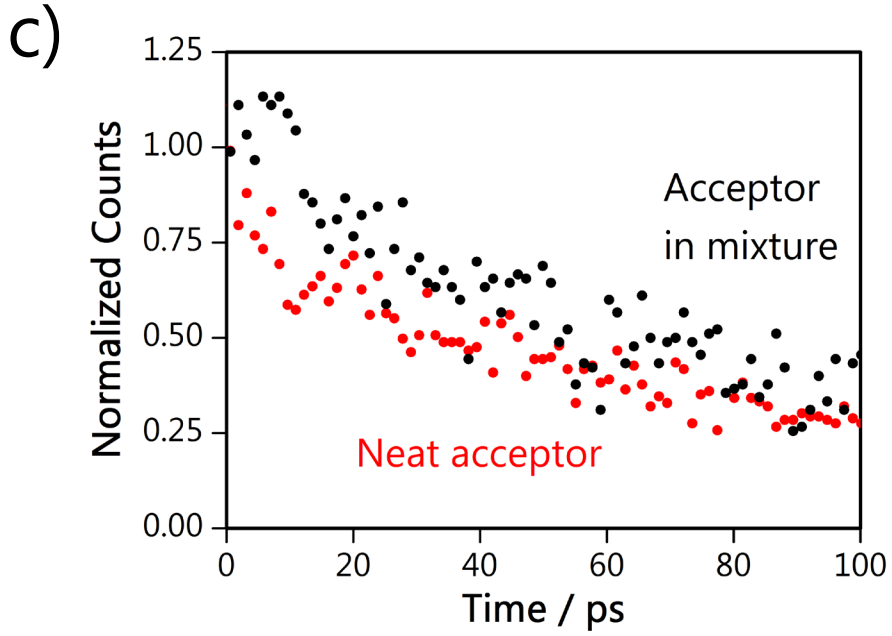

Figure A. 6. Time-resolved photoluminescence data of octylammonium neat and binary materials. Kinetic data are normalized at $t = 0$ ps which is the moment of incident excitation.
a) Time-resolved photon counts as a function of emission wavelength for the binary film, b) normalized emission dynamics at 521 nm from phase pure $n = 1$ and mixture, and c) normalized emission dynamics at 580 nm from phase pure $n = 2$ and mixture. An increase in emission after initial excitation is observed for the acceptor in mixture trace, which is consistent with FRET.

A.4 Distance determinations

For each alkylammonium donor *n = 1* phase and for butylammonium and hexylammonium acceptor *n = 2* phases, single crystal X-ray diffraction information was obtained from previously published works.[166-169] In the case of octylammonium acceptor *n = 2* phase, single crystal X-ray diffraction data was collected using a solution-grown single crystal of $(C_8H_{17}NH_2)_2(CH_3NH_3)Pb_2I_7$. Distances were calculated using VESTA software.[170] First, the distance between centers of PQWs for an individual *n* phase were obtained by calculating the *d*-spacing for planes that bisected and bounded the inorganic PQWs. In particular, we examined reflections along the (00*l*) family of planes in *n = 1* and along (0*k*0) and (*h*00) in *n = 2,* parallel to the stacking axis. Distances d_D represent the empirical interlayer distances for *n = 1* crystals and distances d_A represent the empirical interlayer distances for *n = 2* crystals. Final distances, d_{DA}, from the center of the donor PQW to the center of the acceptor PQW, were calculated by taking the average of distances d_D and d_A for the individual phases.

Table A. 1. Distance data for BA, HA, and OA donor *n = 1* and acceptor *n = 2* neat phases and binary mixtures. Values calculated from crystal structure information obtained through single crystal X-ray diffraction.

Alkylammonium	d_D / Å	d_A / Å	d_{DA} / Å
butylammonium	13.1165	19.6105	16.3635
hexylammonium	16.052	22.6776	19.3648
octylammonium	18.738	25.2162	21.9771

A.5 Theoretical modelling

The relative orientation of the donor and acceptor dipoles, as well as the overall dipole strength, has a significant effect on the rate and efficiency of FRET. Specifically, FRET is most efficient when the two dipoles are parallel to each other such that the dot product of the acceptor dipole and donor electric field is 1. Parallel stacking of $n = 1$ and $n = 2$ layers, as is present in our films, satisfies requisite dipole orientation for most efficient FRET.

We simulate various dipole strengths (Figure S7) and configurations ranging from parallel to perpendicular dipole orientation (Figure S8), highlighting the sensitivity of the system to these parameters. While small increases in dipole strength appear to noticeably decrease FRET lifetimes, especially at longer distances, the results suggest relative dipole orientation has a less pronounced effect for this system.

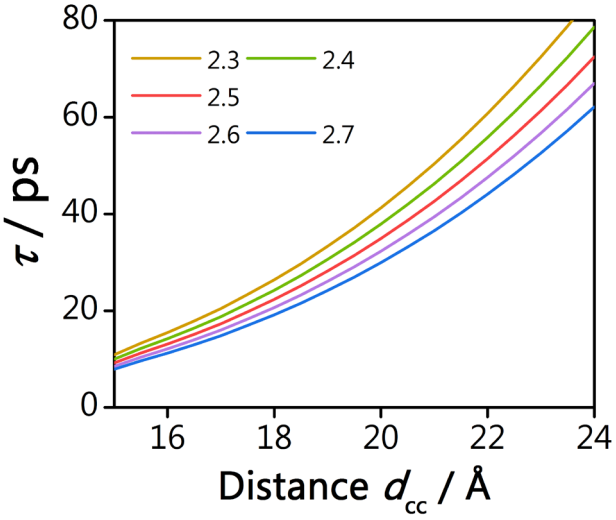

Figure A. 7. Calculated FRET lifetimes as a function of dipole strength.
For various donor dipole strengths μ of 2.3, 2.4, 2.5, 2.6, and 2.7 in eÅ, as a function of center-to-center distance between donor and acceptor states. Previously reported value of μ = 2.5 eÅ was utilized in all other calculations.

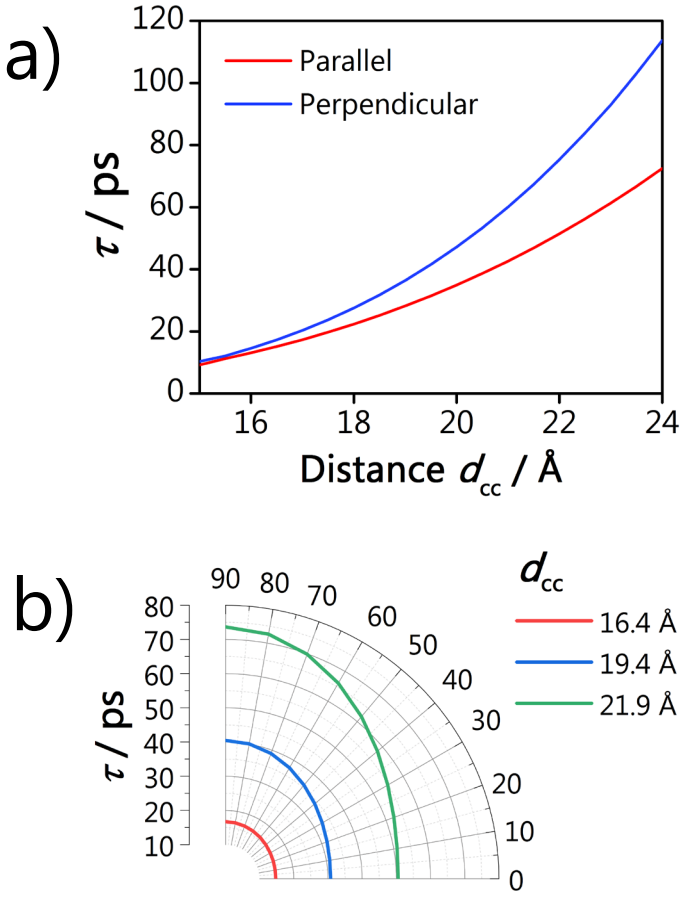

Figure A. 8. Calculated lifetimes as a function of dipole orientation
a) Calculated FRET lifetimes as a function of center-to-center distance between donor and acceptor states for parallel (red) and perpendicular (blue) dipole orientations. b) Calculated FRET lifetimes as a function of dipole orientation for center-to-center distances of 16.4 Å (red), 19.4 Å (blue), and 21.9 Å (green) between donor and acceptor states, corresponding to empirical distances for the alkylammonium spacers used in this study. Dipole orientation is expressed as the angle the dipole and the plane of the nanosheets where θ = 0 is a parallel configuration, as in the main text, and θ = 90 is perpendicular.

Appendix B: Supplementary Information for Chapter 3.

Reprinted with permission from "Phillip I. Martin, Shobhana Panuganti, Joshua C. Portner, Nicolas E. Watkins, Mercouri G. Kanatzidis, Dmitri V. Talapin, and Richard D. Schaller. *Nano Letters* **2023** *23* (4), 1467-1473."

B.1 Experimental Methods

Chemicals. 1-Octadecene (90%, Aldrich), Oleic Acid (90%, Aldrich), Oleylamine (technical grade, 70%, Aldrich), Selenium (100 mesh powder, 99.99%, Aldrich), Cadmium Nitrate Tetrahydrate ($Cd(NO_3)_2$ $4H_2O$, 98%, Aldrich), Cadmium Formate ($Cd(HCOO)_2$, anhydrous, MP Biomedicals), Cadmium Acetate dihydrate ($Cd(OAc)_2$, $2H_2O$, Aldrich), Lithium sulfide (98%, Strem), and Methylcyclohexane (anhydrous, Aldrich). Octadecene, oleic acid, and oleylamine were degassed at 100 °C and transferred to a nitrogen filled glovebox.

Synthesis of 5 ML CdSe NPLs. The synthesis of 5 ML CdSe NPLs was performed following previous literature.[84] Briefly, 170 mg of $Cd(myristate)_2$ in 14 mL octadecene (ODE) was degassed for 2 hours at 100 °C. Under nitrogen flow, the flask was heated to 240 °C and 1 mL of a 0.15 M Se solution sonicated in ODE was swiftly injected. After 30 seconds, 90 mg of $Cd(acetate)_2$ dihydrate was quickly added by lab spoon under a positive nitrogen flow and the flask was quickly resealed with a rubber septum. The solution was heated for 10 minutes with the temperature increased to 245 °C, then quickly cooled by air flow. At 100 °C, a solution of 2 mL oleic acid in 15 mL methylcyclohexane (MCH) was added and the solution was stirred under nitrogen overnight. The NPLs were isolated by centrifugation at 11000 rpm for 10 minutes. The resulting precipitate was redispersed in MCH and filtered through a 0.22 μm PTFE filter.

Synthesis of 5CdSe/*X*CdS NPLs. Cadmium sulfide shells were grown on core 5 ML NPLs by colloidal atomic layer deposition (c-ALD) based on previously reported methods.[85] Core NPLs (~20 mg) were precipitated from the stock solution in MCH with ethanol and transferring to a nitrogen filled glovebox. The NPLs were redispersed in 100 μL MCH and combined in a 4 mL vial with 500 μL ODE, 100 μL oleylamine, and 10 mg Li_2S with a Teflon coated stir bar. The vial was stirred at 150 °C on a hot plate (temperature measured by an ODE solution in an identical 4 mL vial) for 1 minute. After cooling, the Li_2S solids were removed by centrifugation and decantation, and additional NPLs were recovered from the precipitate with 50 μL MCH. The S^{2-} capped NPL solution was then precipitated with 2 mL ethanol and redispersed in 100 μL MCH. The Cd layer was grown by adding the NPL solution to a 4 mL vial containing 500 μL ODE, 100 μL oleylamine, and 10 mg $Cd(formate)_2$ and stirring at 150 °C for 3 minutes. Any remaining solids were removed by centrifugation and decantation, then the solution was washed with 1 mL ethanol and redispersed in 100 μL MCH. This completed one monolayer of cadmium sulfide. Additional monolayers were grown by repeating the same procedure. Oleylamine and ODE were dried at 100°C for two hours under vacuum and transferred to a nitrogen filled glovebox. All steps were performed in a nitrogen glovebox.

Synthesis of 5CdSe/*X*ZnS NPLs. Cadmium and zinc sulfide shells were grown on CdSe nanoplatelets using a modified c-ALD technique.[2] In the first half reaction, 10 mg anhydrous Li_2S,

50 µL oleylamine, 500 uL ODE, and ~10 mg CdSe NPLs in 100 µL MCH were combined and stirred at 150°C for 1 minute with a Teflon coated stir bar. The reaction was cooled to room temperature, and residual solids were removed by centrifugation. The NPLs in the liquid phase were purified by washing with ethanol and redispersing in MCH two times. In the second half reaction, 10 mg zinc acetate, 50 µL oleylamine, 500 µL ODE, and the S^{2-} capped NPLs in 100 µL MCH were combined and stirred at 150°C for 5 minutes. The reaction was cooled to room temperature, and any residual solids were removed by centrifugation. The NPLs were purified by washing with ethanol one time and redispersing in 100 µL MCH. This completed one monolayer of zinc sulfide. Additional monolayers were grown by repeating the same procedure. Oleylamine and ODE were dried at 100°C for two hours under vacuum and transferred to a nitrogen filled glovebox. All steps were performed in a nitrogen glovebox.

Spectroscopic Methods. Static absorption spectra of the NPLs were collected in 2 mm quartz cuvettes using a Cary-50 spectrophotometer. Ultrafast experiments were performed using a Ti:sapphire amplifier with 2 kHz repetition rate and 35 fs pulse width. Pump pulses at were generated by frequency-dividing the 800 nm laser output using an optical parametric amplifier (OPA). A small portion of the 800 nm Ti:sapphire output was focused into a sapphire crystal to produce white light probe pulses. Probe pulses were mechanically time delayed using a translation stage and retroflector and circularly polarized using an achromatic quarter waveplate. Pump pulses were co- and cross-polarized relative to probe pulses using quarter waveplates and selected for every other pulse using a chopper. Additional measurements utilized a photoelastic modulator (electro-optic) operating at 2 kV to shorten collection time and improve data quality. Transient absorption spectra for each time point were averaged over 2 s, and three reproducible, separate scans were then averaged together. Background subtraction and probe chirp correction were conducted for all raw spectra before data analysis. Transient Faraday rotation measurements were performed using permanent magnetic fields that were applied perpendicular to the probe propagation direction. Field strengths at the sample position were evaluated with a Hall probe. All spectroscopic studies were performed at room temperature and in ambient conditions unless otherwise noted.

B.2 Supplementary Data

Table B. 1. Lifetimes of spin depolarization in 2, 3, 4, 5, 6 monolayer CdSe nanoplatelets from single-exponential fitting of spin decay.

*ML*CdSe	τ (ps)	τ amplitude
2CdSe	1.17 ± 0.11	0.86
3CdSe	0.24 ± 0.01	1.04
4CdSe	0.71 ± 0.02	0.90
5CdSe	1.14 ± 0.06	0.84
6CdSe	1.76 ± 0.12	0.81

Table B. 2. Lifetimes of spin depolarization in 5CdSe/*X*CdS core/shell samples with *X*=1, 3, 6 monolayer CdS from biexponential fitting of spin decay.

5CdSe/*X*CdS	τ_1 (ps)	τ_1 amplitude	τ_2 (ps)	τ_2 amplitude
5CdSe	1.30 ± 0.05	0.93	11.24 ± 2.46	0.09
5CdSe/1CdS	1.40 ± 0.21	0.35	24.0 ± 1.3	0.60
5CdSe/3CdS	1.20 ± 0.06	0.39	45.1 ± 1.5	0.57
5CdSe/6CdS	1.09 ± 0.09	0.39	48.6 ± 1.5	0.58

Table B. 3. Lifetimes of spin depolarization in 5CdSe/*X*ZnS core/shell samples with *X*=1, 3 monolayer ZnS from biexponential fitting of spin decay for larger amplitude components.

5CdSe/*X*ZnS	τ_1 (ps)	τ_1 amplitude	τ_2 (ps)	τ_2 amplitude
5CdSe	1.30 ± 0.05	0.93	11.24 ± 2.46	0.09
5CdSe/1ZnS	2.5 ± 0.03	0.54	100.3 ± 3.8	0.31
5CdSe/3ZnS	1.03 ± 0.05	0.96	21.4± 1.07	0.34

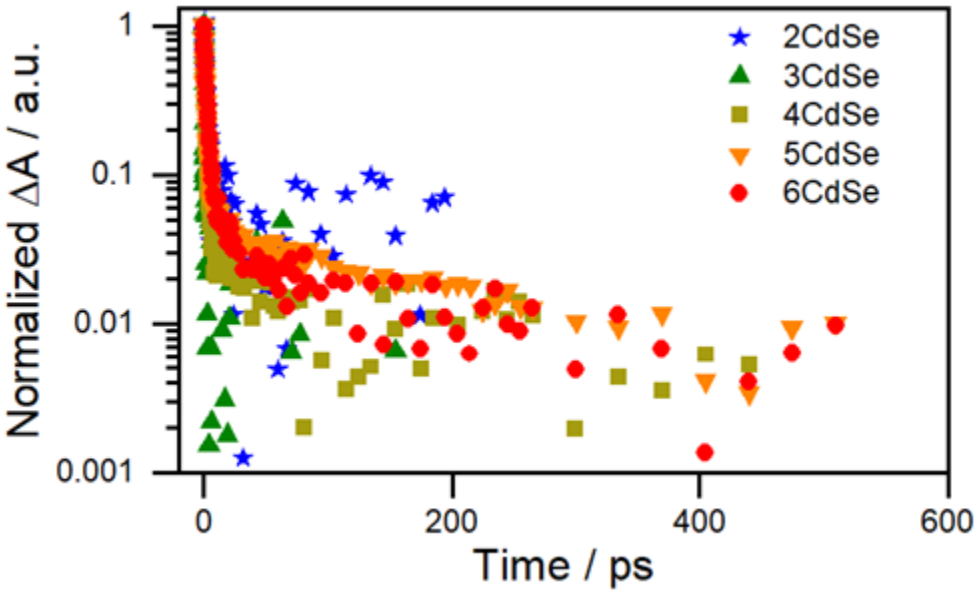

Figure B. 1. Dynamics of complete spin decay for indicated core-only CdSe samples.
Ranging from 2CdSe to 6CdSe. The 2CdSe sample exhibits increased noise compared to other samples owing to the bluer probe wavelength.

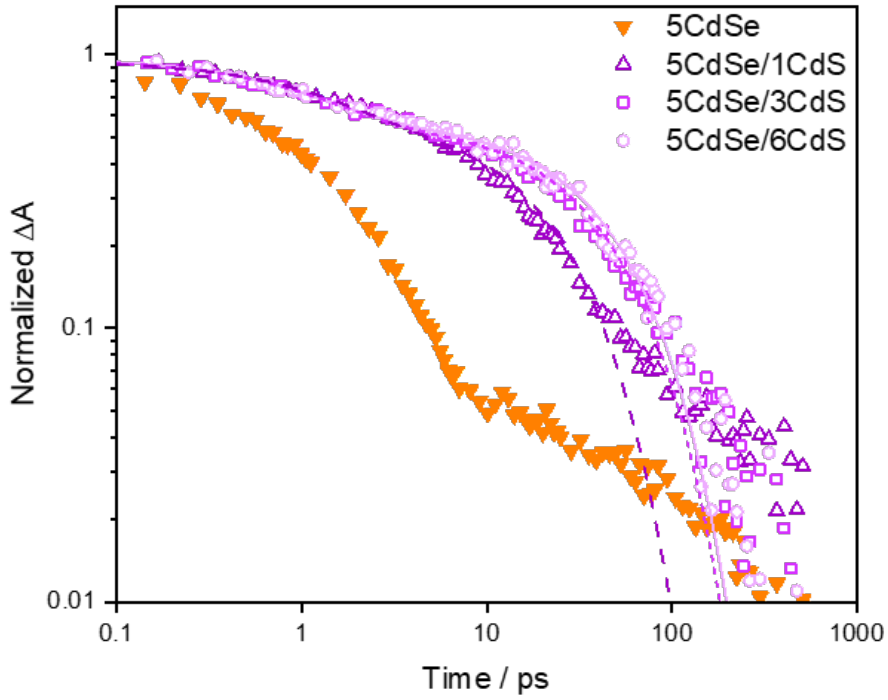

Figure B. 2. Spin depolarization for 5CdSe/*X*CdS samples.
Biexponential fits, color coordinated with the data points shown that are reflected in Table B. 2 above.

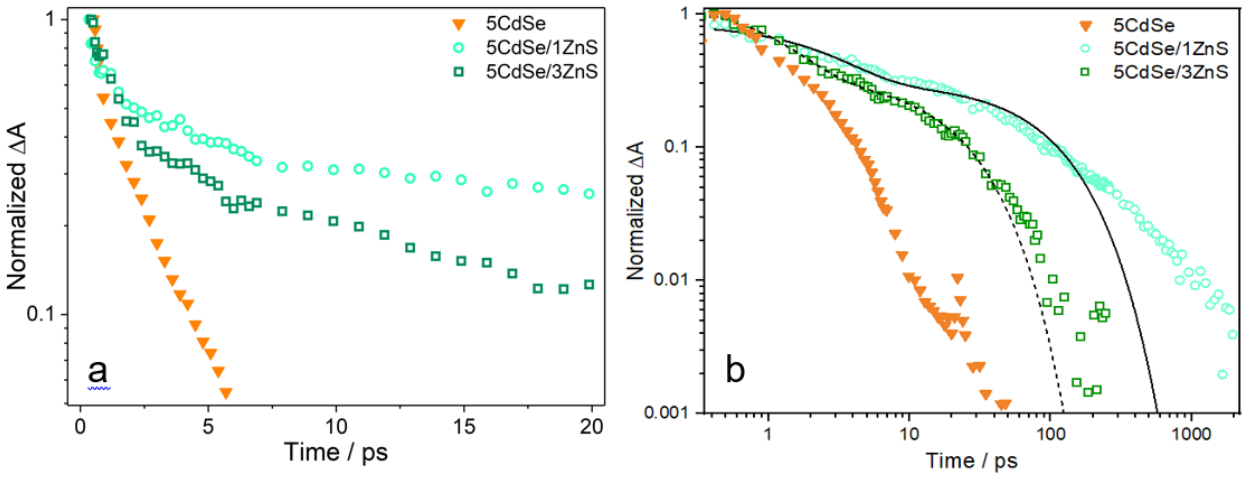

Figure B. 3. Spin depolarization for 5CdSe/*X*ZnS samples.
a) Dynamics at early times show significant increase in lifetimes of spin-coherence in core/shell samples as compared to the core-only sample. b) Logarithmic scaling of kinetic traces highlights the significantly increased decay lifetime of the 5CdSe/1ZnS sample relative to both the 5CdSe core and 5CdSe/3ZnS sample by roughly an order of magnitude. Solid and dashed lines show biexponential fits with parameters that are presented in Table B. 3 above.

Appendix C: Supplementary Information for Chapter 4.

Reprinted with permission from "Shobhana Panuganti, Shelby A. Cuthriell, Ariel A. Leonard, Michael A. Quintero, Craig C. Laing, Burak Guzelturk, Xioyi Zhang, Lin X. Chen, Mercouri G. Kanatzidis, and Richard D. Schaller. *ACS Energy Lett.* **2023** *8* (1)*,* 691-698."

C.1 Experimental Methods

Chemicals. Hydroiodic acid (57 wt %) 99.95%, hypophosphorous acid (50 wt %), dimethyl formamide (anhydrous), chlorobenzene, polymethyl methacrylate, lead (II) oxide powder ≥ 99% trace metals basis, and methylamine hydrochloride ≥ 98% were all purchased from Sigma Aldrich. Ethyl ether (anhydrous) was purchased from Fisher Scientific. Methylamine hydrochloride was dried in an oven at 70ºC overnight before use. All other chemicals were used as received without further purification.

$MAPbI_3$ crystal synthesis. A 50 mL Erlenmeyer flask was dried overnight at 110°C was charged with PbO powder (2232 mg, 10 mmol) and methylamine hydrochloride (676 mg, 10 mmol). Subsequently, 20 mL of hydroiodic acid and 2 mL of hypophosphorous acid were added to the flask while heating and stirring to afford a bright yellow solution. The flask was removed from heat and allowed to cool to room temperature. Small, black crystals precipitated out of solution upon cooling and were isolated from the reaction mixture through vacuum filtration over a medium-porosity fritted glass filter. The crystals were triple washed with diethyl ether and stored in an evacuated desiccator for at least 24 hours before further use.

$MAPbI_3$ thin film fabrication. Single-crystal sapphire and fused quartz glass substrates (Ø25.4 mm × 1.6 mm) were cleaned in a sonicated bath using first soapy water, then deionized water, and finally acetone for ten minutes each. These washes were followed by 30 minutes of ultraviolet-ozone (UVO) treatment. The substrates and previously synthesized $MAPbI_3$ crystals were then transferred into a nitrogen atmosphere for the remainder of processing. A precursor solution was prepared by first dissolving the $MAPbI_3$ crystals (200 mg, 0.323 mmol) in 1 mL of dimethyl formamide and then syringe filtering through 0.2 µm-pore polytetrafluoroethylene (PTFE) membrane. Films were synthesized by spin-coating 80 µL of the precursor solution onto the substrates at 1000 rpm for 30 seconds and then annealing at 110°C for 5 minutes. The films were then coated in a concentrated solution of polymethyl methacrylate in chlorobenzene and annealed at 110°C for 5 minutes. The resulting films were stored in the dark under nitrogen until use.

Time-Resolved X-ray Diffraction. TR-XRD experiments were conducted using synchrotron radiation at beamline 11-ID-D of the Advanced Photon Source (APS), Argonne National Laboratory. Laser pulses were generated using the frequency-doubled output from a Ti:sapphire regeneratively amplified laser with 10 kHz repetition rate, producing 3.1 eV (400 nm) incident pump energy with 1.2 ps pulse width and spot size of 1200 × 6900 µm (area = 0.06557 cm^{-2}). Laser fluence at the sample was adjusted using neutral density filters, and time delays were mechanically created using a translation stage and retroflector. The X-ray probe beam was diverted using two inline undulators from the APS storage ring in 24-bunch mode to provide 11.57 keV (λ

= 1.05969 Å) probe pulses at 6.5 MHz repetition rate with 79 ps pulse width. The laser pump and X-ray probe were orthogonally overlapped onto the surface of the spinning film, which was tilted at an angle of 4° to the incident X-rays. The Pilatus 2M detector was placed ~202 mm from the sample and temporally gated to measure scattering intensity only at the laser-synchronized probe pulses. Detector image plates were collected and integrated over twenty seconds of exposure time. The subsequent scattering intensity was azimuthally integrated to produce diffraction patterns and then averaged over six cycles for each time delay. Image plate pixel values were calibrated to Q /$Å^{-1}$ using the azimuthally integrated diffraction pattern of a CeO_2 standard.

C.2 Data Processing

Area detector plate images were azimuthally integrated to generate powder diffraction patterns as a function of Q/Å^{-1}. Integrated PXRD patterns were normalized to account for variations in scattering intensity and fluctuations in synchrotron X-ray flux using the average scattering intensity in a region of the baseline where Bragg reflections are completely absent (between Q = 0.2032 Å^{-1} to 0.8032 Å^{-1}).

At each time delay post-photoexcitation, a PXRD pattern of the sample film collected prior to photoexcitation, I_0 (t = -5 ns), was subtracted from the photoexcited pattern I (t > 0 ns) to obtain a differenced, transient diffraction pattern as follows:

$$\Delta I\,(t) = I\,(t) \; - \; I_0$$

This was repeated for each individual time point. In this way, we were able to account for minor sample degradation and fluctuations in ambient lab conditions, such as temperature and humidity, by collecting reference steady-state patterns frequently (every four "transient" time points) and comparing transients to the reference pattern collected closest in time over the course of the experiment.

In our analysis, we examined the averaged responses for each film considering:

1. photon absorption in the films at the utilized pump wavelength is not impacted by strain
2. films are rapidly spun
3. each sample film was measured over multiple cycles and averaged over many seconds of exposure time
4. powder patterns are collected on a 2D area detector and then integrated n, meaning we observe a continuum of grain orientation
5. multiple spots on multiple sample films were sampled to ensure reproducibility of results

All TR-XRD patterns shown in this work present smoothed data using the `smoothdata` function in MATLAB R2021b. Data was smoothed every two points (~0.001 Å^{-1}) using locally-weighted quadratic regression method. All integrals calculated in this work were done so using the `trapz` function in MATLAB R2021b, which uses trapezoidal Riemann sums between adjacent data points to estimate integrals. Transient patterns at different fluences were indexed using the aid of GSASII[171]. The maxima of the positive lobes of the transient patterns were used as inputs for indexing.

C.3 Temperature Estimations

Temperature estimations as described in the text necessitated a defined photoexcited volume V which was estimated as the experimental pump spot area with a pump penetration depth based on the previously reported value of the absorption coefficient ($\alpha = 1.4 \cdot 10^5\ cm^{-1}$) for 3.1 eV photons in $MAPbI_3$ thin films.[122] The estimated change in temperature was then calculated according to the following equation:

$$\Delta T = \frac{n \cdot E}{V \cdot C_V}$$

where n is the total number of photons per pump pulse, E is the thermal energy per photon, and C_V is the experimental volumetric heat capacity at 298 K as reported.[151] As noted in the main text, maximum temperature estimations ΔT_{max} assumed all pump energy became available thermal energy (E = 3.1 eV) while minimum temperatures ΔT_{min} were calculated under the assumption that only pump photon energy in excess of the band gap absorption (E = 1.55 eV) was dissipated as thermal energy. In the extreme scenario of complete thermalization, the maximum possible thermal energy is considered to be deposited; thus, in the real material even thermal inhomogeneities likely cannot access temperatures that can induce the known thermodynamic phase transition.

Table C. 1. Minimum and maximum temperature estimations of the photoexcited volume V as a function of pump fluence.

Fluence / µJ • cm^{-2}	**ΔT_{min} /K**	**ΔT_{max} /K**
1.5	0.066	0.140
3	0.148	0.318
10	0.523	1.12
26	1.27	2.81
72	3.50	7.48
323	15.7	33.7
413	20.1	43.0

C.4 Additional Data

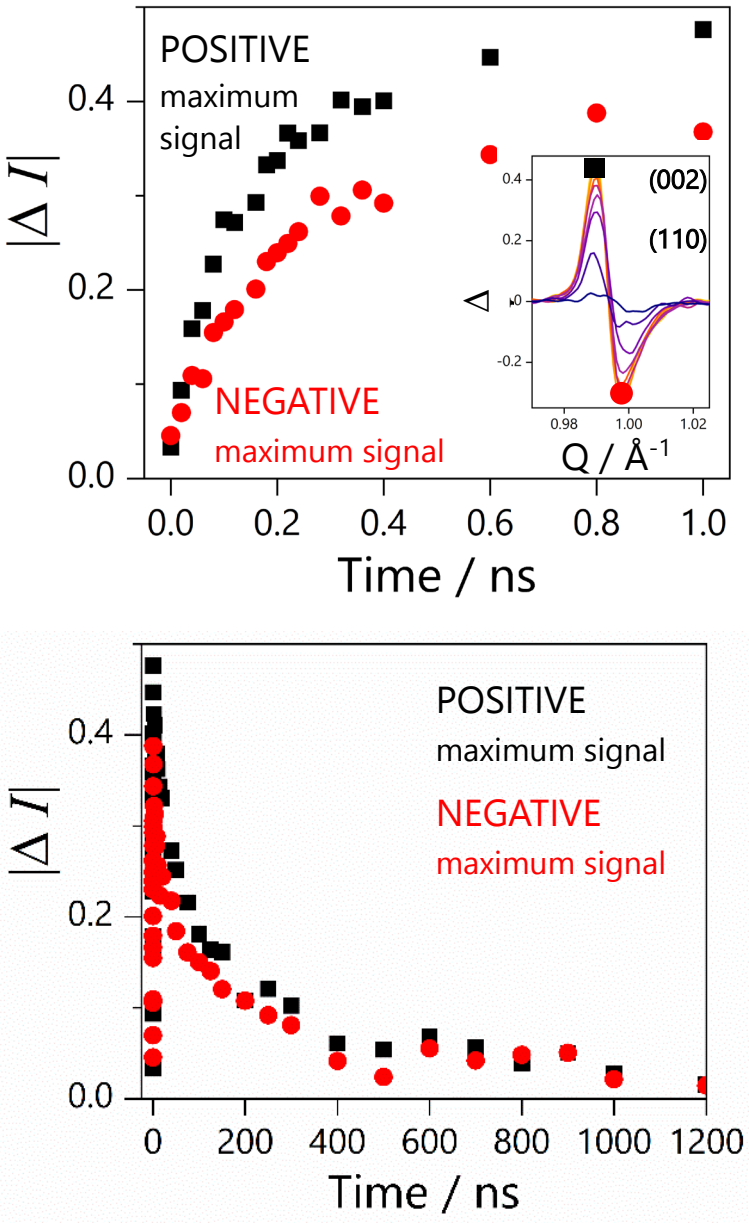

Figure C. 1. Absolute values of maximum change in signal intensity ($|\Delta I|$) over time. **(a)** 0 to 1 ns and **(b)** 0 to 1200 ns for the positive (black, square) and negative (red, circle) signals centered around Q = 0.99 Å^{-1} and indexed to the (002) and (110) Bragg reflection of the tetragonal phase of $MAPbI_3$. Maximum signal intensities are similar until ~60 ps, at which point the positive signal quickly outgrows the negative signal and persists as such until ~600 ns.

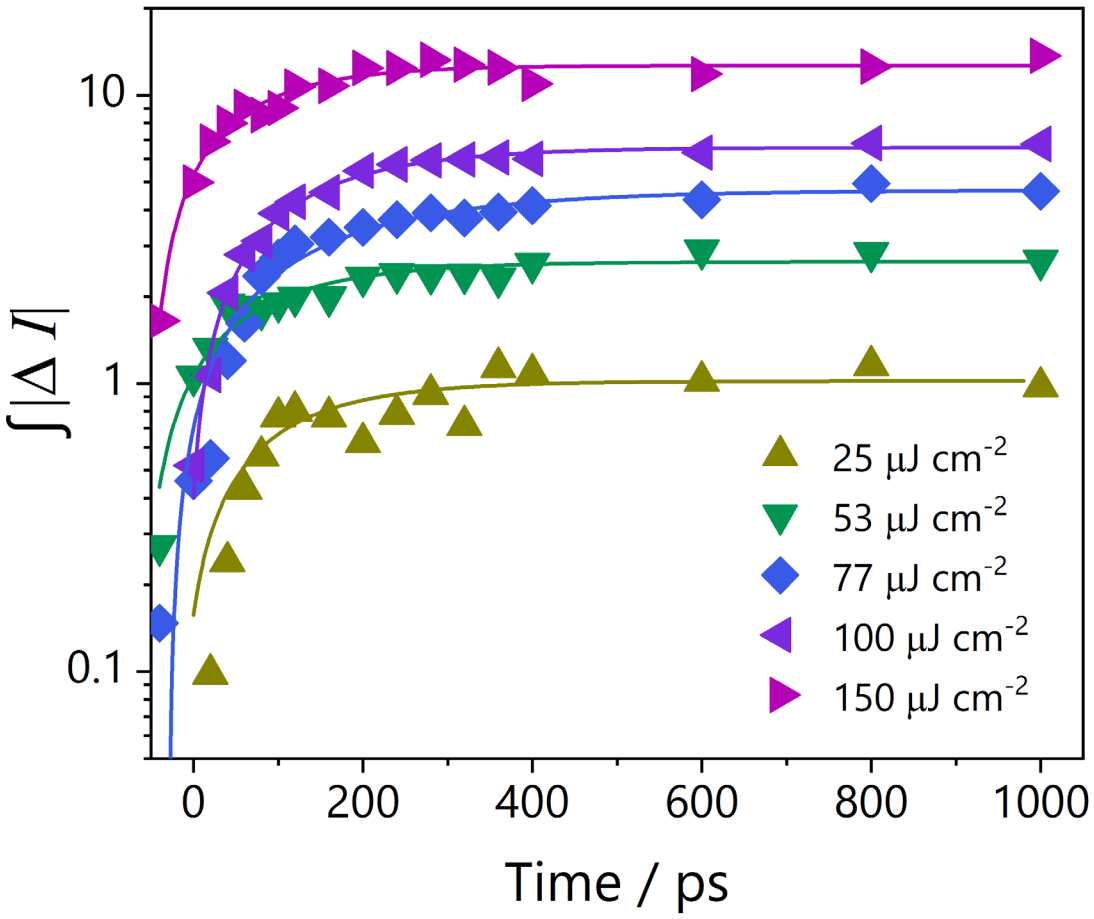

Figure C. 2. Normalized integrated absolute values of the peak area ($\int|\Delta I|$) of the (211) reflection. At Q = 1.66 Å^{-1} as a function of pump-probe delay time 0 to 1 ns and following photoexcitation. Exponential fitting of $\int|\Delta I|$ with respect to time revealed a "rise" lifetime of τ_{211} = 144 ± 20 ps, averaged over all shown fluences, for the initial decrease of the (211) reflection. Similar processing was used in the fitting of other selected peaks shown in the main text.

References

(1) *World Energy Pulse 2023*; World Energy Council, London, United Kingdom, 2023.

(2) Lee, H. R., Jose. Climate Change 2023: Synthesis Report. A Report of the Intergovernmental Panel on Climate Change. Contribution of Working Groups I, II and III to the Sixth Assessment Report of the Intergovernmental Panel on Climate Change. IPCC: Geneva, Switzerland, 2023; p 36.

(3) Lewis, N. S.; Nocera, D. G. Powering the planet: Chemical challenges in solar energy utilization. *Proceedings of the National Academy of Sciences* **2006**, *103* (43), 15729-15735.

(4) Turner, J. A. A Realizable Renewable Energy Future. *Science* **1999**, *285* (5428), 687-689.

(5) *bp Statistical Review of World Energy 2022*; London, 2022.

(6) Hadar, I.; Song, T.-B.; Ke, W.; Kanatzidis, M. G. Modern Processing and Insights on Selenium Solar Cells: The World's First Photovoltaic Device. *Advanced Energy Materials* **2019**, *9* (16), 1802766.

(7) Goetzberger, A.; Luther, J.; Willeke, G. Solar cells: past, present, future. *Solar Energy Materials and Solar Cells* **2002**, *74* (1), 1-11.

(8) Sun, Z.; Chen, X.; He, Y.; Li, J.; Wang, J.; Yan, H.; Zhang, Y. Toward Efficiency Limits of Crystalline Silicon Solar Cells: Recent Progress in High-Efficiency Silicon Heterojunction Solar Cells. *Advanced Energy Materials* **2022**, *12* (23), 2200015.

(9) Smith, M. D.; Crace, E. J.; Jaffe, A.; Karunadasa, H. I. The Diversity of Layered Halide Perovskites. *Annual Review of Materials Research* **2018**, *48* (1), 111-136.

(10) Park, J.; Kim, J.; Yun, H.-S.; Paik, M. J.; Noh, E.; Mun, H. J.; Kim, M. G.; Shin, T. J.; Seok, S. I. Controlled growth of perovskite layers with volatile alkylammonium chlorides. *Nature* **2023**, *616* (7958), 724-730.

(11) Kojima, A.; Teshima, K.; Shirai, Y.; Miyasaka, T. Organometal Halide Perovskites as Visible-Light Sensitizers for Photovoltaic Cells. *Journal of the American Chemical Society* **2009**, *131* (17), 6050-6051.

(12) Bloch, F. Über die Quantenmechanik der Elektronen in Kristallgittern. *Zeitschrift für Physik* **1929**, *52* (7), 555-600.

(13) Smith, M. D.; Connor, B. A.; Karunadasa, H. I. Tuning the Luminescence of Layered Halide Perovskites. *Chemical Reviews* **2019**, *119* (5), 3104-3139.

(14) Goldschmidt, V. M. Die Gesetze der Krystallochemie. *Naturwissenschaften* **1926**, *14* (21), 477-485.

(15) Bartel, C. J.; Sutton, C.; Goldsmith, B. R.; Ouyang, R.; Musgrave, C. B.; Ghiringhelli, L. M.; Scheffler, M. New tolerance factor to predict the stability of perovskite oxides and halides. *Science Advances* **2019**, *5* (2), eaav0693.

(16) Brus, L. Zero-dimensional "excitons" in semiconductor clusters. *IEEE Journal of Quantum Electronics* **1986**, *22* (9), 1909-1914.

(17) Murray, C. B.; Norris, D. J.; Bawendi, M. G. Synthesis and characterization of nearly monodisperse CdE (E = sulfur, selenium, tellurium) semiconductor nanocrystallites. *Journal of the American Chemical Society* **1993**, *115* (19), 8706-8715.

(18) Klimov, V. I. Mechanisms for Photogeneration and Recombination of Multiexcitons in Semiconductor Nanocrystals: Implications for Lasing and Solar Energy Conversion. *The Journal of Physical Chemistry B* **2006**, *110* (34), 16827-16845.

(19) Blancon, J. C.; Stier, A. V.; Tsai, H.; Nie, W.; Stoumpos, C. C.; Traoré, B.; Pedesseau, L.; Kepenekian, M.; Katsutani, F.; Noe, G. T.; et al. Scaling law for excitons in 2D perovskite quantum wells. *Nat. Commun.* **2018**, *9* (1), 2254.

(20) Brumberg, A.; Harvey, S. M.; Philbin, J. P.; Diroll, B. T.; Lee, B.; Crooker, S. A.; Wasielewski, M. R.; Rabani, E.; Schaller, R. D. Determination of the in-plane exciton radius in 2D CdSe nanoplatelets via magneto-optical spectroscopy. *ACS Nano* **2019**, *13* (8), 8589.

(21) Acharya, R.; Challita, E. J.; Ilton, M.; Saad Bhamla, M. The ultrafast snap of a finger is mediated by skin friction. *Journal of The Royal Society Interface* **2021**, *18* (184), 20210672.

(22) Strickland, D.; Mourou, G. Compression of amplified chirped optical pulses. *Optics Communications* **1985**, *55* (6), 447-449.

(23) Lee, M. M.; Teuscher, J.; Miyasaka, T.; Murakami, T. N.; Snaith, H. J. Efficient Hybrid Solar Cells Based on Meso-Superstructured Organometal Halide Perovskites. *Science* **2012**, *338* (6107), 643.

(24) Heo, J. H.; Im, S. H.; Noh, J. H.; Mandal, T. N.; Lim, C.-S.; Chang, J. A.; Lee, Y. H.; Kim, H.-j.; Sarkar, A.; Nazeeruddin, M. K.; et al. Efficient inorganic–organic hybrid heterojunction solar cells containing perovskite compound and polymeric hole conductors. *Nature Photonics* **2013**, *7* (6), 486-491.

(25) Baikie, T.; Fang, Y.; Kadro, J. M.; Schreyer, M.; Wei, F.; Mhaisalkar, S. G.; Graetzel, M.; White, T. J. Synthesis and crystal chemistry of the hybrid perovskite (CH3NH3)PbI3 for solid-state sensitised solar cell applications. *Journal of Materials Chemistry A* **2013**, *1* (18), 5628-5641.

(26) Fieramosca, A.; Polimeno, L.; Ardizzone, V.; De Marco, L.; Pugliese, M.; Maiorano, V.; De Giorgi, M.; Dominici, L.; Gigli, G.; Gerace, D.; et al. Two-dimensional hybrid perovskites sustaining strong polariton interactions at room temperature. *Science Advances* **2019**, *5* (5), eaav9967.

(27) Guzelturk, B.; Kelestemur, Y.; Olutas, M.; Delikanli, S.; Demir, H. V. Amplified Spontaneous Emission and Lasing in Colloidal Nanoplatelets. *ACS Nano* **2014**, *8* (7), 6599-6605.

(28) Zhao, C.; Tian, W.; Liu, J.; Sun, Q.; Luo, J.; Yuan, H.; Gai, B.; Tang, J.; Guo, J.; Jin, S. Stable Two-Photon Pumped Amplified Spontaneous Emission from Millimeter-Sized CsPbBr3 Single Crystals. *The Journal of Physical Chemistry Letters* **2019**, *10* (10), 2357-2362.

(29) Sigle, D. O.; Zhang, L.; Ithurria, S.; Dubertret, B.; Baumberg, J. J. Ultrathin CdSe in Plasmonic Nanogaps for Enhanced Photocatalytic Water Splitting. *The Journal of Physical Chemistry Letters* **2015**, *6* (7), 1099-1103.

(30) Chauhan, H.; Kumar, Y.; Dana, J.; Satpati, B.; Ghosh, H. N.; Deka, S. Photoinduced ultrafast charge separation in colloidal 2-dimensional CdSe/CdS-Au hybrid nanoplatelets and corresponding application in photocatalysis. *Nanoscale* **2016**, *8* (34), 15802-15812.

(31) Peng, W.; Li, Y.; Zhang, F.; Zhang, G.; Fan, X. Roles of Two-Dimensional Transition Metal Dichalcogenides as Cocatalysts in Photocatalytic Hydrogen Evolution and Environmental Remediation. *Industrial & Engineering Chemistry Research* **2017**, *56* (16), 4611-4626.

(32) Kumar, S.; Jagielski, J.; Yakunin, S.; Rice, P.; Chiu, Y.-C.; Wang, M.; Nedelcu, G.; Kim, Y.; Lin, S.; Santos, E. J. G.; et al. Efficient Blue Electroluminescence Using Quantum-Confined Two-Dimensional Perovskites. *ACS Nano* **2016**, *10* (10), 9720-9729.

(33) Hattori, T.; Taira, T.; Era, M.; Tsutsui, T.; Saito, S. Highly efficient electroluminescence from a heterostructure device combined with emissive layered-perovskite and an electron-transporting organic compound. *Chemical Physics Letters* **1996**, *254* (1), 103-108.

(34) Papavassiliou, G. C.; Koutselas, I. B.; Terzis, A.; Whangbo, M. H. Structural and electronic properties of the natural quantum-well system (C6H5CH2CH2NH3)2SnI4. *Solid State Communications* **1994**, *91* (9), 695-698.

(35) Hong, X.; Ishihara, T.; Nurmikko, A. V. Dielectric confinement effect on excitons in ${\mathrm{PbI}}_{4}$-based layered semiconductors. *Physical Review B* **1992**, *45* (12), 6961-6964.

(36) Mitzi, D. B.; Wang, S.; Feild, C. A.; Chess, C. A.; Guloy, A. M. Conducting Layered Organic-inorganic Halides Containing <110>-Oriented Perovskite Sheets. *Science* **1995**, *267* (5203), 1473.

(37) Hartono, N. T. P.; Sun, S.; Gélvez-Rueda, M. C.; Pierone, P. J.; Erodici, M. P.; Yoo, J.; Wei, F.; Bawendi, M.; Grozema, F. C.; Sher, M.-j.; et al. The effect of structural dimensionality on carrier mobility in lead-halide perovskites. *Journal of Materials Chemistry A* **2019**, *7* (41), 23949-23957.

(38) Wang, L.; Huang, L.; Tan, W. C.; Feng, X.; Chen, L.; Huang, X.; Ang, K.-W. 2D Photovoltaic Devices: Progress and Prospects. *Small Methods* **2018**, *2* (3), 1700294.

(39) Motti, S. G.; Crothers, T.; Yang, R.; Cao, Y.; Li, R.; Johnston, M. B.; Wang, J.; Herz, L. M. Heterogeneous Photon Recycling and Charge Diffusion Enhance Charge Transport in Quasi-2D Lead-Halide Perovskite Films. *Nano Letters* **2019**, *19* (6), 3953-3960.

(40) Santra, P. K.; Kamat, P. V. Tandem-Layered Quantum Dot Solar Cells: Tuning the Photovoltaic Response with Luminescent Ternary Cadmium Chalcogenides. *Journal of the American Chemical Society* **2013**, *135* (2), 877-885.

(41) Quan, L. N.; Zhao, Y.; García de Arquer, F. P.; Sabatini, R.; Walters, G.; Voznyy, O.; Comin, R.; Li, Y.; Fan, J. Z.; Tan, H.; et al. Tailoring the Energy Landscape in Quasi-2D Halide Perovskites Enables Efficient Green-Light Emission. *Nano Letters* **2017**, *17* (6), 3701-3709.

(42) Hoffman, J. B.; Alam, R.; Kamat, P. V. Why Surface Chemistry Matters for QD–QD Resonance Energy Transfer. *ACS Energy Letters* **2017**, *2* (2), 391-396.

(43) Patel, M.; Pataniya, P.; Vala, H.; Sumesh, C. K. One-Dimensional/Two-Dimensional/Three-Dimensional Dual Heterostructure Based on MoS2-Modified ZnO-Heterojunction Diode with Silicon. *The Journal of Physical Chemistry C* **2019**, *123* (36), 21941-21949.

(44) Yuan, M.; Quan, L. N.; Comin, R.; Walters, G.; Sabatini, R.; Voznyy, O.; Hoogland, S.; Zhao, Y.; Beauregard, E. M.; Kanjanaboos, P.; et al. Perovskite energy funnels for efficient light-emitting diodes. *Nature Nanotechnology* **2016**, *11* (10), 872-877.

(45) Xia, F.; Wang, H.; Xiao, D.; Dubey, M.; Ramasubramaniam, A. Two-dimensional material nanophotonics. *Nat. Photonics* **2014**, *8* (12), 899.

(46) Tsai, H.; Nie, W.; Blancon, J.-C.; Stoumpos, C. C.; Asadpour, R.; Harutyunyan, B.; Neukirch, A. J.; Verduzco, R.; Crochet, J. J.; Tretiak, S.; et al. High-efficiency two-dimensional Ruddlesden–Popper perovskite solar cells. *Nature* **2016**, *536* (7616), 312-316.

(47) Das, S.; Pandey, D.; Thomas, J.; Roy, T. The Role of Graphene and Other 2D Materials in Solar Photovoltaics. *Advanced Materials* **2019**, *31* (1), 1802722.

(48) Yu, X.; Sivula, K. Toward Large-Area Solar Energy Conversion with Semiconducting 2D Transition Metal Dichalcogenides. *ACS Energy Letters* **2016**, *1* (1), 315-322.

(49) Kumar, S.; Jagielski, J.; Yakunin, S.; Rice, P.; Chiu, Y. C.; Wang, M.; Nedelcu, G.; Kim, Y.; Lin, S.; Santos, E. J. G.; et al. Efficient Blue Electroluminescence Using Quantum-Confined Two-Dimensional Perovskites. *ACS Nano* **2016**, *10* (10), 9720.

(50) Chen, Z.; Nadal, B.; Mahler, B.; Aubin, H.; Dubertret, B. Quasi-2D Colloidal Semiconductor Nanoplatelets for Narrow Electroluminescence. *Adv. Funct. Mater.* **2014**, *24* (3), 295.

(51) Ithurria, S.; Tessier, M. D.; Mahler, B.; Lobo, R. P. S. M.; Dubertret, B.; Efros, A. L. Colloidal nanoplatelets with two-dimensional electronic structure. *Nat. Mater.* **2011**, *10* (12), 936.

(52) Guzelturk, B.; Demir, H. V. Near-Field Energy Transfer Using Nanoemitters For Optoelectronics. *Advanced Functional Materials* **2016**, *26* (45), 8158-8177.

(53) Padgaonkar, S.; Olding, J. N.; Lauhon, L. J.; Hersam, M. C.; Weiss, E. A. Emergent Optoelectronic Properties of Mixed-Dimensional Heterojunctions. *Accounts of Chemical Research* **2020**, *53* (4), 763-772.

(54) Menke, S. M.; Luhman, W. A.; Holmes, R. J. Tailored exciton diffusion in organic photovoltaic cells for enhanced power conversion efficiency. *Nat. Mater.* **2013**, *12* (2), 152.

(55) Förster, T.; Mielczarek, E. V.; Greenbaum, E.; Knox, R. S. *Biological Physics*; 1993.

(56) Hernández-Martínez, P. L.; Govorov, A. O.; Demir, H. V. Generalized Theory of Förster-Type Nonradiative Energy Transfer in Nanostructures with Mixed Dimensionality. *J. Phys. Chem. C* **2013**, *117* (19), 10203.

(57) Liu, X.; Qiu, J. Recent advances in energy transfer in bulk and nanoscale luminescent materials: from spectroscopy to applications. *Chem. Soc. Rev.* **2015**, *44* (23), 8714.

(58) Loiudice, A.; Saris, S.; Buonsanti, R. Tunable Metal Oxide Shell as a Spacer to Study Energy Transfer in Semiconductor Nanocrystals. *J. Phys. Chem. Lett.* **2020**, *11*, 3430.

(59) Erdem, O.; Gungor, K.; Guzelturk, B.; Tanriover, I.; Sak, M.; Olutas, M.; Dede, D.; Kelestemur, Y.; Demir, H. V. Orientation-Controlled Nonradiative Energy Transfer to Colloidal Nanoplatelets: Engineering Dipole Orientation Factor. *Nano Lett.* **2019**, *19* (7), 4297.

(60) Rowland, C. E.; Fedin, I.; Zhang, H.; Gray, S. K.; Govorov, A. O.; Talapin, D. V.; Schaller, R. D. Picosecond energy transfer and multiexciton transfer outpaces Auger recombination in binary CdSe nanoplatelet solids. *Nat. Mater.* **2015**, *14*, 484.

(61) Liu, H.; Wang, T.; Wang, C.; Liu, D.; Luo, J. Exciton Radiative Recombination Dynamics and Nonradiative Energy Transfer in Two-Dimensional Transition-Metal Dichalcogenides. *J. Phys. Chem. C* **2019**, *123* (15), 10087.

(62) Taghipour, N.; Hernandez Martinez, P. L.; Ozden, A.; Olutas, M.; Dede, D.; Gungor, K.; Erdem, O.; Perkgoz, N. K.; Demir, H. V. Near-Unity Efficiency Energy Transfer from Colloidal Semiconductor Quantum Wells of CdSe/CdS Nanoplatelets to a Monolayer of MoS2. *ACS Nano* **2018**, *12* (8), 8547.

(63) Raja, A.; Montoya-Castillo, A.; Zultak, J.; Zhang, X. X.; Ye, Z.; Roquelet, C.; Chenet, D. A.; van der Zande, A. M.; Huang, P.; Jockusch, S.; et al. Energy Transfer from Quantum Dots to Graphene and MoS2: The Role of Absorption and Screening in Two-Dimensional Materials. *Nano Lett.* **2016**, *16* (4), 2328.

(64) Prins, F.; Goodman, A. J.; Tisdale, W. A. Reduced Dielectric Screening and Enhanced Energy Transfer in Single- and Few-Layer MoS2. *Nano Lett.* **2014**, *14* (11), 6087.

(65) Ajayi, O. A.; Anderson, N. C.; Cotlet, M.; Petrone, N.; Gu, T.; Wolcott, A.; Gesuele, F.; Hone, J.; Owen, J. S.; Wong, C. W. Time-resolved energy transfer from single chloride-terminated nanocrystals to graphene. *Appl. Phys. Lett.* **2014**, *104* (17), 171101.

(66) Gaudreau, L.; Tielrooij, K. J.; Prawiroatmodjo, G. E. D. K.; Osmond, J.; de Abajo, F. J. G.; Koppens, F. H. L. Universal Distance-Scaling of Nonradiative Energy Transfer to Graphene. *Nano Lett.* **2013**, *13* (5), 2030.

(67) Swathi, R. S.; Sebastian, K. L. Resonance energy transfer from a dye molecule to graphene. *J. Chem. Phys.* **2008**, *129* (5), 054703.

(68) Hong, X.; Ishihara, T.; Nurmikko, A. V. Dielectric confinement effect on excitons in PbI4-based layered semiconductors. *Phys. Rev. B: Condens. Matter Mater. Phys.* **1992**, *45* (12), 6961.

(69) Lei, L.; Seyitliyev, D.; Stuard, S.; Mendes, J.; Dong, Q.; Fu, X.; Chen, Y. A.; He, S.; Yi, X.; Zhu, L.; et al. So, F., Efficient Energy Funneling in Quasi-2D Perovskites: From Light Emission to Lasing. *Adv. Mater.* **2020**, *32* (16), 1906571.

(70) Zheng, K.; Chen, Y.; Sun, Y.; Chen, J.; Chábera, P.; Schaller, R.; Al-Marri, M. J.; Canton, S. E.; Liang, Z.; Pullerits, T. Inter-phase charge and energy transfer in Ruddlesden–Popper 2D perovskites: critical role of the spacing cations. *J. Mater. Chem. A* **2018**, *6* (15), 6244.

(71) Williams, O. F.; Guo, Z.; Hu, J.; Yan, L.; You, W.; Moran, A. M. Energy transfer mechanisms in layered 2D perovskites. *J. Chem. Phys.* **2018**, *148* (13), 134706.

(72) Proppe, A. H.; Elkins, M. H.; Voznyy, O.; Pensack, R. D.; Zapata, F.; Besteiro, L. V.; Quan, L. N.; Quintero-Bermudez, R.; Todorovic, P.; Kelley, S. O.; et al. Spectrally Resolved Ultrafast Exciton Transfer in Mixed Perovskite Quantum Wells. *J. Phys. Chem. Lett.* **2019**, *10* (3), 419.

(73) Singldinger, A.; Gramlich, M.; Gruber, C.; Lampe, C.; Urban, A. S. Nonradiative Energy Transfer between Thickness-Controlled Halide Perovskite Nanoplatelets. *ACS Energy Letters* **2020**, *5* (5), 1380.

(74) Peng, S.; Wei, Q.; Wang, B.; Zhang, Z.; Yang, H.; Pang, G.; Wang, K.; Xing, G.; Sun, X. W.; Tang, Z. Suppressing Strong Exciton–Phonon Coupling in Blue Perovskite Nanoplatelet Solids by Binary Systems. *Angew. Chem., Int. Ed.* **2020**, *59* (49), 22156.

(75) Li, T.; Zeidell, A. M.; Findik, G.; Dunlap-Shohl, W. A.; Euvrard, J.; Gundogdu, K.; Jurchescu, O. D.; Mitzi, D. B. Phase-Pure Hybrid Layered Lead Iodide Perovskite Films Based on a Two-Step Melt-Processing Approach. *Chem. Mater.* **2019**, *31* (11), 4267.

(76) Dahlman, C. J.; DeCrescent, R. A.; Venkatesan, N. R.; Kennard, R. M.; Wu, G.; Everest, M. A.; Schuller, J. A.; Chabinyc, M. L. Controlling Solvate Intermediate Growth for Phase-Pure Organic Lead Iodide Ruddlesden–Popper (C4H9NH3)2(CH3NH3)n–1PbnI3n+1 Perovskite Thin Films. *Chem. Mater.* **2019**, *31* (15), 5832.

(77) Fang, H. H.; Yang, J.; Adjokatse, S.; Tekelenburg, E.; Kamminga, M. E.; Duim, H.; Ye, J.; Blake, G. R.; Even, J.; Loi, M. A. Band-Edge Exciton Fine Structure and Exciton Recombination Dynamics in Single Crystals of Layered Hybrid Perovskites. *Adv. Funct. Mater.* **2020**, *30* (6), 1907979.

(78) Liang, Y.; Shang, Q.; Wei, Q.; Zhao, L.; Liu, Z.; Shi, J.; Zhong, Y.; Chen, J.; Gao, Y.; Li, M.; et al. Lasing from Mechanically Exfoliated 2D Homologous Ruddlesden–Popper Perovskite Engineered by Inorganic Layer Thickness. *Adv. Mater.* **2019**, *31* (39), 1903030.

(79) Spanopoulos, I.; Hadar, I.; Ke, W.; Tu, Q.; Chen, M.; Tsai, H.; He, Y.; Shekhawat, G.; Dravid, V. P.; Wasielewski, M. R.; et al. Uniaxial Expansion of the 2D Ruddlesden–Popper Perovskite Family for Improved Environmental Stability. *J. Am. Chem. Soc.* **2019**, *141* (13), 5518.

(80) Stoumpos, C. C.; Cao, D. H.; Clark, D. J.; Young, J.; Rondinelli, J. M.; Jang, J. I.; Hupp, J. T.; Kanatzidis, M. G. Ruddlesden–Popper Hybrid Lead Iodide Perovskite 2D Homologous Semiconductors. *Chem. Mater.* **2016**, *28* (8), 2852.

(81) Yang, Y.; Yang, M.; Zhu, K.; Johnson, J. C.; Berry, J. J.; van de Lagemaat, J.; Beard, M. C. Large polarization-dependent exciton optical Stark effect in lead iodide perovskites. *Nat. Commun.* **2016**, *7* (1), 12613.

(82) Proppe, A. H.; Walters, G. W.; Alsalloum, A. Y.; Zhumekenov, A. A.; Mosconi, E.; Kelley, S. O.; De Angelis, F.; Adamska, L.; Umari, P.; Bakr, O. M.; et al. Transition Dipole Moments of n = 1, 2, and 3 Perovskite Quantum Wells from the Optical Stark Effect and Many-Body Perturbation Theory. *The Journal of Physical Chemistry Letters* **2020**, *11* (3), 716-723.

(83) Phillips, L. J.; Rashed, A. M.; Treharne, R. E.; Kay, J.; Yates, P.; Mitrovic, I. Z.; Weerakkody, A.; Hall, S.; Durose, K. Dispersion relation data for methylammonium lead triiodide perovskite deposited on a (100) silicon wafer using a two-step vapour-phase reaction process. *Data in Brief* **2015**, *5*, 926.

(84) She, C.; Fedin, I.; Dolzhnikov, D. S.; Dahlberg, P. D.; Engel, G. S.; Schaller, R. D.; Talapin, D. V. Red, yellow, green, and blue amplified spontaneous emission and lasing using colloidal CdSe nanoplatelets. *ACS Nano* **2015**, *9* (10), 9475.

(85) Hazarika, A.; Fedin, I.; Hong, L.; Guo, J.; Srivastava, V.; Cho, W.; Coropceanu, I.; Portner, J.; Diroll, B. T.; Philbin, J. P.; et al. Colloidal atomic layer deposition with stationary reactant phases enables precise synthesis of "digital" II–VI nano-heterostructures with exquisite control of confinement and strain. *J. Am. Chem. Soc.* **2019**, *141* (34), 13487.

(86) Ithurria, S.; Dubertret, B. Quasi 2D colloidal CdSe platelets with thicknesses controlled at the atomic level. *J. Am. Chem. Soc.* **2008**, *130* (49), 16504.

(87) Ithurria, S.; Tessier, M.; Mahler, B.; Lobo, R.; Dubertret, B.; Efros, A. L. Colloidal nanoplatelets with two-dimensional electronic structure. *Nat. Mater.* **2011**, *10* (12), 936.

(88) Mahler, B.; Nadal, B.; Bouet, C.; Patriarche, G.; Dubertret, B. Core/shell colloidal semiconductor nanoplatelets. *J. Am. Chem. Soc.* **2012**, *134* (45), 18591.

(89) Chen, X.; Lu, H.; Li, Z.; Zhai, Y.; Ndione, P. F.; Berry, J. J.; Zhu, K.; Yang, Y.; Beard, M. C. Impact of layer thickness on the charge-carrier and spin coherence lifetime in two-dimensional layered perovskite single crystals. *ACS Energy Lett.* **2018**, *3* (9), 2273.

(90) Geiregat, P.; Tomar, R.; Chen, K.; Singh, S.; Hodgkiss, J. M.; Hens, Z. Thermodynamic equilibrium between excitons and excitonic molecules dictates optical gain in colloidal CdSe quantum wells. *J. Phys. Chem. Lett.* **2019**, *10* (13), 3637.

(91) Odenthal, P.; Talmadge, W.; Gundlach, N.; Wang, R.; Zhang, C.; Sun, D.; Yu, Z. G.; Valy Vardeny, Z.; Li, Y. S. Spin-polarized exciton quantum beating in hybrid organic–inorganic perovskites. *Nat. Phys.* **2017**, *13* (9), 894.

(92) Shornikova, E. V.; Golovatenko, A. A.; Yakovlev, D. R.; Rodina, A. V.; Biadala, L.; Qiang, G.; Kuntzmann, A.; Nasilowski, M.; Dubertret, B.; Polovitsyn, A.; et al. Surface spin magnetism controls the polarized exciton emission from CdSe nanoplatelets. *Nat. Nanotechnol.* **2020**, *15* (4), 277.

(93) Xiang, D.; Li, Y.; Wang, L.; Ding, T.; Wang, J.; Wu, K. Electron and hole spin relaxation in CdSe colloidal nanoplatelets. *J. Phys. Chem. Lett.* **2021**, *12* (1), 86.

(94) Kikkawa, J.; Gupta, J.; Malajovich, I.; Awschalom, D. Spin coherence in semiconductors: storage, transport and reduced dimensionality. *Physica E: Low-dimensional Systems and Nanostructures* **2001**, *9* (1), 194.

(95) Ouyang, M.; Awschalom, D. D. Coherent spin transfer between molecularly bridged quantum dots. *Science* **2003**, *301* (5636), 1074.

(96) Žutić, I.; Fabian, J.; Sarma, S. D. Spintronics: Fundamentals and applications. *Rev. Mod. Phys.* **2004**, *76* (2), 323.

(97) Chen, X.; Lu, H.; Wang, K.; Zhai, Y.; Lunin, V.; Sercel, P. C.; Beard, M. C. Tuning Spin-Polarized Lifetime in Two-Dimensional Metal–Halide Perovskite through Exciton Binding Energy. *J. Am. Chem. Soc.* **2021**, *143* (46), 19438.

(98) Ithurria, S.; Talapin, D. V. Colloidal Atomic Layer Deposition (c-ALD) using Self-Limiting Reactions at Nanocrystal Surface Coupled to Phase Transfer between Polar and Nonpolar Media. *J. Am. Chem. Soc.* **2012**, *134* (45), 18585.

(99) Benchamekh, R.; Gippius, N. A.; Even, J.; Nestoklon, M.; Jancu, J. M.; Ithurria, S.; Dubertret, B.; Efros, A. L.; Voisin, P. Tight-binding calculations of image-charge effects in colloidal nanoscale platelets of CdSe. *Phys. Rev. B* **2014**, *89* (3), 035307.

(100) Ji, B.; Rabani, E.; Efros, A. L.; Vaxenburg, R.; Ashkenazi, O.; Azulay, D.; Banin, U.; Millo, O. Dielectric confinement and excitonic effects in two-dimensional nanoplatelets. *ACS Nano* **2020**, *14* (7), 8257.

(101) Shornikova, E. V.; Yakovlev, D. R.; Gippius, N. A.; Qiang, G.; Dubertret, B.; Khan, A. H.; Di Giacomo, A.; Moreels, I.; Bayer, M. Exciton Binding Energy in CdSe Nanoplatelets Measured by One-and Two-Photon Absorption. *Nano Lett.* **2021**, *21* (24), 10525.

(102) Rodà, C.; Geiregat, P.; Di Giacomo, A.; Moreels, I.; Hens, Z. Area-Independence of the Biexciton Oscillator Strength in CdSe Colloidal Nanoplatelets. *Nano Lett.* **2022**, *22* (23), 9537.

(103) Delikanli, S.; Yu, G.; Yeltik, A.; Bose, S.; Erdem, T.; Yu, J.; Erdem, O.; Sharma, M.; Sharma, V. K.; Quliyeva, U. Ultrathin highly luminescent two-monolayer colloidal CdSe nanoplatelets. *Adv. Funct. Mater.* **2019**, *29* (35), 1901028.

(104) Greenwood, A. R.; Mazzotti, S.; Norris, D. J.; Galli, G. Determining the Structure–Property Relationships of Quasi-Two-Dimensional Semiconductor Nanoplatelets. *J. Phys. Chem. C* **2021**, *125* (8), 4820.

(105) Sigle, D. O.; Hugall, J. T.; Ithurria, S.; Dubertret, B.; Baumberg, J. J. Probing confined phonon modes in individual CdSe nanoplatelets using surface-enhanced Raman scattering. *Physical Review Letters* **2014**, *113* (8), 087402.

(106) Vong, A. F.; Irgen-Gioro, S.; Wu, Y.; Weiss, E. A. Origin of low temperature trion emission in CdSe nanoplatelets. *Nano Lett.* **2021**, *21* (23), 10040.

(107) Macias-Pinilla, D. F.; Planelles, J.; Climente, J. I. Biexcitons in CdSe nanoplatelets: geometry, binding energy and radiative rate. *Nanoscale* **2022**, *14* (23), 8493.

(108) Brumberg, A.; Watkins, N. E.; Diroll, B. T.; Schaller, R. D. Acceleration of Biexciton Radiative Recombination at Low Temperature in CdSe Nanoplatelets. *Nano Lett.* **2022**, *22* (17), 6997.

(109) Grim, J. Q.; Christodoulou, S.; Di Stasio, F.; Krahne, R.; Cingolani, R.; Manna, L.; Moreels, I. Continuous-wave biexciton lasing at room temperature using solution-processed quantum wells. *Nat. Nanotechnol.* **2014**, *9* (11), 891.

(110) Huxter, V. M.; Kovalevskij, V.; Scholes, G. D. Dynamics within the Exciton Fine Structure of Colloidal CdSe Quantum Dots. *J. Phys. Chem. B* **2005**, *109* (43), 20060.

(111) Rodina, A.; Efros, A. L. Magnetic Properties of Nonmagnetic Nanostructures: Dangling Bond Magnetic Polaron in CdSe Nanocrystals. *Nano Lett.* **2015**, *15* (6), 4214.

(112) Rodina, A. V.; Golovatenko, A. A.; Shornikova, E. V.; Yakovlev, D. R. Spin Physics of Excitons in Colloidal Nanocrystals. *Phys. Solid State* **2018**, *60* (8), 1537.

(113) Hu, R.; Wu, Z.; Zhang, Y.; Yakovlev, D. R.; Liang, P.; Qiang, G.; Guo, J.; Jia, T.; Sun, Z.; Bayer, M. Long-Lived Negative Photocharging in Colloidal CdSe Quantum Dots Revealed by Coherent Electron Spin Precession. *J. Phys. Chem. Lett.* **2019**, *10* (17), 4994.

(114) Feng, D.; Yakovlev, D. R.; Dubertret, B.; Bayer, M. Charge separation dynamics in CdSe/CdS core/shell nanoplatelets addressed by coherent electron spin precession. *ACS Nano* **2020**, *14* (6), 7237.

(115) Brenner, T. M.; Egger, D. A.; Kronik, L.; Hodes, G.; Cahen, D. Hybrid organic—inorganic perovskites: low-cost semiconductors with intriguing charge-transport properties. *Nature Reviews Materials* **2016**, *1* (1), 15007.

(116) Herz, L. M. Charge-Carrier Dynamics in Organic-Inorganic Metal Halide Perovskites. *Annual Review of Physical Chemistry* **2016**, *67* (1), 65-89.

(117) Johnston, M. B.; Herz, L. M. Hybrid Perovskites for Photovoltaics: Charge-Carrier Recombination, Diffusion, and Radiative Efficiencies. *Accounts of Chemical Research* **2016**, *49* (1), 146-154.

(118) Miyata, K.; Atallah, T. L.; Zhu, X.-Y. Lead halide perovskites: Crystal-liquid duality, phonon glass electron crystals, and large polaron formation. *Science Advances* **2017**, *3* (10), e1701469.

(119) Panzer, F.; Li, C.; Meier, T.; Köhler, A.; Huettner, S. Impact of Structural Dynamics on the Optical Properties of Methylammonium Lead Iodide Perovskites. *Advanced Energy Materials* **2017**, *7* (16), 1700286.

(120) Guzelturk, B.; Winkler, T.; Van de Goor, T. W. J.; Smith, M. D.; Bourelle, S. A.; Feldmann, S.; Trigo, M.; Teitelbaum, S. W.; Steinrück, H.-G.; de la Pena, G. A.; et al. Visualization of dynamic polaronic strain fields in hybrid lead halide perovskites. *Nature Materials* **2021**, *20* (5), 618-623.

(121) Schlipf, M.; Poncé, S.; Giustino, F. Carrier Lifetimes and Polaronic Mass Enhancement in the Hybrid Halide Perovskite $CH_3NH_3PbI_3$ from Multiphonon Frohlich Coupling. *Physical Review Letters* **2018**, *121* (8), 086402.

(122) Yang, Y.; Ostrowski, D. P.; France, R. M.; Zhu, K.; van de Lagemaat, J.; Luther, J. M.; Beard, M. C. Observation of a hot-phonon bottleneck in lead-iodide perovskites. *Nature Photonics* **2016**, *10* (1), 53-59.

(123) Frost, J. M.; Whalley, L. D.; Walsh, A. Slow Cooling of Hot Polarons in Halide Perovskite Solar Cells. *ACS Energy Letters* **2017**, *2* (12), 2647-2652.

(124) Quarti, C.; Mosconi, E.; Ball, J. M.; D'Innocenzo, V.; Tao, C.; Pathak, S.; Snaith, H. J.; Petrozza, A.; De Angelis, F. Structural and optical properties of methylammonium lead iodide

across the tetragonal to cubic phase transition: implications for perovskite solar cells. *Energy & Environmental Science* **2016**, *9* (1), 155-163.

(125) Rolston, N.; Bennett-Kennett, R.; Schelhas, L. T.; Luther, J. M.; Christians, J. A.; Berry, J. J.; Dauskardt, R. H. Comment on "Light-induced lattice expansion leads to high-efficiency perovskite solar cells". *Science* **2020**, *368* (6488), eaay8691.

(126) Zhu, H.; Miyata, K.; Fu, Y.; Wang, J.; Joshi Prakriti, P.; Niesner, D.; Williams Kristopher, W.; Jin, S.; Zhu, X. Y. Screening in crystalline liquids protects energetic carriers in hybrid perovskites. *Science* **2016**, *353* (6306), 1409-1413.

(127) Allegro, I.; Li, Y.; Richards, B. S.; Paetzold, U. W.; Lemmer, U.; Howard, I. A. Bimolecular and Auger Recombination in Phase-Stable Perovskite Thin Films from Cryogenic to Room Temperature and Their Effect on the Amplified Spontaneous Emission Threshold. *The Journal of Physical Chemistry Letters* **2021**, *12* (9), 2293-2298.

(128) Diroll, B. T. Temperature-Dependent Intraband Relaxation of Hybrid Perovskites. *The Journal of Physical Chemistry Letters* **2019**, *10* (18), 5623-5628.

(129) Hopper, T. R.; Gorodetsky, A.; Frost, J. M.; Müller, C.; Lovrincic, R.; Bakulin, A. A. Ultrafast Intraband Spectroscopy of Hot-Carrier Cooling in Lead-Halide Perovskites. *ACS Energy Letters* **2018**, *3* (9), 2199-2205.

(130) Jacobsson, T. J.; Schwan, L. J.; Ottosson, M.; Hagfeldt, A.; Edvinsson, T. Determination of Thermal Expansion Coefficients and Locating the Temperature-Induced Phase Transition in Methylammonium Lead Perovskites Using X-ray Diffraction. *Inorganic Chemistry* **2015**, *54* (22), 10678-10685.

(131) Verma, S. D.; Gu, Q.; Sadhanala, A.; Venugopalan, V.; Rao, A. Slow Carrier Cooling in Hybrid Pb–Sn Halide Perovskites. *ACS Energy Letters* **2019**, *4* (3), 736-740.

(132) Poglitsch, A.; Weber, D. Dynamic disorder in methylammoniumtrihalogenoplumbates (II) observed by millimeter-wave spectroscopy. *The Journal of Chemical Physics* **1987**, *87* (11), 6373-6378.

(133) Whitfield, P. S.; Herron, N.; Guise, W. E.; Page, K.; Cheng, Y. Q.; Milas, I.; Crawford, M. K. Structures, Phase Transitions and Tricritical Behavior of the Hybrid Perovskite Methyl Ammonium Lead Iodide. *Scientific Reports* **2016**, *6* (1), 35685.

(134) Stoumpos, C. C.; Malliakas, C. D.; Kanatzidis, M. G. Semiconducting Tin and Lead Iodide Perovskites with Organic Cations: Phase Transitions, High Mobilities, and Near-Infrared Photoluminescent Properties. *Inorganic Chemistry* **2013**, *52* (15), 9019-9038.

(135) Wu, X.; Tan, L. Z.; Shen, X.; Hu, T.; Miyata, K.; Trinh, M. T.; Li, R.; Coffee, R.; Liu, S.; Egger, D. A.; et al. Light-induced picosecond rotational disordering of the inorganic sublattice in hybrid perovskites. *Science Advances* **2017**, *3* (7), e1602388.

(136) Harmand, M.; Coffee, R.; Bionta, M. R.; Chollet, M.; French, D.; Zhu, D.; Fritz, D. M.; Lemke, H. T.; Medvedev, N.; Ziaja, B.; et al. Achieving few-femtosecond time-sorting at hard X-ray free-electron lasers. *Nature Photonics* **2013**, *7* (3), 215-218.

(137) Kirschner, M. S.; Diroll, B. T.; Guo, P.; Harvey, S. M.; Helweh, W.; Flanders, N. C.; Brumberg, A.; Watkins, N. E.; Leonard, A. A.; Evans, A. M.; et al. Photoinduced, reversible phase transitions in all-inorganic perovskite nanocrystals. *Nature Communications* **2019**, *10* (1), 504.

(138) Kirschner, M. S.; Hannah, D. C.; Diroll, B. T.; Zhang, X.; Wagner, M. J.; Hayes, D.; Chang, A. Y.; Rowland, C. E.; Lethiec, C. M.; Schatz, G. C.; et al. Transient Melting and Recrystallization of Semiconductor Nanocrystals Under Multiple Electron–Hole Pair Excitation. *Nano Letters* **2017**, *17* (9), 5314-5320.

(139) Brumberg, A.; Kirschner, M. S.; Diroll, B. T.; Williams, K. R.; Flanders, N. C.; Harvey, S. M.; Leonard, A. A.; Watkins, N. E.; Liu, C.; Kinigstein, E. D.; et al. Anisotropic Transient Disordering of Colloidal, Two-Dimensional CdSe Nanoplatelets upon Optical Excitation. *Nano Letters* **2021**, *21* (3), 1288-1294.

(140) Harvey, S. M.; Houck, D. W.; Kirschner, M. S.; Flanders, N. C.; Brumberg, A.; Leonard, A. A.; Watkins, N. E.; Chen, L. X.; Dichtel, W. R.; Zhang, X.; et al. Transient Lattice Response upon Photoexcitation in CuInSe2 Nanocrystals with Organic or Inorganic Surface Passivation. *ACS Nano* **2020**, *14* (10), 13548-13556.

(141) Ghosh, D.; Welch, E.; Neukirch, A. J.; Zakhidov, A.; Tretiak, S. Polarons in Halide Perovskites: A Perspective. *The Journal of Physical Chemistry Letters* **2020**, *11* (9), 3271-3286.

(142) Snaider, J. M.; Guo, Z.; Wang, T.; Yang, M.; Yuan, L.; Zhu, K.; Huang, L. Ultrafast Imaging of Carrier Transport across Grain Boundaries in Hybrid Perovskite Thin Films. *ACS Energy Letters* **2018**, *3* (6), 1402-1408.

(143) Jiang, X.; Hoffman, J.; Stoumpos, C. C.; Kanatzidis, M. G.; Harel, E. Transient Sub-Band-Gap States at Grain Boundaries of CH3NH3PbI3 Perovskite Act as Fast Temperature Relaxation Centers. *ACS Energy Letters* **2019**, *4* (7), 1741-1747.

(144) Gold-Parker, A.; Gehring, P. M.; Skelton, J. M.; Smith, I. C.; Parshall, D.; Frost, J. M.; Karunadasa, H. I.; Walsh, A.; Toney, M. F. Acoustic phonon lifetimes limit thermal transport in methylammonium lead iodide. *Proceedings of the National Academy of Sciences* **2018**, *115* (47), 11905-11910.

(145) Chang, A. Y.; Cho, Y.-J.; Chen, K.-C.; Chen, C.-W.; Kinaci, A.; Diroll, B. T.; Wagner, M. J.; Chan, M. K. Y.; Lin, H.-W.; Schaller, R. D. Slow Organic-to-Inorganic Sub-Lattice Thermalization in Methylammonium Lead Halide Perovskites Observed by Ultrafast Photoluminescence. *Advanced Energy Materials* **2016**, *6* (15), 1600422.

(146) Guo, P.; Gong, J.; Sadasivam, S.; Xia, Y.; Song, T.-B.; Diroll, B. T.; Stoumpos, C. C.; Ketterson, J. B.; Kanatzidis, M. G.; Chan, M. K. Y.; et al. Slow thermal equilibration in

methylammonium lead iodide revealed by transient mid-infrared spectroscopy. *Nature Communications* **2018**, *9* (1), 2792.

(147) Crothers, T. W.; Milot, R. L.; Patel, J. B.; Parrott, E. S.; Schlipf, J.; Müller-Buschbaum, P.; Johnston, M. B.; Herz, L. M. Photon Reabsorption Masks Intrinsic Bimolecular Charge-Carrier Recombination in CH3NH3PbI3 Perovskite. *Nano Letters* **2017**, *17* (9), 5782-5789.

(148) Davies, C. L.; Filip, M. R.; Patel, J. B.; Crothers, T. W.; Verdi, C.; Wright, A. D.; Milot, R. L.; Giustino, F.; Johnston, M. B.; Herz, L. M. Bimolecular recombination in methylammonium lead triiodide perovskite is an inverse absorption process. *Nature Communications* **2018**, *9* (1), 293.

(149) Zheng, F.; Wang, L.-w. Large polaron formation and its effect on electron transport in hybrid perovskites. *Energy & Environmental Science* **2019**, *12* (4), 1219-1230.

(150) Kennard, R. M.; Dahlman, C. J.; DeCrescent, R. A.; Schuller, J. A.; Mukherjee, K.; Seshadri, R.; Chabinyc, M. L. Ferroelastic Hysteresis in Thin Films of Methylammonium Lead Iodide. *Chemistry of Materials* **2021**, *33* (1), 298-309.

(151) Onoda-Yamamuro, N.; Matsuo, T.; Suga, H. Calorimetric and IR spectroscopic studies of phase transitions in methylammonium trihalogenoplumbates (II). *Journal of Physics and Chemistry of Solids* **1990**, *51* (12), 1383-1395.

(152) Nah, S.; Spokoyny, B.; Stoumpos, C.; Soe, C. M. M.; Kanatzidis, M.; Harel, E. Spatially segregated free-carrier and exciton populations in individual lead halide perovskite grains. *Nature Photonics* **2017**, *11* (5), 285-288.

(153) Qian, X.; Gu, X.; Yang, R. Lattice thermal conductivity of organic-inorganic hybrid perovskite CH3NH3PbI3. *Applied Physics Letters* **2016**, *108* (6), 063902.

(154) Lee, J.-H.; Bristowe, N. C.; Bristowe, P. D.; Cheetham, A. K. Role of hydrogen-bonding and its interplay with octahedral tilting in CH3NH3PbI3. *Chemical Communications* **2015**, *51* (29), 6434-6437.

(155) Lee, J.-H.; Bristowe, N. C.; Lee, J. H.; Lee, S.-H.; Bristowe, P. D.; Cheetham, A. K.; Jang, H. M. Resolving the Physical Origin of Octahedral Tilting in Halide Perovskites. *Chemistry of Materials* **2016**, *28* (12), 4259-4266.

(156) Cannelli, O.; Colonna, N.; Puppin, M.; Rossi, T. C.; Kinschel, D.; Leroy, L. M. D.; Löffler, J.; Budarz, J. M.; March, A. M.; Doumy, G.; et al. Quantifying Photoinduced Polaronic Distortions in Inorganic Lead Halide Perovskite Nanocrystals. *Journal of the American Chemical Society* **2021**, *143* (24), 9048-9059.

(157) Dastidar, S.; Li, S.; Smolin, S. Y.; Baxter, J. B.; Fafarman, A. T. Slow Electron–Hole Recombination in Lead Iodide Perovskites Does Not Require a Molecular Dipole. *ACS Energy Letters* **2017**, *2* (10), 2239-2244.

(158) Munson, K. T.; Swartzfager, J. R.; Gan, J.; Asbury, J. B. Does Dipolar Motion of Organic Cations Affect Polaron Dynamics and Bimolecular Recombination in Halide Perovskites? *The Journal of Physical Chemistry Letters* **2020**, *11* (8), 3166-3172.

(159) Zhu, H.; Trinh, M. T.; Wang, J.; Fu, Y.; Joshi, P. P.; Miyata, K.; Jin, S.; Zhu, X. Y. Organic Cations Might Not Be Essential to the Remarkable Properties of Band Edge Carriers in Lead Halide Perovskites. *Advanced Materials* **2017**, *29* (1), 1603072.

(160) Govinda, S.; Kore, B. P.; Swain, D.; Hossain, A.; De, C.; Guru Row, T. N.; Sarma, D. D. Critical Comparison of FAPbX3 and MAPbX3 (X = Br and Cl): How Do They Differ? *The Journal of Physical Chemistry C* **2018**, *122* (25), 13758-13766.

(161) Motta, C.; El-Mellouhi, F.; Kais, S.; Tabet, N.; Alharbi, F.; Sanvito, S. Revealing the role of organic cations in hybrid halide perovskite CH3NH3PbI3. *Nature Communications* **2015**, *6* (1), 7026.

(162) Guo, P.; Xia, Y.; Gong, J.; Stoumpos, C. C.; McCall, K. M.; Alexander, G. C. B.; Ma, Z.; Zhou, H.; Gosztola, D. J.; Ketterson, J. B.; et al. Polar Fluctuations in Metal Halide Perovskites Uncovered by Acoustic Phonon Anomalies. *ACS Energy Letters* **2017**, *2* (10), 2463-2469.

(163) Yang, B.; Ming, W.; Du, M.-H.; Keum, J. K.; Puretzky, A. A.; Rouleau, C. M.; Huang, J.; Geohegan, D. B.; Wang, X.; Xiao, K. Real-Time Observation of Order-Disorder Transformation of Organic Cations Induced Phase Transition and Anomalous Photoluminescence in Hybrid Perovskites. *Advanced Materials* **2018**, *30* (22), 1705801.

(164) Yaffe, O.; Guo, Y.; Tan, L. Z.; Egger, D. A.; Hull, T.; Stoumpos, C. C.; Zheng, F.; Heinz, T. F.; Kronik, L.; Kanatzidis, M. G.; et al. Local Polar Fluctuations in Lead Halide Perovskite Crystals. *Physical Review Letters* **2017**, *118* (13), 136001.

(165) Fabini, D. H.; Seshadri, R.; Kanatzidis, M. G. The underappreciated lone pair in halide perovskites underpins their unusual properties. *MRS Bulletin* **2020**, *45* (6), 467-477.

(166) Billing, D. G.; Lemmerer, A. Synthesis, characterization and phase transitions in the inorganic-organic layered perovskite-type hybrids [(CnH2n + 1NH3)2PbI4], n = 4, 5 and 6. *Acta Crystallographica* **2007**, *B63* (5), 735-737.

(167) Stoumpos, C. C.; Cao, D. H.; Clark, D. J.; Young, J.; Rondinelli, J. M.; Jang, J. I.; Hupp, J. T.; Kanatzidis, M. G. Ruddlesden–Popper Hybrid Lead Iodide Perovskite 2D Homologous Semiconductors. *Chemistry of Materials* **2016**, *28* (8), 2852-2867.

(168) Lemmerer, A.; Billing, D. G. Synthesis, characterization and phase transitions of the inorganic–organic layered perovskite-type hybrids [(CnH2n+1NH3)2PbI4], n = 7, 8, 9 and 10. *Dalton Transactions* **2012**, *41* (4), 1146-1157.

(169) Spanopoulos, I.; Hadar, I.; Ke, W.; Tu, Q.; Chen, M.; Tsai, H.; He, Y.; Shekhawat, G.; Dravid, V. P.; Wasielewski, M. R.; et al. Uniaxial Expansion of the 2D Ruddlesden–Popper

Perovskite Family for Improved Environmental Stability. *Journal of the American Chemical Society* **2019**, *141* (13), 5518-5534.

(170) Momma, K.; Izumi, F. VESTA 3 for three-dimensional visualization of crystal, volumetric and morphology data. *Journal of Applied Crystallography* **2011**, *44* (6), 1272-1276.

(171) Toby, B. H.; Von Dreele, R. B. GSAS-II: the genesis of a modern open-source all purpose crystallography software package. *Journal of Applied Crystallography* **2013**, *46* (2), 544-549.

Curriculum Vitae

Summary

Collaborative and creative scientist who is a driven community leader and effective science communicator. Thrives in interdisciplinary and fast-paced settings. Enthusiastic about applying knowledge in development of renewable energy and sustainable materials. Ph.D. candidate (anticipated graduation: 2023) and National Science Foundation Research Fellow in materials chemistry at Northwestern University studying electron dynamics for solar applications. Recipient of 6 prestigious research awards, co-author on 15+ research publications, including 3 as first author. Passionate about improving public scientific education and awareness, especially among underrepresented youth.

Education

Northwestern University – Evanston, IL **2018 – 2023**
Doctor of Philosophy (Ph.D), Materials Chemistry *magna cum laude* GPA: 3.79/4.00

University of Michigan – Ann Arbor, MI **2014 – 2018**
Bachelor of Science (B.S.) Chemistry with Honors *cum laude* GPA: 3.72/4.00

Research Experience

Photophysics of Semiconductors for Energy Applications **2018 – present**

Northwestern University, *Principal Investigators:* Prof. Richard Schaller, Prof. Mercouri Kanatzidis

- Investigated and established new fundamental models for electronic behavior in nanomaterials using time-resolved optical spectroscopies and improved synthetic methods, including the first empirical demonstration of distance dependence for energy transfer between 2D nanomaterials
- Identified novel structural dynamics in the leading photovoltaic perovskite candidate methylammonium lead iodide, revealing key factors responsible for its outstanding properties
- Led and participated in international collaborations resulting in several high-impact publications
- Designed and optimized one of 3 time-resolved structural probes available worldwide using high-energy, synchrotron X-ray source at the Advanced Photon Source, Argonne National Laboratory to investigate *in-situ* structural behavior in thin films and colloidal nanoparticles
- Managed, repaired, and trained new members on research equipment including 2 UV-Vis-NIR spectrophotometer; 3 ultrafast laser systems with Ti:sapphire oscillators and over ~1000 lenses, mirrors, other optics

Heterogeneous Photocatalysis for Solar Fuel Generation **2016 – 2018**

University of Michigan, *Principal Investigator:* Prof. Bart Bartlett

- Investigated complex oxides for heterogeneous catalysis in aerobic conditions, optimizing visible light absorption and chemical stability to boost efficiency and viability in solar applications
- Identified systematic trends across materials for photochemical oxidation of biomass byproduct wastes into desired chemicals, elucidating catalytic mechanisms for selective product formation at competitive reaction rates

Solid-State Electrolytes for Lithium Batteries **2016**

Justus Liebig University of Gießen, *Principal Investigator:* Prof. Jürgen Janek

- Characterized structural and electrochemical properties of Li_2S-P_2S_5 glasses for solid-state electrolytes in Li-ion batteries
- Explored synthetic methods for obtaining amorphous material, including molten-material quenching and planetary ball-milling, resulting in conductivities several orders of magnitude greater than in crystalline materials

Paleoethnobotany of Bronze Age Şanţul-Mare **2014 - 2016**

University of Michigan, *Principal Investigators*: Prof. Amy Nicodemus, Prof. Laura Motta

- Site-excavated and analyzed charred archaeological seed remains in Pecica, Romania to establish agricultural methods and food pathways at major center for production of metalwork and horse domestication during the middle Bronze Age (1800-1500 BCE)

Publications (*denotes equal contribution)

11. **Panuganti, S.;** Cuthriell, S. A.; Guzelturk, B.; Leonard, A. A.; Quintero, M. A.; Laing, C. C.; Zhang, X.; Chen, L. X.; Kanatzidis, M. G.; Schaller, R. D. "Transient X-ray Diffraction Reveals Nonequilibrium Phase Transition in Thin Films of $CH_3NH_3PbI_3$ Perovskite." *ACS Energy Lett.* **2023,** *8* (1), 691-698.

10. *Martin, P. I.; ***Panuganti, S.;** Portner, J. C.; Watkins, N. E.; Kanatzidis, M. G.; Schaller, R. D. "Excitonic Spin-Coherence Lifetimes in CdSe Nanoplatelets Increase Significantly with Core/Shell Morphology." *Nano Lett.* **2023,** *ASAP.*

9. Cuthriell, S. A.; **Panuganti, S.;** Laing, C. C.; Quintero, M. A.; Guzelturk, B.; Yazdani, N.; Traore, B.; Brumberg, A.; Malliakas, C. D.; Lindenberg, A. M.; Wood, V.; Katan, C.; Even, J.; Zhang, X.; Kanatzidis, M. G.; Schaller, R. D. "Nonequilibrium Lattice Dynamics in Photoexcited 2D Perovskites." *Adv. Mat.* **2022,** *34* (44), 2202709.

8. Kennard, R. M.; Dahlman, C. J.; Morgan, E. E.; Chung, J.; Cotts, B. L.; Kincaid, J. R. A.; DeCrescent, R. A.; Stone, K. H.; **Panuganti, S.;** Mohtashami, Y.; Mao, L.; Schaller, R. D.; Salleo, A.; Kanatzidis, M. G.; Schuller, J. A.; Seshadri, R.; Chabinyc, M. L. "Enhancing and Extinguishing the Different Emission Features of 2D $(EA_{1-x}FA_x)_4Pb_3Br_{10}$ Perovskite Films." *Adv. Opt. Mat.* **2022,** *10* (17), 2200547.

7. Wang, S.; Morgan, E. E.; **Panuganti, S.;** Mao, L.; Vishnoi, P.; Wu, G.; Liu, Q.; Kanatzidis, M. G.; Schaller, R. D.; Seshadri, R. "Ligand Control of Structural Diversity in Luminescent Hybrid Copper (I) Iodides." *Chem. Mater.* **2022,** *34* (7), 3206-3216.

6. **Panuganti, S.;** Besteiro, L. V.; Vasileiadou, E. S.; Hoffman, J. M.; Govorov, A. O.; Gray, S. K.; Kanatzidis, M. G.; Schaller, R. D. "Distance dependence of Förster Resonance Energy Transfer Rates in 2D Perovskite Quantum Wells via Control of Organic Spacer Length." *J. Am. Chem. Soc.* **2021,** *143* (11), 4244-4252.

5. Adhikari, S.; Cortes, C. L.; Wen, X.; **Panuganti, S.**; Gosztola, D. J.; Schaller, R. D.; Wiederrecht, G. P.; Gray, S. K. "Accelerating ultrafast spectroscopy with compressive sensing." *Phys. Rev. Applied* **2021,** *15* (2), 024032.

4. Brumberg. A; Kirschner, M. S.; Diroll, B. T.; Williams, K. R.; Flanders, N. C.; Harvey, S. M.; Leonard, A. A.; Watkins, N. E.; Liu, C.; Kinigstein, E. D.; Yu, J.; Evans, A. M.; Liu, Y.; Cuthriell, S. A.; **Panuganti, S.**; Dichtel, W. R.; Kanatzidis, M. G.; Wasielewski, M. R.; Zhang, X.; Chen, L. X.; Schaller, R. D. "Anisotropic Transient Disordering of Colloidal, Two-Dimensional Nanoplatelets upon Optical Excitation." *Nano Lett.* **2021,** *21* (3), 1288-1294.

3. Diroll, B. T.; Brumberg, A.; Leonard, A. A.; **Panuganti, S.**; Watkins, N. E.; Cuthriell, S. A.; Harvery, S. M.; Kinigstein, E. D.; Yu, J.; Zhang, X.; Kanatzidis, M. G.; Wasielewski, M. R.; Chen, L. X.; Schaller, R. D. "Photothermal behaviour of titanium nitride nanoparticles evaluated by transient X-ray diffraction." *Nanoscale* **2021,** *13,* 2658-2664.

2. Proctor, A. D.; Panuganti, S.; Bartlett, B. M. "$CuWO_4$ as a Photocatalyst for Room Temperature Aerobic Benzylamine Oxidation." *Chem. Commun*. **2018**, *54* (9), 1101-1104.

1. Brancho, J. J.; Proctor, A. D.; **Panuganti, S.;** Bartlett, B. M. "Urea-glass preparation of titanium niobium nitrides and subsequent oxidation to photoactive titanium niobium oxynitrides." *Dalton Trans.* **2017,** *46* (36), 12081-12087.

Presentations

5. **Panuganti, S.** *Basolo-Ibers-Pearson Inorganic Seminar.* "Anomalous carrier dynamics in bivalent metal selenophosphates with intrinsic anti-ferromagnetism." **Oct. 14, 2022.** Oral Presentation.

4. **Panuganti, S.** *Material Research Society Spring 2022*. "Direct Observation of Photoinduced, Non-Equilibrium Phase Transition in $CH_3NH_3PbI_3$ via Time-Resolved X-ray Diffraction." **May 9, 2022.** Poster Presentation.

3. **Panuganti, S.** *Basolo-Ibers-Pearson Inorganic Seminar.* "Directly probing structural distortions in bulk seminconductors upon photoexcitation with transient X-ray diffraction." **Feb, 5. 2021.** Oral Presentation.

2. **Panuganti, S.** *Material Research Society Spring 2021*. "Distance Dependence of Förster Resonance Energy Transfer (FRET) in 2D Perovskite Quantum Wells (PQWs)." **Apr. 22, 2021.** Oral Presentation.

1. **Panuganti, S.** *Basolo-Ibers-Pearson Inorganic Seminar.* "Dynamics of non-radiative energy transfer between 2D quantum wells in bulk semiconductors." **Jan. 31, 2020.** Oral Presentation.

Leadership and Outreach

Lesson Leader, Science in the Classroom – *15 hours/week* **2018 – present**

- Organize, lead, and teach hands-on science experiments and demonstrations for 3rd and 4th graders to explore and discover high-level science concepts at Hayt Elementary School
- Collaborate with Chicago Public School teachers and curriculum to design grade-level appropriate activities for introducing concepts such as wave-particle duality, chromatography, electricity, and others

Student Recruitment, Expanding Your Horizons Symposia – *5 hours/week* **2018 – 2021**

- Recruited middle school girls of color from low-income backgrounds to participate in one-day STEM symposia that feature educational workshops aiming to boost interest in scientific careers,

- Communicated with Chicago Public School administrators to increase accessibility for students with lack of transportation and financial resources

Teaching Assistant, Northwestern Dept. of Chemistry – *30 hours/week* **2018 – 2021**

- Planned, taught, and evaluated upper-level undergraduate chemistry laboratory coursework in air-free material synthesis and electrochemistry with 15-20 students, receiving highly positive feedback from 95% of students for approachability and engaging communication style
- Led general chemistry laboratory sections with 20-30 students, working with teaching faculty and 15+ other TAs to create equitable grading and teaching practices across 300+ students enrolled in course

Executive Director, South Asian Awareness Network – *25 hours/week* **2014 – 2018**

- Organized 20+ events yearly for advocacy and civic engagement surrounding issues salient to South Asian diaspora including annual, regional conference that attracted 400+ attendees with past speakers including Dr. Sanjay Gupta, Hasan Minhaj, and other prominent public figures
- Designed workshops for low-income high school students in Detroit to facilitate dialogue around cultural barriers to pursuing higher education, especially among South Asian girls, and aiding in college applications

Editor, Journal of Undergraduate Research – *10 hours/week* **2016 – 2018**

- Solicited manuscript submissions from students from 25+ departments with a focus on work conducted by underrepresented minorities in STEM
- Collaborated with researchers to revise and prepare their work for broad appeal

Academic Tutor, Michigan Athletics – *15 hours/week* **2017 – 2018**

- Instructed student athletes in STEM courses to improve retention and graduation rates of student scholarship recipients, primarily from low-income and underrepresented backgrounds

Teaching Assistant, Michigan Dept. of Chemistry – *15 hours/week* **2017 – 2018**

- Led general chemistry and organic laboratory sections with 20-30 students, assisting in planning and grading

Awards, Fellowships, and Scholarships

International Institute for Nanotechnology Ryan Fellow **2021**
Research fellowship that provides additional stipend benefits and research awards to outstanding graduate students dedicated to the exploration of fundamental nanoscale science

National Science Foundation Graduate Research Fellowship (NSF GRFP) **2020**
Graduate research fellowship in Chemical Structure, Dynamics, and Mechanism covering tuition and stipend for three years in recognition and support of outstanding doctoral students in NSF-supported STEM disciplines

Hierarchical Materials Cluster Fellow **2019**
Interdisciplinary academic and research program providing one quarter of tuition and stipend for students pursuing research in nanomaterials

DAAD Research in Science and Engineering Scholarship **2016**
Research scholarship awarded by German Exchange Service (DAAD) to 300 students each year from North America, Great Britain, and Ireland covering all travel, accommodation, and stipend to work and study at a German university

Chemical Research Grant, Society for German Chemists **2016**
External research grant through the Stipendien-Fonds foundation supporting outstanding students in academic chemistry research in Germany

Richard I. Ford Endowment Fund **2015**
Research grant supporting research, travel, and accommodation for students conducting research on diverse questions concerning humans and the environment

Jean E. Fairfax Scholarship **2014**
Four-year academic tuition scholarship in honor of civil rights activist awarded to incoming students with demonstrated scholarly potential and record of leadership

Young Adult Cancer Survivors Scholarship **2014**
National scholarship fund, My Hometown Heroes, serving college bound young adult cancer survivors across the United States

Additional Skills

Languages: Fluent in English, Spanish, Telugu; Conversational German, Hindi **Techniques:** *X-ray diffraction*: powder, single-crystal, GIWAXS, SAXS. *Optical spectroscopy:* UV-vis-NIR, Raman, fluorescence. *Transient characterization:* absorption, transient THz, transient reflectance, time-resolved powder X-ray diffraction, time-correlated single photon counting, streak camera, transient femtosecond stimulated Raman. **Software:** OriginLab, MATLAB, Surface Explorer, HDTPA, HELIOS, Labview, QXRD, GSAS-II, WinXPOW, Vesta, Diamond, Mercury. **Other:** CNC machining and woodworking, metal casting and forging, brewing, vegan fermentations, backpacking